Attenuation Field Estimation Using Radio Tomography

Corey D. Cooke

Thesis submitted to the Faculty of the
Virginia Polytechnic Institute and State University
in partial fulfillment of the requirements for the degree of

Master of Science
in
Electrical Engineering

R. Michael Buehrer, Chair
Timothy Pratt
Steven W. Ellingson

August 11, 2011
Blacksburg, Virginia

Keywords: Radio Tomography, Location Estimation, Propagation Modeling, Attenuation Field Estimation

Attenuation Field Estimation Using Radio Tomography

Corey D. Cooke

(ABSTRACT)

Radio Tomographic imaging (RTI) is an exciting new field that utilizes a sensor network of a large number of relatively simple radio nodes for inverse imaging, utilizing similar mathematical algorithms to those used in medical imaging. Previous work in this field has almost exclusively focused on device-free object location and tracking. In this thesis, the application of RTI to propagation problems will be studied– specifically using RTI to measure the strength and location of attenuating objects in an area of interest, then using this knowledge of the shadowing present in an area for radio coverage prediction.

In addition to radio coverage prediction, RTI can be used to improve the quality of RSS-based position location estimates. Because the traditional failing of RSS-based multilateration is ranging error due to attenuating objects, RTI has great potential for improving the accuracy of these estimates if shadowing objects are accounted for.

In this thesis, these two problems will primarily be studied. A comparison with other inverse imaging, remote sensing, and propagation modeling techniques of interest will be given, as well as a description of the mathematical theory used for tomographic image reconstruction. Proof-of-concept of the efficacy of applying RTI to position location will be given by computer simulation, and then physical experiments with an RTI network consisting of 28 Zigbee radio sensors will be used to verify the validity of these assertions. It will be shown in this thesis that RTI does provide noticeable improvement in RSS-based position location accuracy in cluttered environments, and it produces much more accurate RSS estimates than a standard exponential path-loss model is able to provide.

Dedication

I would like to dedicate this thesis to my parents, who have made countless sacrifices for me and taught me the value of obtaining an education, which has brought me to this point.

Acknowledgments

I would like to acknowledge the support of numerous individuals who have helped me immensely in the course of this research. First and foremost is my advisor, Dr. Buehrer, who has been extremely helpful in guiding me and helping me focus my energies in a positive direction. As well, I would like to acknowledge Dr. Robert Qiu and Dr. A. A. Beex, who while they did not directly work with me on this project, provided amazing professional opportunities to me and invaluable training in the methods of academic research.

In addition I would like to thank those that have helped me in during the (somewhat tedious) tasks of constructing, measuring, and deploying the RTI network, including Nicholas Frazier, Mayank Saraf, Hunter DeJarnette, Javier and Rebekah Schloemann, and Christian Lopez-Flores, without whose help the physical experiments would have been nearly impossible.

As well, I would like to thank Dr. Joey Wilson and the SPAN lab at the University of Utah, whose open data sets and RTI software allowed me to test RTI algorithms and rapidly deploy a working RTI network with minimal effort, allowing me to focus my energies on the problem at hand rather than "reinventing the wheel" just to develop software to make RTI measurements. I am especially grateful to Dr. Wilson for personally taking the time to answer several questions I had during the process of setting up the network.

Lastly, I would like to thank my father, Thomas H. Cooke, who, through numerous discussions during my phone calls home to my family, has given me someone with a unique perspective to bounce ideas off of, and has helped me to keep in mind the need of a practical application to my research.

Contents

1 Introduction **1**

1.1 Introduction 1

1.2 Inverse Problems 1

1.2.1 Medical Imaging 2

1.2.2 Diffraction Tomography 6

1.2.3 Wireless Channel Modeling 7

1.2.4 Position Location 8

1.3 Problem Statement 9

1.4 Applications 10

1.5 Original Contributions and Outline of Thesis 11

2 Mathematical Methods for Radio Tomographic Imaging **12**

2.1 Introduction 12

2.2 System Model 12

2.2.1 Correlated Shadowing Model 14

2.2.2 Linear Problem Formulation 16

2.2.3 Noise Models 19

2.2.4 Path Loss Exponent Estimation 20

2.2.5 Statistical Estimators for Attenuation Field Estimation 23

2.2.6 Regularization Methods 23

2.2.7 Estimation Error Analysis 25

2.3 RSS Coverage Prediction 35
2.4 Position Location 36
2.4.1 Position Location with RTI 37
2.4.2 Error Minimization Problem 37
2.4.3 Radial Search Algorithm 37
2.5 Conclusion 42

3 Computer Simulations and Proof of Concept 43
3.1 Introduction 43
3.2 Image Simulation 43
3.2.1 Image Reconstruction 46
3.2.2 Optimal Regularization Parameters 47
3.2.3 Regularized Images 53
3.3 RSS-Based Position Location 57
3.3.1 Simulation Setup 57
3.3.2 Results 58
3.4 Conclusion 64

4 Experimental Verification 65
4.1 Introduction 65
4.2 Test Environments 65
4.2.1 Scene 1 65
4.2.2 Scene 2 71
4.2.3 Scene 3 72
4.3 Experimental Procedures 73
4.3.1 Sensor Network 73
4.3.2 Optimal Regularization Parameters 76
4.3.3 Image Estimation 76
4.4 Radio Coverage Prediction 80

4.5 Tomography-Aided Radiolocation 88
4.5.1 Repositioned Test Node Location Experiments 88
4.5.2 Perimeter Node Location Experiments 91
4.5.3 Analysis 95
4.6 Conclusion 95

5 Conclusions **96**
5.1 Summary of Findings 96
5.1.1 Radio Tomographic Imaging 96
5.1.2 Improvements to Radio Coverage Prediction 96
5.1.3 Improvement to RSS-Multilateration 97
5.2 Open Research Topics 97
5.2.1 Scalability 97
5.2.2 Spatial Sampling Geometry 97
5.2.3 Refinement of Linear Estimation Problem 98
5.2.4 Spatial Correlation of Received Signal Strength 98
5.3 Conclusion 98

A RSS Estimation Error Statistics **99**

B Position Location Plots **108**

C Localization Error Statistics **118**

Bibliography **122**

List of Figures

1.1 Coordinate geometry used in deriving the Fourier Slice Theorem. The attenuating object is expressed as an object function $f(x, y)$, which in the case of RTI, represents the value of the electromagnetic attenuation coefficient in decibels per unit length. Adapted from [1]. 3

1.2 Pixel selection scheme used by algebraic methods. The blue x's represent sensor locations, the dashed line represents a single measurement ray, and the green pixels represent the pixels that affect the attenuation experienced by that ray. Adapted from [2]. 5

1.3 Geometry for a noiseless RSS-based positioning system. The blue x's represent anchor node locations, while the red circle represents the free node to be located. 9

1.4 Example random attenuation field produced using a correlated shadowing model. 10

2.1 An example of a circular RTI geometry. The blue "X"s represent sensor node locations, the blue lines represent radio links between nodes, the green circle represents an attenuating object, and the white boxes represent pixel locations. 13

2.2 An example of a square RTI geometry. 13

2.3 Random scene generated using the correlated shadowing model with $\sigma_X = 2$ dB and $\delta = 1$ ft. Note that each pixel is only slightly correlated with neighboring pixels. 15

2.4 Random scene generated using the correlated shadowing model with $\sigma_X = 2$ dB and $\delta = 4$ ft. Note that each pixel is highly correlated with neighboring pixels. 16

2.5 Ellipse method for selecting which pixels are included in a given link. The dashed blue line represents a radio link, and the green pixels are those whose centroid falls within the ellipse (whose focii lie at the node locations). For the ellipse shown in this plot, $\lambda = 0.2$ m. 18

2.6 Fat ray method for weighting of pixels included in each link. Each pixel is weighted by the proportion of the link ray that passes through it. This method, however, requires very specific sensor geometry and is not feasible for implementation in RTI. 19

2.7 Received relative reference power in arbitrary dB units versus $\log_{10}(d/d_0)$. The blue x's represent measured power levels at the specified distance, and the dashed line is the computed best-fit line for the data. The path loss exponent and relative reference power can then be computed from the slope and y-intercept, respectively, of this line. The reason the reference level of the decibel units is not specified (i.e. dBm or dBW) is because the RSSI data from the TelosB nodes does not specify the exact reference level being used. 21

2.8 Pixel numbering scheme for a 4 by 4 pixel image. The convention used in this figure (i.e. numbering the pixels row-wise, left to right, starting with the lower left pixel) is the convention used throughout this work. 24

2.9 Test point source image, wherein a single pixel's attenuation value was set to 1 dB, with the other pixels set to 0 dB. The pixel width is 0.5 ft, and the 1 dB pixel's centroid is located at (10.25 ft, 10.25 ft). 27

2.10 Output of the regularization operation given in (2.29) with $\alpha = 2.111$ and $\lambda = 0.0999$ ft used to construct the necessary matrices. Note that the image limits have been scaled by a factor of 0.1 to make the output more visible. . 28

2.11 Normalized standard deviation of each pixel of $\hat{x}_T$, normalized by the noise standard deviation. It can be seen that the standard deviation is lowest near the center of the figure, where the density of link measurements is highest. . 30

2.12 Random test image used to illustrate the regularization process. This image was generated using the correlated shadowing model given in (2.1)-(2.7) with $\sigma_X = 1$ dB, $\delta = 2$ ft, $\sigma_n = 1$ dB. 31

2.13 Estimated image using $\alpha = 2.111$, $\lambda = 0.0999$ ft and sensors placed around the perimeter spaced every 3 ft (28 sensors total). 32

2.14 Estimation error of the test image. Note that for many pixels, the magnitude of the error is comparable to the magnitude of the image itself. 33

2.15 Signal to noise ratio of the image per pixel (unitless). Note that despite the relatively high SNR's observed for many pixels, there is still significant estimation error. 34

2.16 Example modeled received signal strength contour map. The blue "x" represents the hypothetical transmitter location, and the received power contours were generated using the exponential path loss model in (2.19) and shadowing model given in (2.10). Cubic spline interpolation was used to generate a higher resolution image for plotting purposes. 35

2.17 Example modeled received signal strength contour map. The blue "x" represents the hypothetical transmitter location, and the received power contours were generated using the exponential path loss model in (2.19). Cubic spline interpolation was used to generate a higher resolution image for plotting purposes. (This is why the contours look slightly elliptical.) 36

2.18 Example error surface generated from the problem stated in (2.37). The light blue "x" represents the true transmitter location, and the four blue circles (one at each corner of a 21 ft by 21 ft square area) represent anchor node locations. 38

2.19 Visualization of search algorithm. A coarse sampling of the entire objective function is taken, then the algorithm recursively searches at points within a specified radius centered at the last iteration's minimum value. The blue x's represent the points searched when tomography data is included in the RSS model whereas the green x's represent the points searched when tomography data is not accounted for. (The initial coarse sampling over the entire area is the same in both cases.) 41

3.1 Random test image number 1. 44

3.2 Random test image number 2. 45

3.3 Random test image number 3. 45

3.4 Random test image number 4. 46

3.5 Error surface for test image 1 where λ is varied logarithmically from 10^{-3} to 10^{0} and α is varied logarithmically from 10^{-1} to 10^{2}. Note that beyond certain values of λ and α, the surface remains relatively flat, implying that the choice of α and λ have little effect on the MSE after they are raised above those critical values. It is important to note, however, that lower values of α are desirable for the reasons mentioned in the text. 49

3.6 Error surface for test image 2 where λ is varied logarithmically from 10^{-3} to 10^{0} and α is varied logarithmically from 10^{-1} to 10^{2}. Note that when an appropriate value for α is chosen (i.e., in the "trough" on the error surface), the value of λ chosen has little effect on the MSE. 50

3.7 Error surface for test image 3 where λ is varied logarithmically from 10^{-3} to 10^{0} and α is varied logarithmically from 10^{-1} to 10^{2}. Note that when an appropriate value for α is chosen (i.e., in the "trough" on the error surface), the value of λ chosen has little effect on the MSE. 51

3.8 Error surface for test image 4 where λ is varied logarithmically from 10^{-3} to 10^{0} and α is varied logarithmically from 10^{-1} to 10^{2}. Note that beyond certain values of λ and α, the surface remains relatively flat, implying that the choice of α and λ have little effect on the MSE after they are raised above those critical values. 52

3.9 Regularized estimate of test image 1, $\sigma_n = 1$ dB. 53

3.10 Regularized estimate of test image 1, $\sigma_n = \sqrt{10}$ dB. 54

3.11 Regularized estimate of test image 2, $\sigma_n = 1$ dB. 54

3.12 Regularized estimate of test image 2, $\sigma_n = \sqrt{10}$ dB. 55

3.13 Regularized estimate of test image 3, $\sigma_n = 1$ dB. 55

3.14 Regularized estimate of test image 3, $\sigma_n = \sqrt{10}$ dB. 56

3.15 Regularized estimate of test image 4, $\sigma_n = 1$ dB. 56

3.16 Regularized estimate of test image 4, $\sigma_n = \sqrt{10}$ dB. 57

3.17 Average distance error of RSS-based position location estimates as a function of noise standard deviation, with the distance error from 10000 position estimates averaged per noise standard deviation value. For scene generation, $\sigma_X = 1$ dB, $\delta = 2$ ft, $P_{0,dB} = -45$ dB, $n_p = 3$, and $d_0 = 3$ ft were used. . . . 60

3.18 Average distance error of RSS-based position location estimates as a function of noise standard deviation, with the distance error from 2500 position estimates averaged per noise standard deviation value. For scene generation, $\sigma_X = 5$ dB, $\delta = 2$ ft, $P_{0,dB} = -45$ dB, $n_p = 3$, and $d_0 = 3$ ft were used. . . . 61

3.19 Average distance error of RSS-based position location estimates as a function of noise standard deviation, with the distance error from 2500 position estimates averaged per noise standard deviation value. For scene generation, $\sigma_X = 10$ dB, $\delta = 2$ ft, $P_{0,dB} = -45$ dB, $n_p = 3$, and $d_0 = 3$ ft were used. . . 62

4.1 Approximate measurement geometry for scene 1. Used under fair use, 2011. . 67

4.2 South-facing view from the western boundary of scene 1. 68

4.3 North-facing view from the western boundary of scene 1. 69

4.4 South-facing view from the northeastern corner of scene 1. 70

4.5 Measurement geometry for scene 2. Sensor node locations (N0 through N27 are the sensor nodes numbered in a clockwise fashion as shown in the figure) are denoted by the circles around the perimeter of the area. Test "free node" locations are designated as T1 through T4 (their use will be explained in a later section). 71

4.6 Photograph of deployed network at scene 2, taken from outside the network on the left side of Figure 4.5, facing in the x-direction. 72

4.7 Approximate measurement geometry for scene 3. Used under fair use, 2011. . 74

4.8 North facing view from the southern corner (the origin of the coordinate system) of scene 3. 75

4.9 Estimated image for scene 1 (empty). 77

4.10 Estimated image for scene 2 (empty). 78

4.11 Estimated image for scene 3 (empty). 79

4.12 RSS versus log-distance for scene 1 (empty). 81

4.13 RSS versus log-distance for scene 2 (empty). 82

4.14 RSS versus log-distance for scene 3 (empty). 83

4.15 Histogram of RSS estimation error without using RTI for scene 1 (empty). . 84

4.16 Histogram of RSS estimation error with using RTI for scene 1 (empty). . . . 85

4.17 Q-Q Plot of RSS estimation error (with using RTI) versus normal distribution for scene 1 (empty). The dashed blue line (which has a slope of 1) is plotted for reference. 86

4.18 Location estimates with and without tomography for node position 1 in scene 2. The blue circles represent anchor node locations. 90

4.19 Scatter plot of distance error with RTI versus distance error without RTI for the perimeter node experiments performed in scene 1. The least-squares fit line for the data is shown in grey. 92

4.20 Scatter plot of distance error with RTI versus distance error without RTI for the perimeter node experiments performed in scene 2. The least-squares fit line for the data is shown in grey. 93

4.21 Scatter plot of distance error with RTI versus distance error without RTI for the perimeter node experiments performed in scene 3. The least-squares fit line for the data is shown in grey. 94

A.1 Histogram of RSS estimation error without using RTI for scene 1 (empty). . 100

A.2 Histogram of RSS estimation error with RTI for scene 1 (empty). 101
A.3 Q-Q Plot of RSS estimation error versus normal distribution for scene 1 (empty).102
A.4 Histogram of RSS estimation error without using RTI for scene 2 (empty). . 103
A.5 Histogram of RSS estimation error with RTI for scene 2 (empty). 104
A.6 Q-Q Plot of RSS estimation error versus normal distribution for scene 2 (empty).105
A.7 Histogram of RSS estimation error without using RTI for scene 3 (empty). . 106
A.8 Histogram of RSS estimation error with RTI for scene 3 (empty). 107
A.9 Q-Q Plot of RSS estimation error versus normal distribution for scene 3 (empty).107

B.1 Location estimates with and without tomography for node position 1 in scene 2. The blue circles represent anchor node locations. 109
B.2 Location estimates with and without tomography for node position 2 in scene 2. The blue circles represent anchor node locations. 110
B.3 Location estimates with and without tomography for node position 3 in scene 2. The blue circles represent anchor node locations. 111
B.4 Location estimates with and without tomography for node position 4 in scene 2. The blue circles represent anchor node locations. 112
B.5 Location estimates with and without tomography for node position 1 in scene 3. The blue circles represent anchor node locations. 113
B.6 Location estimates with and without tomography for node position 2 in scene 3. The blue circles represent anchor node locations. 114
B.7 Location estimates with and without tomography for node position 3 in scene 3. The blue circles represent anchor node locations. 115
B.8 Location estimates with and without tomography for node position 4 in scene 3. The blue circles represent anchor node locations. 116
B.9 Location estimates with and without tomography for node position 5 in scene 3. The blue circles represent anchor node locations. 117

C.1 Histogram of localization errors for the network deployed in scene 1 utilizing tomography data. 119
C.2 Histogram of localization errors for the network deployed in scene 1 without utilizing tomography data. 119

C.3 Histogram of localization errors for the network deployed in scene 2 utilizing tomography data. 120
C.4 Histogram of localization errors for the network deployed in scene 2 without utilizing tomography data. 120
C.5 Histogram of localization errors for the network deployed in scene 3 utilizing tomography data. 121
C.6 Histogram of localization errors for the network deployed in scene 3 without utilizing tomography data. 121

List of Tables

4.1 RSS estimation error statistics without (EXP) and with (RTI) tomography. . 87
4.2 Position location performance for scene 2. 89
4.3 Position location performance for scene 3. 89
4.4 Position location performance for perimeter node experiments. 91

Chapter 1

Introduction

1.1 Introduction

Radio Tomographic Imaging (RTI) is an emerging field that uses received signal strength (RSS) measurements made around the perimeter of an area of interest to reconstruct an image (usually two-dimensional) of objects in the enclosed area [4]. In this specific brand of radio tomography, narrowband sensors are used to characterize the region at a single frequency. This approach does not require phase synchronization between transceivers.

The ability to reconstruct two-dimensional images from RSS measurements between links on the perimeter of the area arises from the fact that attenuating objects in the paths of each link will create correlated link shadowing that can be exploited to estimate the positions of the attenuating objects [5]. The capability to remotely measure the location and relative strengths of attenuating objects can be very useful for a variety of applications, including radio coverage prediction and received signal strength-based methods of trilateration.

Naturally, RTI shares many similarities with other methods of remote sensing and wireless channel modeling. To elucidate the context in which RTI lies, a summary of these methods will be compared and contrasted with RTI. A full enumeration of every aspect of these topics is not going to be attempted– instead only those points that relate to the work of radio tomographic imaging pursued in this thesis will be compared.

1.2 Inverse Problems

As the reader may have noted, RTI shares similarities with many other fields, such as medical imaging and remote sensing, in the sense that electromagnetic waves are to probe an an environment to infer descriptive parameters that characterize the system. In applied math-

ematics literature this is referred to as *inverse problem theory.* This is contrasted with the *forward, modeling,* or *simulation problem*, wherein a parametric description of a system can be used to simulate any hypothetical measurement [6].

It is instructive to view RTI in this context because it reveals its relative advantages and disadvantages as compared to other methods, and it also allows one to utilize advancements in related fields to improve the methods used in radio tomography. Related fields include medical imaging (especially computed tomography), remote sensing (such as radar and geophysical applications), wireless channel modeling, and position location.

1.2.1 Medical Imaging

In conventional Computed Tomography (CT), there are two main classes of algorithms: algebraic reconstruction techniques and Fourier-based reconstruction techniques. Algebraic reconstruction techniques formulate the problem as an inverse linear estimation problem, whereas Fourier-based techniques map measurement data to points in a Fourier space, which is then inverted to obtain an image of the original object. Neither method requires phase-information for the received signals [1].

Fourier Tomography

Historically, medical CT imaging has relied on the class of imaging tools we will hereafter refer to as Fourier tomography. The core feature of two-dimensional Fourier tomography is the Fourier Slice Theorem, which relates attenuation measurements made around the perimeter of a circular area to the Fourier transform of the "object function" of the attenuating object [1], which will be further described herein.

Consider the coordinate systems shown in Figure 1.1. Note that the t–s coordinate system is a rectangular coordinate system rotated counterclockwise by θ from the x–y system. The relationship between points in the two coordinate systems is given by:

$$\begin{bmatrix} t \\ s \end{bmatrix} = \begin{bmatrix} \cos\theta & \sin\theta \\ -\sin\theta & \cos\theta \end{bmatrix} \begin{bmatrix} x \\ y \end{bmatrix} \tag{1.1}$$

or, to convert a point in the t–s frame back to the x–y frame:

$$\begin{bmatrix} x \\ y \end{bmatrix} = \begin{bmatrix} \cos\theta & -\sin\theta \\ \sin\theta & \cos\theta \end{bmatrix} \begin{bmatrix} t \\ s \end{bmatrix} \tag{1.2}$$

The attenuation experienced as an electromagnetic wave propagates through the object in a direction parallel to the s-axis (constant t) may be expressed as a line integral of the

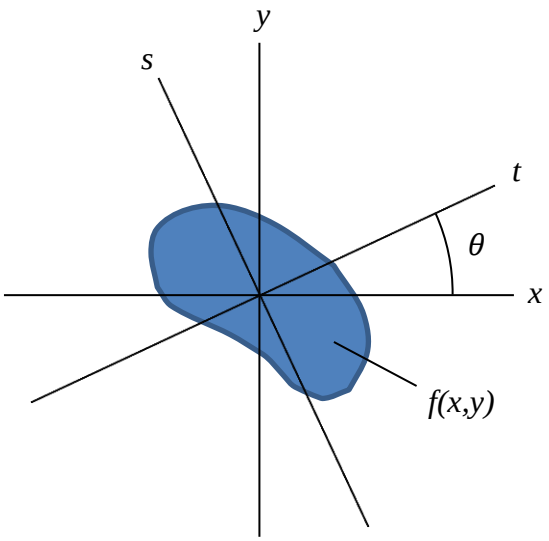

Figure 1.1: Coordinate geometry used in deriving the Fourier Slice Theorem. The attenuating object is expressed as an object function $f(x, y)$, which in the case of RTI, represents the value of the electromagnetic attenuation coefficient in decibels per unit length. Adapted from [1].

scalar-valued object function as follows:

$$P_\theta(t) = \int_{-\infty}^{\infty} f(x(t,s), y(t,s))\, ds. \tag{1.3}$$

The function $P_\theta(t)$ is known as the Radon transform of the function $f(x,y)$ [1].

The Fourier transform of $P_\theta(t)$ is given by:

$$S_\theta(w) = \int_{-\infty}^{\infty} P_\theta(t) e^{-j2\pi wt}\, dt, \tag{1.4}$$

which, after substituting (1.3) into (1.4) and using the Jacobian determinant to change the variables of integration, becomes:

$$\begin{aligned} S_\theta(w) &= \int_{-\infty}^{\infty} f(x,y) e^{-j2\pi w(x\cos\theta + y\sin\theta)}\, dx\, dy \\ &= F(w\cos\theta, w\sin\theta) = F(u,v), \end{aligned} \tag{1.5}$$

where $F(w\cos\theta, w\sin\theta)$ is the Fourier transform of the object function $f(x,y)$ evaluated at the points $u = w\cos\theta$ and $v = w\sin\theta$. This result, which relates the measured attenuation data to the Fourier transform of the object function, is known as the Fourier Slice Theorem, and is the basis of two-dimensional Fourier tomography.

The derivation shown in (1.1)-(1.5) is valid for parallel projection data, i.e., where incident rays are all parallel for each value of θ. Reconstruction algorithms for data obtained from sources that radiate omnidirectionally ("fan beams") are also available, but their derivation is beyond the scope of this work [1].

The disadvantage of this method lies in the fact that a large number of radial views are required for accurate image formation, and the estimation process does not take into account noise statistics. As well, the complexity of the reconstruction algorithm makes adaptation for arbitrary sensor network geometries difficult. Since our application will typically involve varied sensor geometries, we have not explored this approach further.

Algebraic Reconstruction Methods

As was stated earlier, algebraic reconstruction methods formulate the imaging problem as a linear estimation problem. The problem can be expressed as follows:

$$y = Wx + n, \tag{1.6}$$

where $y \in \mathbb{R}^M$ is the measurement vector containing the measured attenuations for each of the M rays, $x \in \mathbb{R}^N$ is an (unknown) image vector that contains the attenuation value for

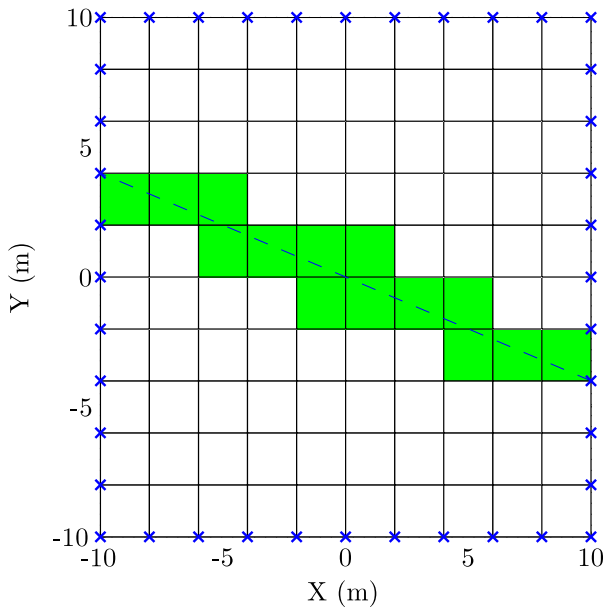

Figure 1.2: Pixel selection scheme used by algebraic methods. The blue x's represent sensor locations, the dashed line represents a single measurement ray, and the green pixels represent the pixels that affect the attenuation experienced by that ray. Adapted from [2].

each of the N pixels in units of dB/pixel, $W \in \mathbb{R}^{M \times N}$ is a known matrix that relates each ray to the pixels it passes through, and $n \in \mathbb{R}^M$ is a noise vector [2].

Consider the diagram shown in Figure 1.2, wherein the pixels that contribute to the attenuation experienced by each ray are shown. Note that due to the pixelated nature of the image domain, some method must be used to select which pixels provide a significant contribution. Multiple methods have been proposed, such as the "fat-ray" method, wherein each ray is assigned a finite width and the weight assigned to each pixel is given by the percentage of pixel area covered by that ray [1] and the "weighted ellipse" method, wherein an ellipse is drawn with the foci located at the source and detector locations, and the pixels whose centroids lie outside the ellipse are given zero weight [2].

As well, multiple schemes have been proposed for solving the inverse problem described by (1.6). Due to the large matrix sizes, direct methods for inversion or least-squares estimation may be impractical. Traditional algebraic methods used in medical x-ray tomography have relied on iterative methods such as ART (Algebraic Reconstruction Techniques), SIRT (Simultaneous Iterative Reconstructive Technique), and SART (Simultaneous Algebraic Reconstruction Technique) [1].

The advantage of algebraic methods lies in their conceptual simplicity, which make them easily adaptable to irregular geometries or cases where the number of measurements made

are small, such as in geophysical sensing applications [1]. As well, it has been noted that algebraic methods are useful in cases where media are weakly diffracting or refracting (as compared to Fourier tomography, which assumes no ray-bending).

The class of algorithms proposed by Patwari [5], Wilson [4], and others of the SPAN Lab at the University of Utah referred to as "Radio Tomographic Imaging" can be considered algebraic reconstruction methods. The difference between algebraic radio tomographic imaging and the algorithms used in medical tomography is that the radio tomography algorithms take into account noise statistics, largely due to the fact that multipath interference (which is treated as noise) is much more prominent at the longer wavelengths used in radio tomography.

In addition, due to the fact that the quantities being measured are the location and strength of attenuating objects, this method can be used to predict received signal strength for radio coverage prediction applications. This subject will be dealt with later in this chapter.

Due to the flexibility and simplicity of algebraic radio tomography methods, it was the method of choice for imaging used in this thesis. Further description of this method and the assumptions therein will be given in the following chapter.

1.2.2 Diffraction Tomography

As was mentioned previously, conventional tomography algorithms (Fourier and algebraic methods) generally assume that there is either no diffraction, or small amounts of it, and any multipath that exists is treated as noise. The appeal of this approach is that it does not require phase information; only received signal strength is required, which lends itself to implementation on less-complex devices.

Diffraction tomography, by contrast, takes advantage of phase information to provide a more accurate image estimate. However, the quantity being measured is the ability of the object to scatter electromagnetic waves (like radar), rather than its ability to transmit them (like x-ray tomography).

The fundamental theoretical result that underlies diffraction tomography is the Fourier Diffraction Theorem- which relates phasor measurements of scattered electromagnetic wave components taken at different points in space to the three-dimensional Fourier transform of the object's scattering properties [1, 7]. Because of this, it is conceptually similar to two-dimensional Fourier tomography.

Others in the field [8–13] have used a similar approach for diffraction tomography, with the exception that they use a more advanced method based on the use of dyadic Green's functions and use different inversion methods other than the IFFT, but the concept is similar.

Because diffraction tomography does not measure the attenuation properties of the objects it images, it is ill-suited to the tasks of wireless channel modeling and radio coverage pre-

diction. However, it does afford the possibility of greater image quality than algebraic radio tomography because of the inclusion of more advanced concepts from electromagnetic theory.

1.2.3 Wireless Channel Modeling

In addition to the field of remote sensing, RTI can be used for wireless channel modeling purposes, i.e., if the tomographic image for an area of interest is taken, one may predict the shadowing present in the environment and obtain more accurate estimates for radio coverage prediction than traditional statistical or empirical models can provide.

The motivation for statistical and empirical models lies in the fact that the complex and time-varying geometries involved in mobile radio channels make it practically impossible to obtain solutions to Maxwell's equations to model the effect the channel has on the signal [14]. A brief survey of these simpler methods will be given.

Deterministic Models

A variety of deterministic models of varying complexity have been proposed. Generally, these models account for path loss and shadowing (large-scale fading) but do not always account for the effect of multipath interference (small-scale fading).

The simplest model to account for path loss in a wide variety of environments is the exponential path loss model. The average received power, P_r, as a function of distance, d, is given by:

$$P_r = P_0 \left(\frac{d}{d_0} \right)^{-n_p}, \tag{1.7}$$

where n_p is known as the path loss exponent, and P_0 is the average power level measured at distance d_0 from the transmitter [5, 15].

While the exponential path loss model is flexible enough to be used in a wide variety of situations, its simplicity is also its weakness. A number of empirical (Okumura, Hata, etc) models have been proposed that add additional terms/factors to improve estimates based on measurement data [14]. Others, like the Longley-Rice model [16], ray-tracing [14], and Geometrical Theory of Diffraction (GTD) [17] use simplifications of Maxwell's equations to approximate a solution.

These models can provide accurate results if detailed knowledge of the site is known. However, if the mobile device is expected to encounter a wide variety of environments that may change quickly with time, statistical models will likely be more useful.

Statistical Models

When propagation characteristics of the specific site of interest are not known, statistical models can be very useful. Usually, only a few parameters (such as mean and variance) need to be estimated, which leads to easy implementation. These models also allow communications engineers to design the system to meet a certain level of performance despite random fluctuations in signal strength given that the statistical properties are measurable.

For large-scale fading, a log-normal distribution is used to model the effect of shadowing objects. This assumption is based on the fact that over the course of a long signal path, the signal power is affected by a series of multiplicative attenuating factors (additive when using dB units). If each of these attenuations is considered to be an independent, identically distributed random variable, then by the central limit theorem, the total attenuation (in dB) will approach a Gaussian distribution for a large number of attenuations [14].

For small-scale fading, the Rayleigh and Rician distributions are commonly used to model dense multipath fading. While a full derivation of the assumptions used in these models will not be given here, they are derived using the fact that narrowband signals generally have low delay spread and consequently multipath components will arrive at the receiver at roughly the same time, causing constructive and destructive interference. Rayleigh fading assumes no line of sight path, whereas Rician fading accounts for a line of sight ray. In cases where neither model is satisfactory, the Nakagami fading model was developed for better agreement with certain empirical results, and it is the most general of the three aforementioned statistical models [14].

Other statistical models [5, 18] account for the fact that shadowing between links may be correlated if the links share similar paths. This model will be the basis for the statistical estimators used in the following chapter.

1.2.4 Position Location

While there are many methods for position location, most require either tight synchronization between nodes (time of arrival, time-difference of arrival), or directional antennas (angle of arrival) [19]. Received signal strength (RSS) methods have the advantage that they are the easiest to implement (requiring only signal strength measurements between nodes), but are the most prone to error. An explanation of this method will be given herein.

Consider the diagram shown in Figure 1.3. Using an equation such as (1.7), one can relate a measured signal strength from a radio source to its distance from the receiver. Geometrically, this means that the target of interest will lie on a circle whose radius is determined by (1.7). When three nodes of known location (anchor nodes) perform this procedure, the mobile node's location is given by the intersection of the three circles.

However, when signal strength measurements deviate from those predicted by (1.7), the

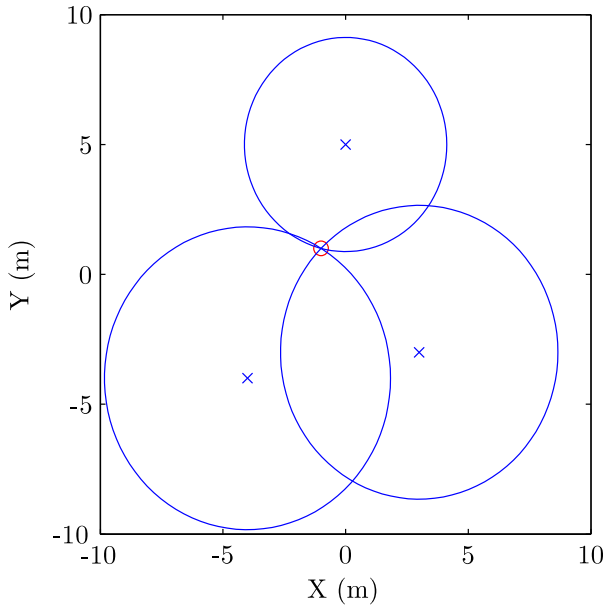

Figure 1.3: Geometry for a noiseless RSS-based positioning system. The blue x's represent anchor node locations, while the red circle represents the free node to be located.

ranging circles in Figure 1.3 will not intersect. In these cases, a least-squares or maximum likelihood method must be used to find the point that is the most probable location of the mobile node [3].

A further discussion of the combination of this method with the additional data given by RTI will be given in the following chapter.

1.3 Problem Statement

The goal of the research is to apply RTI for the purpose of obtaining an attenuation field for a given area from sensor measurements, and then to utilize this information for improving radio coverage and position location estimates, among other things.

Because the only quantity required for RTI is received signal strength, a larger number of low-cost sensors may be used to make a very dense sensor network. It should also be noted that since essentially every mobile radio already measures RSS, these techniques could possibly be implemented in existing networks, such as Wi-Fi or cellular networks.

The object of interest to be measured is the attenuation field for a given region. This would measure the shadowing caused by large objects in the region of interest, such as trees, hills, or buildings. An example attenuation field is shown in Figure 1.4. The attenuation field

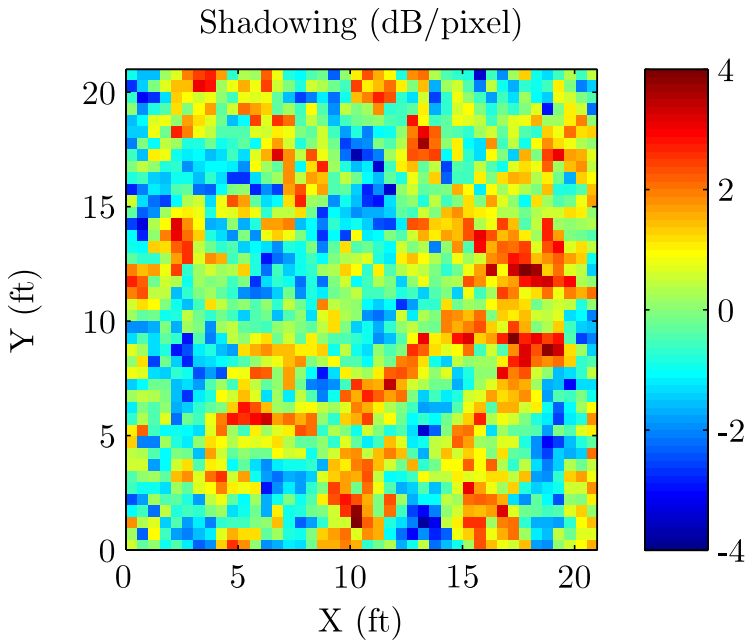

Figure 1.4: Example random attenuation field produced using a correlated shadowing model.

shows the shadowing (in dB per pixel) of a given region as a function of position. In this work, it will be assumed that the attenuation field shows the variation from the mean signal strength (as determined by the exponential path loss model in (1.7)), so it is possible to have pixels in the attenuation field that have negative attenuation in dB. This information can be used as an aid to cellular network planning.

1.4 Applications

The simplicity and flexibility of RTI combined with the near ubiquitous ability of wireless devices to measure and record RSS data allow for widespread application of this technology. The following are example networks where RTI may be implemented in the future:

- Military Units - A squad or platoon of soldiers (each with a radio tranceiver) may surround a building, and the RTI network can provide the locations of persons within the building, and if the protocol used by enemy radios is known, locate them to a high degree of precision.
- WiFi - Many buildings today are filled with WiFi access nodes and large numbers of WiFi-capable devices. If these devices were modified so that they measured RSS data between nodes not in the current local area network, RTI could be implemented in

these situations. This additional channel information could potentially improve the quality of data transmissions over these networks.

- Cellular Networks - Similar to the application to WiFi networks, cellular network infrastructure and devices may be used for the same purpose. As well, if RTI data has been obtained for a given area, this can aid in network planning, as has been previously mentioned.
- Cognitive Radio - As the aforementioned devices implement more "cognitive" features in their designs, collaborative artificial intelligence in these networks may be used to further optimize transmission characteristics with the additional information provided by RTI.

1.5 Original Contributions and Outline of Thesis

While many others have proposed using RTI for object/motion tracking [2, 4, 5, 20–22], the author is not aware of serious efforts to investigate the viability of using RTI for radio coverage planning. As well, the technique of utilizing RTI data to improve RSS-based position location methods, while proposed by Callaway and others in 2004 [23], has not been pursued seriously to the author's knowledge.

The remainder of the thesis will be as follows:

- Chapter 2: Mathematical Methods for Radio Tomographic Imaging
- Chapter 3: Computer Simulations and Proof of Concept
- Chapter 4: Experimental Verification
- Chapter 5: Conclusion

Chapter 2

Mathematical Methods for Radio Tomographic Imaging

2.1 Introduction

The purpose of this chapter will be to explain the mathematical imaging algorithms used in radio tomographic imaging as well as the combination of RTI with RSS-based position location algorithms. While the RTI estimation algorithms are essentially the same as those used by Wilson and Patwari [4, 5], a more detailed explanation of the algorithms than was given in the previous chapter will be given so that the reader understands the fundamentals of RTI.

However, as was mentioned previously, the application of RTI to attenuation field estimation for radio coverage prediction as well as the combination of RTI with RSS-based position location techniques are new problems that have not been explored seriously to this point. Topics discussed in this chapter are the assumed statistical model of the attenuation field, the formulation of the linear estimation problem, statistical estimators used, regularization methods for matrix inversion, attenuation field estimation, position location algorithms, and potential applications.

2.2 System Model

Consider the diagrams shown in Figures 2.1-2.2. Sensor locations are denoted by blue "X"s, an attenuating object is represented by the green circle, and the blue lines between sensor locations represent line-of-sight radio links between nodes. The radio sensors used by the author in this thesis were TelosB motes produced by MEMSIC, Inc. utilizing the IEEE 802.15.4 ZigBee standard. As was mentioned previously, the advantage of the algebraic RTI

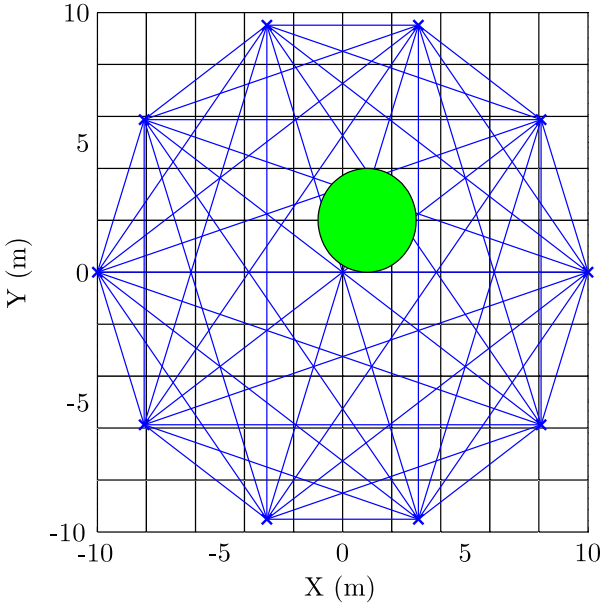

Figure 2.1: An example of a circular RTI geometry. The blue "X"s represent sensor node locations, the blue lines represent radio links between nodes, the green circle represents an attenuating object, and the white boxes represent pixel locations.

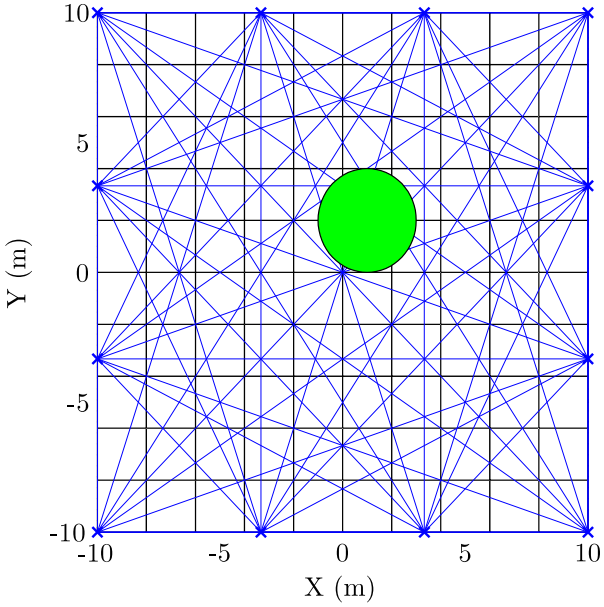

Figure 2.2: An example of a square RTI geometry.

method chosen was that it allows for flexibility in the network geometry used– essentially any network geometry can be used provided that the sensor locations are known. Figures 2.1-2.2 show example circular and square geometries, respectively.

2.2.1 Correlated Shadowing Model

Note that in Figure 2.2, multiple links cross the same attenuating object (the green circle). This gives rise to the fact that the shadowing on those links will experience a high degree of correlation, a fact that has been ignored in the standard log-normal shadowing model, wherein each link's shadowing component is assumed to be independent [5].

The correlated shadowing model utilized in this thesis is based on the one proposed by Patwari [5], which assumes that the environment consists of a scalar "spatial attenuation field", $p(x)$, with units of dB/m, where $x \in \mathbb{R}^2$ is the position coordinate vector. The attenuation field $p(x)$ is assumed to be an isotropic, wide-sense stationary, zero-mean Gaussian random process with a spatial autocorrelation given by:

$$E\left[p(x_i)p(x_j)\right] = R_p(d_{i,j}) = \frac{\sigma_X^2}{2\delta} e^{-\frac{d_{i,j}}{\delta}}, \tag{2.1}$$

where $d_{i,j} = \parallel x_i - x_j \parallel$ is the distance between observation points $x_i, x_j \in \mathbb{R}^2$, δ is a spatial constant, and σ_X^2 is roughly the variance of the shadowing experienced on link (i, j).

The importance of this model to RTI is multi-fold. First, the correlated shadowing model provides a more realistic model for random scene generation for simulation purposes than the uncorrelated log-normal shadowing model provides. Secondly, the model aids in determining the relationship between the attenuating pixels and the links that cross through them that will be explained later in this chapter. Lastly, knowledge of the covariance matrix is of use if one utilizes a Bayesian approach to estimating the attenuation field [24].

The shadowing on link (i, j) is therefore the scalar line integral of the attenuation field between x_i and x_j, and is expressed by:

$$X_{i,j} = \frac{1}{\sqrt{d_{i,j}}} \int_{x_i}^{x_j} p(x)\, ds, \tag{2.2}$$

where $ds = \parallel dx \parallel$ is the differential path length, and the factor $1/\sqrt{d_{i,j}}$ is included so that the variance of link shadowing is roughly constant with distance [5]. This can be seen by the following:

$$\begin{aligned} \mathrm{Var}\left[X_{i,j}\right] &= E\left[\frac{1}{d_{i,j}} \int_{x_i}^{x_j} p(x)\, ds_1 \int_{x_i}^{x_j} p(y)\, ds_2\right] = \frac{1}{d_{i,j}} \int_{x_i}^{x_j} \int_{x_i}^{x_j} E\left[p(x)p(y)\right]\, ds_1 ds_2 \\ &= \frac{1}{d_{i,j}} \int_{x_i}^{x_j} \int_{x_i}^{x_j} R_p(\parallel y - x \parallel)\, ds_1 ds_2. \end{aligned} \tag{2.3}$$

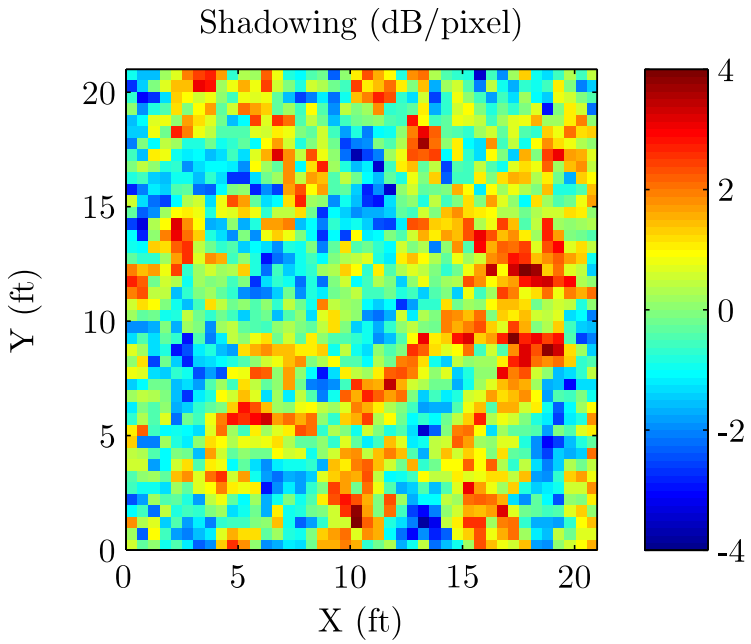

Figure 2.3: Random scene generated using the correlated shadowing model with $\sigma_X = 2$ dB and $\delta = 1$ ft. Note that each pixel is only slightly correlated with neighboring pixels.

The integral in (2.3) can be solved by parameterizing x and y as functions of an intermediate variable using the following process:

$$x(t_1) = x_i + t_1(x_j - x_i) \tag{2.4}$$

$$\Rightarrow \frac{dx}{dt_1} = x_j - x_i$$

$$\Rightarrow \left|\left|\frac{dx}{dt_1}\right|\right| = \| x_j - x_i \| = d_{i,j} \tag{2.5}$$

$$\Rightarrow ds_1 = \| dx \| = \left|\left|\frac{dx}{dt_1}\right|\right| dt_1 = d_{i,j}\, dt_1. \tag{2.6}$$

The same procedure can be used to parameterize y as a function of t_2. Substituting (2.1) and (2.6) into (2.3) and solving the resulting double integral yields:

$$\mathrm{Var}\left[X_{i,j}\right] = \sigma_X^2 \left[1 - \frac{\delta}{d_{i,j}}\left(1 - e^{-d_{i,j}/\delta}\right)\right] \approx \sigma_X^2, \tag{2.7}$$

where the approximation is valid when $d_{i,j} \gg \delta$.

It can also be deduced from (2.2) that since $p(x)$ is Gaussian-distributed, $X_{i,j}$ will also be Gaussian-distributed because the integral is a linear operation on $p(x)$ [25].

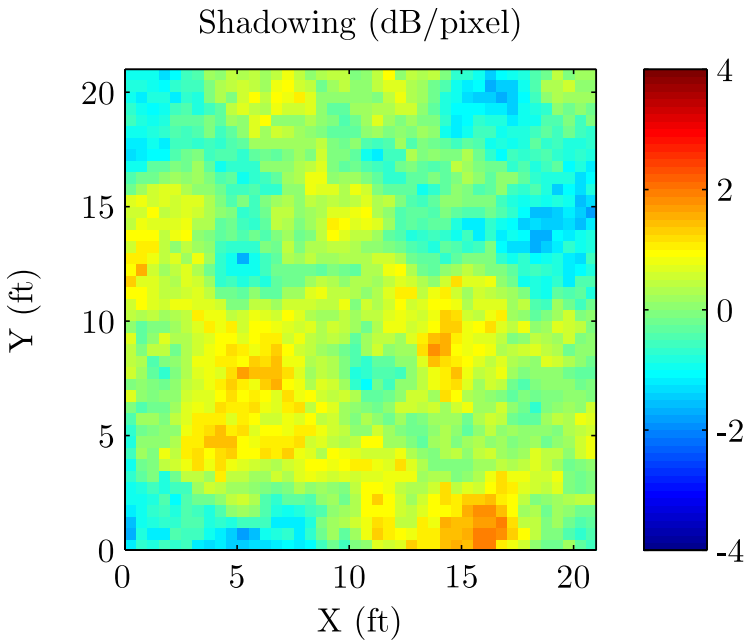

Figure 2.4: Random scene generated using the correlated shadowing model with $\sigma_X = 2$ dB and $\delta = 4$ ft. Note that each pixel is highly correlated with neighboring pixels.

To provide a visual illustration, Figures 2.3-2.4 were generated using a zero-mean Gaussian random vector with covariance matrix computed from (2.1) with a pixel width of 0.5 ft, $\sigma_X = 2$ dB, $\delta = 1$ ft for Figure 2.3, and $\delta = 4$ ft for Figure 2.4. It can be seen that the larger the value of δ, the more correlated each pixel is with neighboring pixels.

2.2.2 Linear Problem Formulation

As has been previously implied, an RTI sensor network must consist of an array of self-localized nodes that have the ability to transmit and receive radio signals and determine received signal strength from each source. Phase and timing information is not required.

For a network consisting of K wireless sensor nodes, the number of unique radio links, M, is given by the arithmetic series:

$$M = \sum_{k=1}^{K-1} k = \frac{K(K-1)}{2}. \tag{2.8}$$

The received signal strength, $y_i(t)$, in dB power units (such as dBW or dBm), for a given sensor link, i is given by [4]:

$$y_i(t) = P_i - L_i - S_i(t) - F_i(t) - \nu_i(t), \tag{2.9}$$

with:

- P_i: Transmit power for the link, in dB units.
- L_i: Losses due to antenna patterns, path loss, and other static factors.
- $S_i(t)$: Shadowing loss due to obstructing objects.
- $F_i(t)$: Fading loss due to multipath.
- $\nu_i(t)$: Measurement noise.

For the two-dimensional imaging case, the area of interest can be divided up into N pixels, each of which is considered a shadowing attenuator. The total amount of shadowing for a link is given by:

$$S_i(t) = \sum_{j=1}^{N} w_{ij} x_j(t), \tag{2.10}$$

where $x_j(t)$ is the attenuation value for pixel j at time t, and w_{ij} is the weighting for pixel j along link i. If a particular link is not affected by a certain pixel, the weight for that pixel is set to zero for that link [4].

To formulate the problem as a system of linear equations, the expression in (2.9) may be rewritten as:

$$y_i(t) = -\sum_{j=1}^{N} w_{ij} x_j(t) + n_i(t), \tag{2.11}$$

with:

$$n_i(t) = P_i - L_i - F_i(t) - \nu_i(t). \tag{2.12}$$

This model has been used previously to image moving objects by estimating the change in RSS for each link over time to remove the effect of static objects [4]. In this paper, however, we will consider the static case because our application of interest is network planning, wherein it is desirable to know the positions of attenuating objects.

For the static case, the system of equations described by (2.11) may be succinctly expressed as a linear estimation problem:

$$y = Wx + n \tag{2.13}$$

where:

$$\begin{aligned} y &= [y_1, y_2, \ldots, y_M]^T, \\ x &= [x_1, x_2, \ldots, x_N]^T, \\ n &= [n_1, n_2, \ldots, n_M]^T, \end{aligned} \tag{2.14}$$

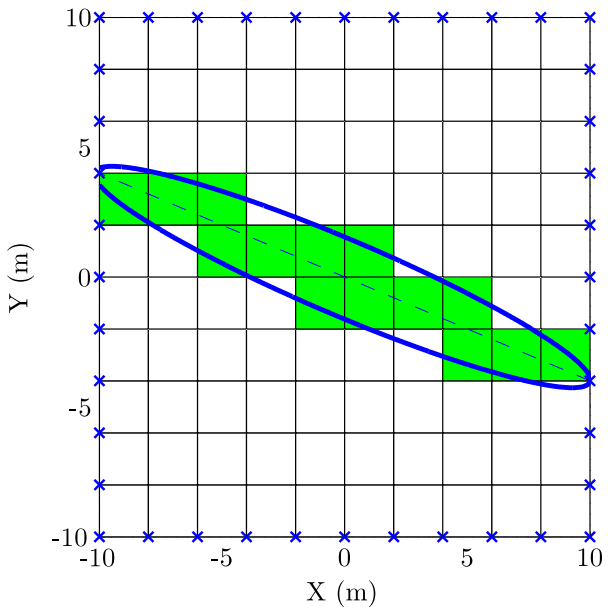

Figure 2.5: Ellipse method for selecting which pixels are included in a given link. The dashed blue line represents a radio link, and the green pixels are those whose centroid falls within the ellipse (whose focii lie at the node locations). For the ellipse shown in this plot, $\lambda = 0.2$ m.

and

$$[W]_{i,j} = -w_{ij}, \quad W \in \mathbb{R}^{M \times N}. \tag{2.15}$$

The matrix W defines the relationship between each pixel (elements of the vector x) and the links (elements of y) that are affected by the attenuation in those pixels. There are several ways of determining the values of the elements of W, but only two will be explained here.

One method for determining the weighting matrix W is, for each link, to use an ellipse with its foci located at the sensor node locations as the selection criteria. If and only if the centroid of a pixel falls within the ellipse, it is given a non-zero weighting value. This may be expressed mathematically as:

$$w_{ij} = \begin{cases} \frac{1}{\sqrt{d}}, & \text{if } d_{ij}(1) + d_{ij}(2) < d + \lambda, \\ 0, & \text{otherwise,} \end{cases} \tag{2.16}$$

where d is the distance between the two nodes, $d_{ij}(1)$ is the distance from the first node of link i to the centroid of pixel j, $d_{ij}(2)$ is the distance from the second node of link i to the centroid of pixel j, and λ is a tunable parameter that changes the width of the ellipse [4]. The reason for weighting each link by $1/\sqrt{d}$ is so that (2.10) conforms with the correlated shadowing model given by (2.1)-(2.3). This weighting scheme ensures that the link shadowing variance is roughly constant with distance [5].

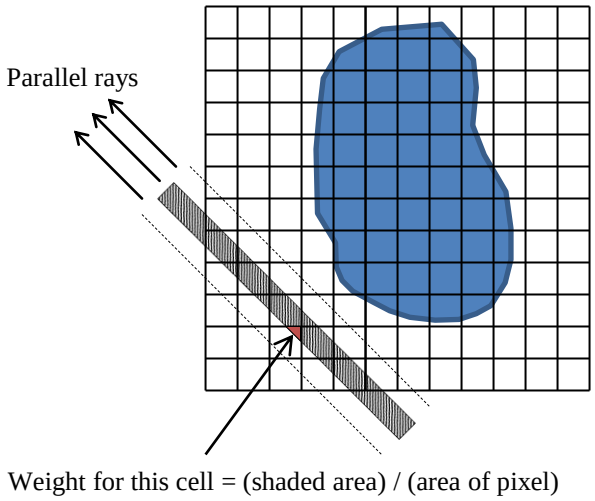

Figure 2.6: Fat ray method for weighting of pixels included in each link. Each pixel is weighted by the proportion of the link ray that passes through it. This method, however, requires very specific sensor geometry and is not feasible for implementation in RTI.

An illustration of this method is shown in Figure 2.5, where the green pixels represent those pixels that are included in the given link. This is the primary method used by Wilson and Patwari [4] in their later work in RTI.

One of the primary methods for determining the matrix W in conventional medical tomography literature is called the "fat-ray" method, wherein the link lines are considered to have finite width and the weights are determined by the proportion of the pixel area covered by each ray [1]. This method assumes that each link line (where attenuation is measured) emanating from a source is parallel, an assumption that may have been valid for early CT systems where the x-ray source/detector pairs slid on rotating parallel tracks, but is not directly applicable to RTI because of the network geometries involved. An illustration of this method is shown in Figure 2.6.

2.2.3 Noise Models

A brief explanation of the possible distributions for the noise term given by (2.12) will be undertaken. The importance of selecting a proper noise distribution lies in the fact that statistical estimators used to estimate the image vector, x, rely on the assumed noise statistics.

Of the terms in (2.12), P_i and L_i are deterministic, and therefore will only contribute to the mean of n_i. An appropriate distribution to account for the multipath fading experienced by

each link could be either a Rician or Nakagami random variable (Rayleigh fading is excluded in this case because it does not account for the possibility of a line-of-sight ray) [14]. However, it should be noted that because these distributions account for changes in amplitude due to fading, they must be converted to decibels to be used in (2.12) using the following:

$$F_i(t) = 20 \log_{10} \left(f_i(t) \right), \tag{2.17}$$

where $f_i(t)$ is the assumed fading distribution.

The term $\nu_i(t)$ is included to account for any signal strength variations aside from fading. Included in this term are:

- Quantization noise (the sensors used in this thesis report RSS in steps of 1 dB).
- Interference from other devices in the 2.4 GHz band.
- Any other measurement noise.

The problem of accurately creating an analytical model for the noise distribution, $n_i(t)$, from the contributions of each of the individual terms makes it desirable to use a simpler model. In their initial paper on this topic, Patwari and Agrawal assume a Gaussian (in dB) noise model, justifying this choice by the fact that for a wideband signal, the receiver effectively averages several narrowband fading terms, leading to an approximately Gaussian distribution [5]. Later, Wilson and Patwari propose using a two-component Gaussian mixture model, with strong empirical support for such, but note that using a single Gaussian random variable is still a good approximation of the empirical probability distribution function (PDF) within roughly 2.5 quantiles on a quantile-quantile plot [4].

For these reasons, and for simplicity of analysis in constructing a statistical estimator, we will assume a one-component Gaussian noise model with $n \sim \mathcal{N}(m, C)$, where the elements of the mean vector $m \in \mathbb{R}^M$ are given by:

$$m_i = P_i - L_i, \tag{2.18}$$

which is purely deterministic, and $C \in \mathbb{R}^{M \times M}$ is the covariance matrix of n.

2.2.4 Path Loss Exponent Estimation

As was mentioned previously, the noise model we are using assumes that $E[n] = m$ is purely deterministic and is given by (2.18). However, because we do not know the exact transmit power, antenna gains, path loss, or other static parameters, we will use the simplified exponential path loss model to determine the values of the elements of m. When (1.7) is converted to decibels, is may be expressed as [5]:

$$P_{r,dB}(d) = P_{0,dB} - 10 n_p \log_{10} \left(\frac{d}{d_0} \right). \tag{2.19}$$

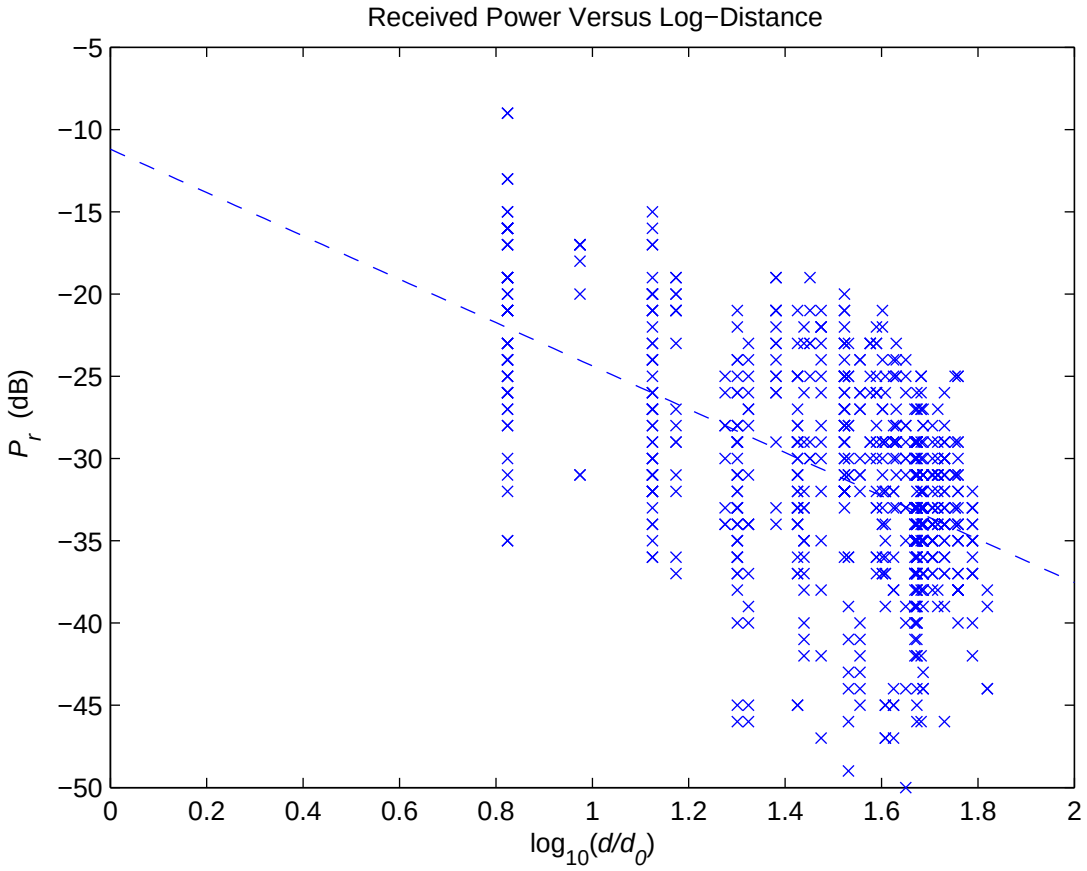

Figure 2.7: Received relative reference power in arbitrary dB units versus $\log_{10}(d/d_0)$. The blue x's represent measured power levels at the specified distance, and the dashed line is the computed best-fit line for the data. The path loss exponent and relative reference power can then be computed from the slope and y-intercept, respectively, of this line. The reason the reference level of the decibel units is not specified (i.e. dBm or dBW) is because the RSSI data from the TelosB nodes does not specify the exact reference level being used.

It should be noted that in this thesis power levels will be reported in dB (rather than dBW or dBm) because the exact reference level for the RSSI values reported by the TelosB sensor is not known (it is approximately -45 dBm to -50 dBm, but must be empirically determined [26]). Because the exact value is not known, we will simply refer to $P_{0,dB}$ as the "relative reference power", with units of dB. The image estimation accuracy is unchanged by the choice of reference level for the dB units because the only quantity affected is $P_{0,dB}$ given in (2.19).

Because the term $P_{0,dB}$ depends on the choice of reference distance, d_0, there are two parameters of interest that must be determined: the relative reference power, $P_{0,dB}$, and the path loss exponent, n_p, for a given choice of d_0 (which is arbitrary).

The astute observer will note that when the path loss equation is expressed in dB as is shown in (2.19), it may be plotted as a straight line where the abscissae (x-values) are given by $\log_{10}(d/d_0)$ and the ordinates (y-values) are simply the values of P_r for a given distance. The slope of the line is therefore $-10n_p$ and the y-intercept is $P_{0,dB}$. Thus, if one has a large number of RSS measurements as a function of distance, they plot them on a log-log plot and use linear least-squares regression to find the "best-fit" line for this data set and consequently, determine estimates for $P_{0,dB}$ and n_p from the y-intercept and slope of this line, respectively.

An example plot is shown in Figure 2.7. The data in this figure was taken during an RTI experiment wherein 28 TelosB sensor nodes were placed around the perimeter of a 140 ft by 140 ft square with even spacing (20 ft) between all nodes. The received power level from each node to each other node was recorded and plotted versus the base-10 logarithm of distance. Linear least-squares regression was used to find the best-fit line, which is also plotted in the figure. The relative reference power $P_{0,dB}$ is simply the y-intercept of the fit line (-11.1954 dB in this example), and the path loss exponent is computed by dividing the slope of the line by -10 (yielding a path loss exponent of 1.3174 in this example). The choice of dB units is arbitrary in this process because the only effect on the data would be to shift all the data points up or down by a constant amount, which would only affect the y-intercept of the line (the relative reference power).

This process is quite easy to perform in RTI because for each deployed network, there are already a large number of sensor pairs making RSS measurements essentially in real-time, so the process of path-loss exponent and relative reference power estimation is quite easy. Once these parameters are determined, one may estimate the values of the noise mean vector by:

$$E[n_i] \approx \hat{m}_i = \hat{P}_{r,dB}(d_i), \tag{2.20}$$

where d_i is the link distance for radio link i and

$$\hat{P}_{r,dB}(d) = \hat{P}_{0,dB} - 10\hat{n}_p \log_{10}\left(\frac{d}{d_0}\right), \tag{2.21}$$

where $\hat{P}_{0,dB}$ and $\hat{n}_p$ are the estimated relative reference power and path loss exponent, respectively.

2.2.5 Statistical Estimators for Attenuation Field Estimation

For a given noisy measurement vector, y, and a known weighting matrix, W, the objective is to estimate the image vector, x.

Linear reconstruction methods essentially use matrix inversion techniques to solve the linear estimation problem in (2.13). Algebraic Reconstruction Techniques (ART) from medical tomography are one way of solving the linear estimation problem wherein iterative techniques are used due to the potentially large size of the transfer matrix W [1]. In this work, however, we will implicitly assume that matrix inversion is available (and matrix sizes are small enough for direct solution methods) to the reader through software packages such as MATLAB.

If $n \sim \mathcal{N}(m, C_n)$, then it can be shown that the minimum variance unbiased (MVU) estimator to (2.13) is given by:

$$\hat{x} = \left(W^T C_n^{-1} W\right)^{-1} W^T C_n^{-1} (y - m), \tag{2.22}$$

provided that $\text{rank}(W) = N$, $M > N$, and C_n is positive definite [24]. If $M < N$, then the system is underdetermined and may not have a unique solution [1]. In other words, to use the MVU estimator directly, there must be more unique links than image pixels. For the case when the noise is white (i.e., $C_n = \sigma_n^2 I_M$), the relation in (2.22) reduces to:

$$\hat{x} = \left(W^T W\right)^{-1} W^T (y - m). \tag{2.23}$$

However, if W is not full-rank, then the matrix $W^T W$ will not be invertible because it will have some eigenvalues equal to zero. This makes the inversion problem very unstable because small amounts of noise may be amplified to the point that the resulting image estimate is meaningless. This characteristic makes RTI an ill-posed inverse problem [4].

It should be noted that the approach for image estimation in this section falls under classical estimation theory, wherein the parameters to be estimated (in this case, the image vector x) are assumed to be deterministic. If one assumes that the parameters to be estimated are random, a Bayesian approach would be used to estimate $E[x|y]$, the expected attenuation field given the set of measurements [24]. In this case, the correlated shadowing model described earlier can be utilized to specify the image statistics and construct an alternate linear estimator [5]. This approach, however, was not utilized in this work because it was not determined by the author to generate noticeably better image estimation quality. However, further investigation into utilizing Bayesian estimators may be beneficial to study at a future date.

2.2.6 Regularization Methods

To improve the conditioning of the matrix $W^T W$, a mathematical technique known as regularization may be used. A number of schemes have been proposed such as Tikhonov,

x_{13}	x_{14}	x_{15}	x_{16}
x_9	x_{10}	x_{11}	x_{12}
x_5	x_6	x_7	x_8
x_1	x_2	x_3	x_4

Figure 2.8: Pixel numbering scheme for a 4 by 4 pixel image. The convention used in this figure (i.e. numbering the pixels row-wise, left to right, starting with the lower left pixel) is the convention used throughout this work.

truncated singular value decomposition, and total variation [27], but we have only investigated Tikhonov regularization in this work. In Tikhonov regularization, an extra term is added in (2.23) to the matrix to be inverted. This is expressed mathematically as follows:

$$\hat{x}_T = \left(W^T W + \alpha \left(D_X^T D_X + D_Y^T D_Y\right)\right)^{-1} W^T \left(y - \hat{m}\right), \tag{2.24}$$

where the matrices D_X and D_Y are difference matrices for the image vector in the horizontal and vertical directions, respectively, and $\hat{m}$ is used in place of m because in practice, the path loss exponent and relative reference power are unknown and must be estimated. For example, if the elements of x are numbered according to the scheme shown in Figure 2.8, then the difference matrices will be given by:

$$D_X = \begin{bmatrix}
-1 & 1 & 0 & 0 & 0 & 0 & 0 & 0 & 0 & 0 & 0 & 0 & 0 & 0 & 0 & 0 \\
0 & -1 & 1 & 0 & 0 & 0 & 0 & 0 & 0 & 0 & 0 & 0 & 0 & 0 & 0 & 0 \\
0 & 0 & -1 & 1 & 0 & 0 & 0 & 0 & 0 & 0 & 0 & 0 & 0 & 0 & 0 & 0 \\
0 & 0 & 0 & 0 & -1 & 1 & 0 & 0 & 0 & 0 & 0 & 0 & 0 & 0 & 0 & 0 \\
0 & 0 & 0 & 0 & 0 & -1 & 1 & 0 & 0 & 0 & 0 & 0 & 0 & 0 & 0 & 0 \\
0 & 0 & 0 & 0 & 0 & 0 & -1 & 1 & 0 & 0 & 0 & 0 & 0 & 0 & 0 & 0 \\
0 & 0 & 0 & 0 & 0 & 0 & 0 & 0 & -1 & 1 & 0 & 0 & 0 & 0 & 0 & 0 \\
0 & 0 & 0 & 0 & 0 & 0 & 0 & 0 & 0 & -1 & 1 & 0 & 0 & 0 & 0 & 0 \\
0 & 0 & 0 & 0 & 0 & 0 & 0 & 0 & 0 & 0 & -1 & 1 & 0 & 0 & 0 & 0 \\
0 & 0 & 0 & 0 & 0 & 0 & 0 & 0 & 0 & 0 & 0 & 0 & -1 & 1 & 0 & 0 \\
0 & 0 & 0 & 0 & 0 & 0 & 0 & 0 & 0 & 0 & 0 & 0 & 0 & -1 & 1 & 0 \\
0 & 0 & 0 & 0 & 0 & 0 & 0 & 0 & 0 & 0 & 0 & 0 & 0 & 0 & -1 & 1
\end{bmatrix}, \tag{2.25}$$

and

$$D_Y = \begin{bmatrix} -1 & 0 & 0 & 0 & 1 & 0 & 0 & 0 & 0 & 0 & 0 & 0 & 0 & 0 & 0 & 0 \\ 0 & 0 & 0 & 0 & -1 & 0 & 0 & 0 & 1 & 0 & 0 & 0 & 0 & 0 & 0 & 0 \\ 0 & 0 & 0 & 0 & 0 & 0 & 0 & 0 & -1 & 0 & 0 & 0 & 1 & 0 & 0 & 0 \\ 0 & -1 & 0 & 0 & 0 & 1 & 0 & 0 & 0 & 0 & 0 & 0 & 0 & 0 & 0 & 0 \\ 0 & 0 & 0 & 0 & 0 & -1 & 0 & 0 & 0 & 1 & 0 & 0 & 0 & 0 & 0 & 0 \\ 0 & 0 & 0 & 0 & 0 & 0 & 0 & 0 & 0 & -1 & 0 & 0 & 0 & 1 & 0 & 0 \\ 0 & 0 & -1 & 0 & 0 & 0 & 1 & 0 & 0 & 0 & 0 & 0 & 0 & 0 & 0 & 0 \\ 0 & 0 & 0 & 0 & 0 & 0 & -1 & 0 & 0 & 0 & 1 & 0 & 0 & 0 & 0 & 0 \\ 0 & 0 & 0 & 0 & 0 & 0 & 0 & 0 & 0 & 0 & -1 & 0 & 0 & 0 & 1 & 0 \\ 0 & 0 & 0 & -1 & 0 & 0 & 0 & 1 & 0 & 0 & 0 & 0 & 0 & 0 & 0 & 0 \\ 0 & 0 & 0 & 0 & 0 & 0 & 0 & -1 & 0 & 0 & 0 & 1 & 0 & 0 & 0 & 0 \\ 0 & 0 & 0 & 0 & 0 & 0 & 0 & 0 & 0 & 0 & 0 & -1 & 0 & 0 & 0 & 1 \end{bmatrix}. \quad (2.26)$$

The relation in (2.24) can be simplified as follows:

$$\hat{x}_T = \Pi z, \quad (2.27)$$

where

$$\Pi = \left(W^T W + \alpha \left(D_X^T D_X + D_Y^T D_Y\right)\right)^{-1} W^T,$$

and

$$z = y - \hat{m}.$$

Thus, the estimation algorithm can be expressed as a linear transformation of the shifted input data. It should be noted that the matrix Π needs only to be computed once and can be used repeatedly for future image updates.

2.2.7 Estimation Error Analysis

To understand potential sources of error in the estimated image, we will rewrite (2.27) in the following form:

$$\begin{aligned} \hat{x}_T &= \Pi z \\ &= \Pi(y - \hat{m}) \\ &= \Pi(Wx + n - \hat{m}) \\ &= Qx + u \\ &= \tilde{x} + u, \end{aligned} \quad (2.28)$$

where $\tilde{x} = Qx$, $u = \Pi(n - \hat{m})$, and

$$\begin{aligned} Q &= \Pi W \\ &= (W^T W + \alpha(D_X^T D_X + D_Y^T D_Y))^{-1} W^T W. \end{aligned} \quad (2.29)$$

The statistics of the noise vector $u \in \mathbb{R}^N$ are computed as follows:

$$\begin{aligned} E[u] &= \Pi E[n - \hat{m}] \\ &= \Pi(E[n] - E[\hat{m}]) \\ &= \Pi(m - E[\hat{m}]) \\ &= 0, \end{aligned} \tag{2.30}$$

where we have assumed $E[\hat{m}] = m$ for simplicity of analysis, and

$$\begin{aligned} \mathrm{Cov}[u] &= E[uu^T] \\ &= \Pi C_n \Pi^T \\ &= \sigma_n^2(\Pi I_M \Pi^T), \end{aligned} \tag{2.31}$$

where C_n is the covariance matrix of the noise vector n [25].

It can be seen from (2.28) that the image estimate consists of a filtered version of x with filtered (colored) noise added to each pixel. The filtering process is represented by the matrix multiplication Qx; note that if $\alpha = 0$, W is full rank, and if there are more link measurements than pixels, Q becomes the identity matrix, and no information is lost in the filtering process. However, if W is not full rank (due to the radio links not sufficiently covering each pixel) or if there are fewer link measurements than pixels (both of which are generally the case), alpha must be set to a nonzero value for the matrix inverse in (2.29) to exist.

To visualize the effect regularization has on image quality, a test image was generated wherein a single pixel, whose centroid is located at (10.25 ft,10.25 ft), was set to have an attenuation value of 1 dB, and all other pixels were set to an attenuation value of 0 dB. The pixels in this image have pixel width of 0.5 ft. The regularization parameter $\alpha = 2.111$ in this experiment, and $\lambda = 0.0999$ ft was used to construct the W matrix. The "sensors" are placed around the perimeter of a 21 ft by 21 ft area, with sensors spaced every 3 ft (28 sensors total). The test image is shown in Figure 2.9.

The output of the filter is shown in Figure 2.10. It can be seen that the energy present in the attenuating pixel has been spread across neighboring pixels. Note that the most attenuating pixel (which is located at (10.25 ft, 10.25 ft)) now has an attenuation value of less than 0.1 dB. It should be noted, however, that when simulating the RSS for a link passing through the point (10.25 ft, 10.25 ft), the pixel at (10.25 ft, 10.25 ft), as well as several of its neighboring pixels, will be included in the total shadowing observed in that link, which will have the effect of somewhat offsetting the error due to filtering the image. It should be reiterated that information is lost due to the fact that either W is not full rank, or that the number of pixels to be estimated is greater than the number of link measurements, and thus regularization is necessary.

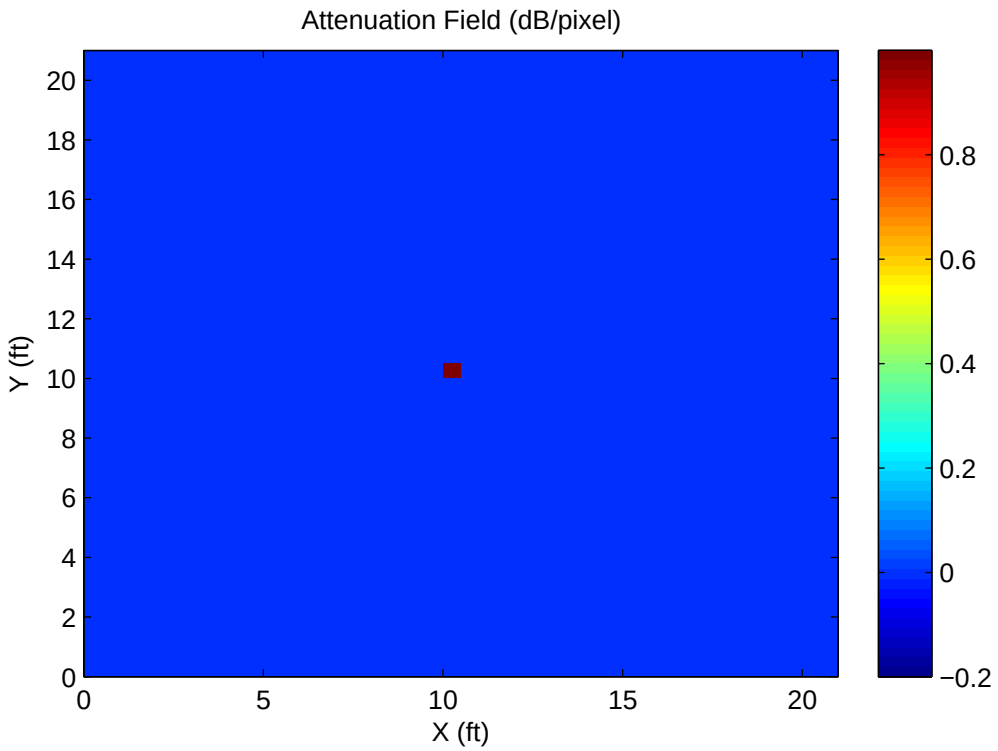

Figure 2.9: Test point source image, wherein a single pixel's attenuation value was set to 1 dB, with the other pixels set to 0 dB. The pixel width is 0.5 ft, and the 1 dB pixel's centroid is located at (10.25 ft, 10.25 ft).

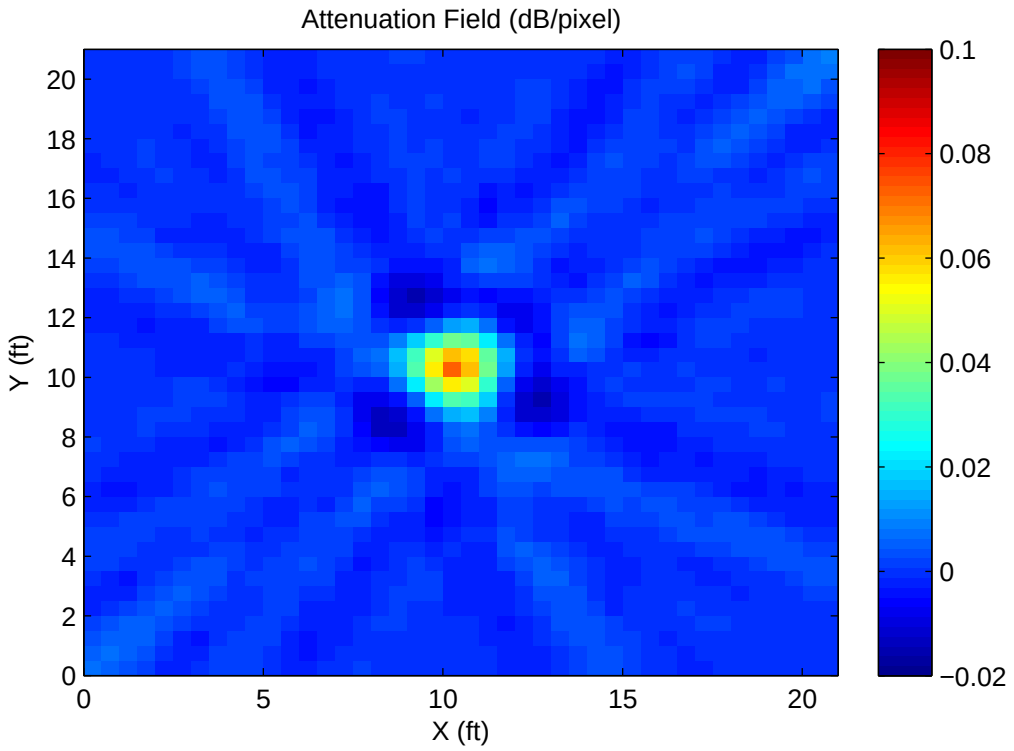

Figure 2.10: Output of the regularization operation given in (2.29) with $\alpha = 2.111$ and $\lambda = 0.0999$ ft used to construct the necessary matrices. Note that the image limits have been scaled by a factor of 0.1 to make the output more visible.

Bias and Variance

To study the effect the noise has on the quality of the image estimate, we will derive the bias and variance of the linear estimator given in (2.28). The bias of the estimator is given by [25]:

$$\begin{aligned} B[\hat{x}_T] &= E[\hat{x}_T] - x \\ &= E[Qx + u] - x \\ &= Qx + E[u] - x \\ &= Qx + \Pi E[n - \hat{m}] - x \\ &= Qx + \Pi(m - E[\hat{m}]) - x \\ &= \tilde{x} - x. \end{aligned} \tag{2.32}$$

For simplicity of analysis have assumed that $E[\hat{m}] = m$. It can be seen from (2.32) that any bias in the estimator is caused by loss of information due to filtering, as was discussed earlier. The covariance matrix of the estimator is given by [25]:

$$\begin{aligned} \text{Cov}[\hat{x}_T] &= E[(\hat{x}_T - E[\hat{x}_T])(\hat{x}_T - E[\hat{x}_T])^T] \\ &= E[(\hat{x}_T - Qx)(\hat{x}_T - Qx)^T] \\ &= E[uu^T] \\ &= \sigma_n^2(\Pi I_M \Pi^T). \end{aligned} \tag{2.33}$$

The variance of the estimator at each pixel is contained in the elements of the the main diagonal of $\text{Cov}[\hat{x}_T]$, and the standard deviation is simply the square root of the variance. Because the standard deviation is proportional to σ_n, the standard deviation was normalized by σ_n for plotting, and the result is shown in Figure 2.11. It can be observed that the center part of the figure generally has the lowest variance, likely due to the fact that the center of the figure has the most dense link coverage.

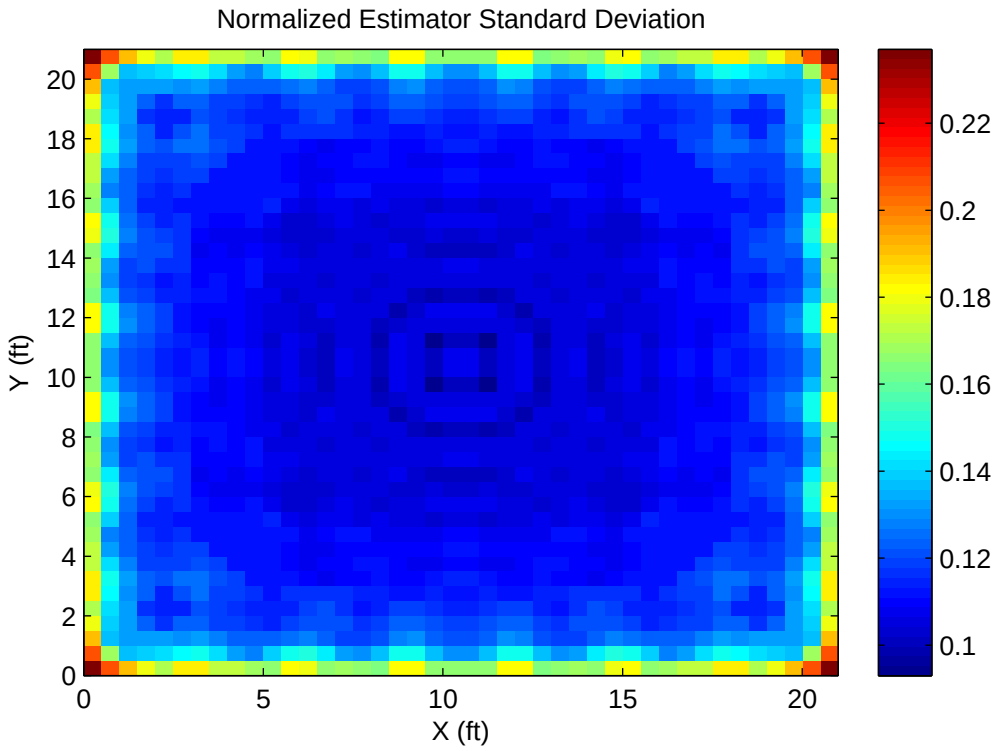

Figure 2.11: Normalized standard deviation of each pixel of $\hat{x}_T$, normalized by the noise standard deviation. It can be seen that the standard deviation is lowest near the center of the figure, where the density of link measurements is highest.

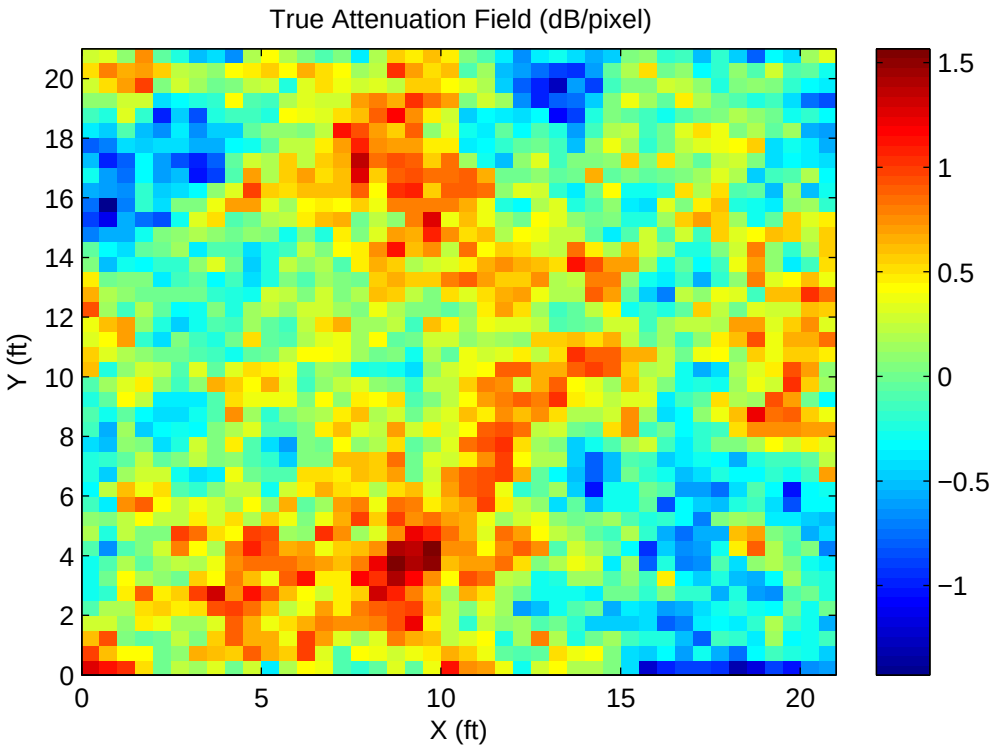

Figure 2.12: Random test image used to illustrate the regularization process. This image was generated using the correlated shadowing model given in (2.1)-(2.7) with $\sigma_X = 1$ dB, $\delta = 2$ ft, $\sigma_n = 1$ dB.

SNR Considerations

To illustrate the image estimation process on a more realistic image, a random scene was generated using the correlated shadowing model given in (2.1)-(2.7) with $\sigma_X = 1$ dB, $\delta = 2$ ft, $\sigma_n = 1$ dB, and path loss parameters $P_{0,dB} = -45$ dB, $n_p = 3$, and $d_0 = 3$ ft. Noisy RSS measurements were generated using (2.13) (where the noise was applied to both the forward and reverse links, and then the RSS from each direction was averaged so that there were M unique links, so the problem conforms with the form given in (2.13)). The noisy link measurements were then used to estimate the image using (2.24). For this experiment $\alpha = 2.111$ and $\lambda = 0.0999$ ft. The sensors are placed around the perimeter of a 21 ft by 21 ft area, with sensors spaced every 3 ft (28 sensors total). The true and estimated images are shown in Figures 2.12-2.13, respectively, and the estimation error is shown in Figure 2.14. It can be noted that by observing the estimation error that the magnitude of the error is comparable to the magnitude of the image itself.

To calculate the SNR for each pixel for this test image, it is necessary to calculate the

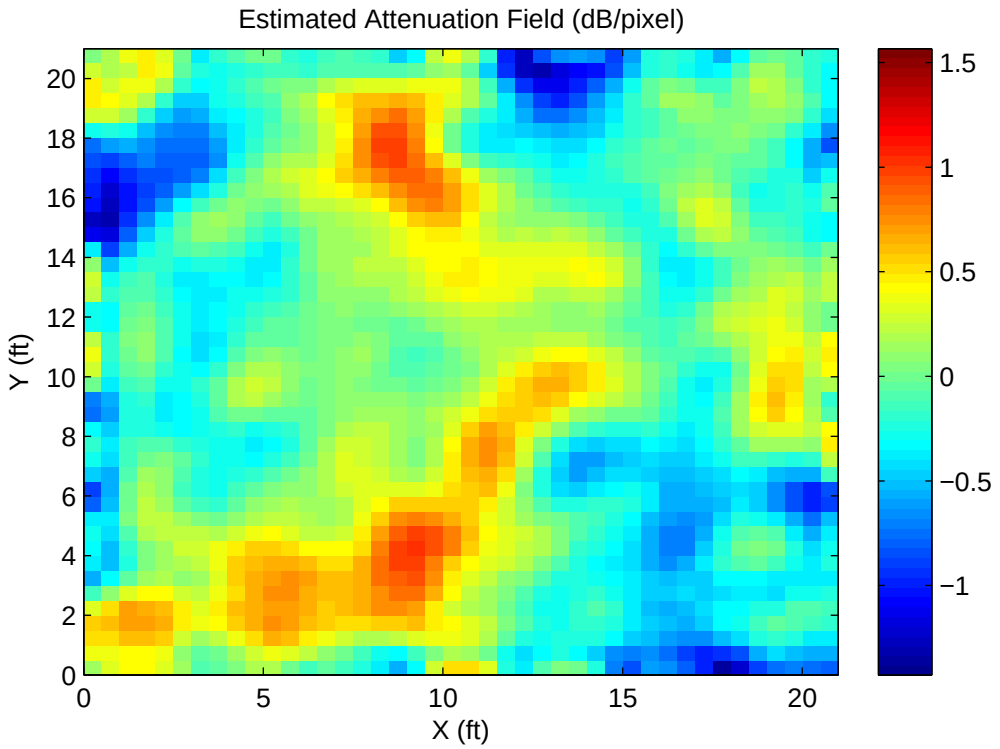

Figure 2.13: Estimated image using $\alpha = 2.111$, $\lambda = 0.0999$ ft and sensors placed around the perimeter spaced every 3 ft (28 sensors total).

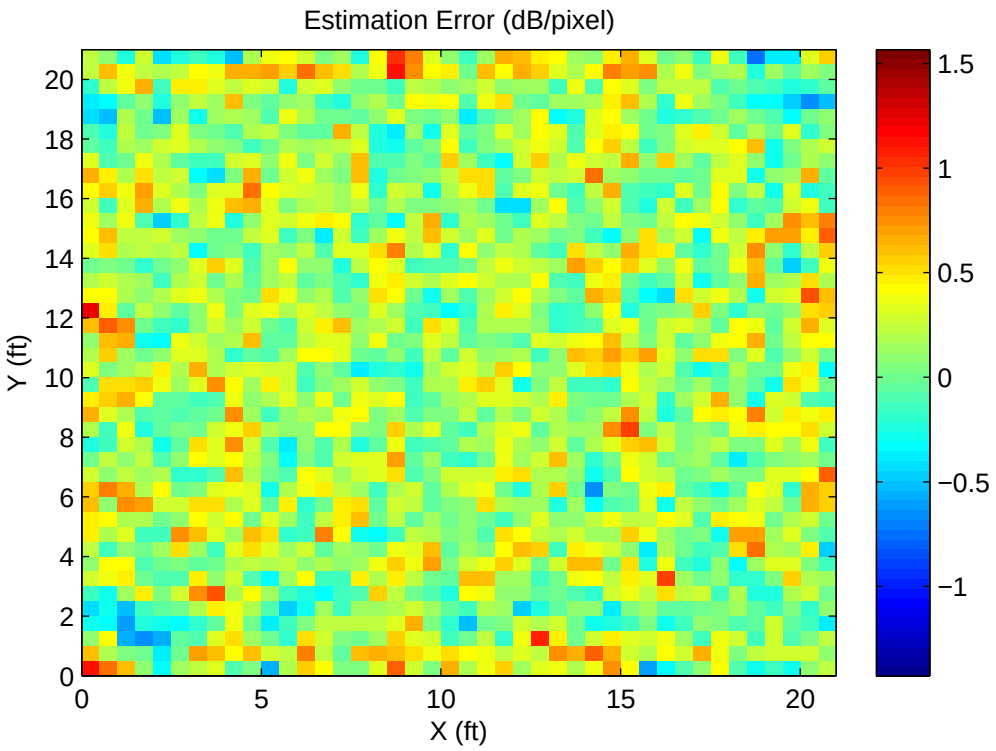

Figure 2.14: Estimation error of the test image. Note that for many pixels, the magnitude of the error is comparable to the magnitude of the image itself.

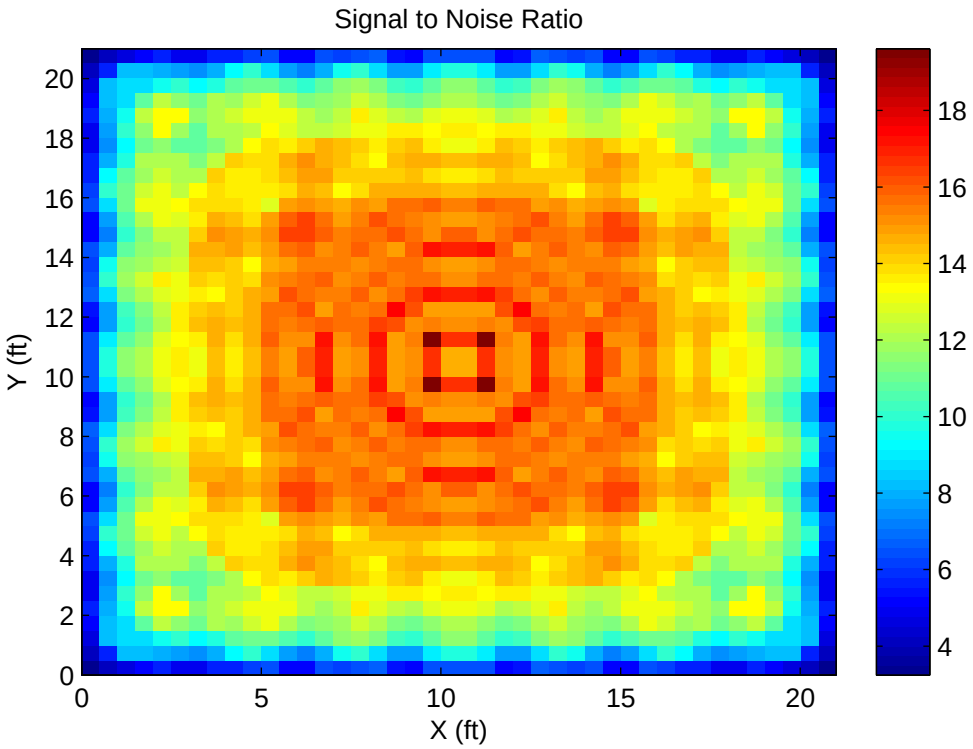

Figure 2.15: Signal to noise ratio of the image per pixel (unitless). Note that despite the relatively high SNR's observed for many pixels, there is still significant estimation error.

covariance matrix of the estimated image. This is obtained by noting that $\tilde{x} = Qx$; therefore:

$$C_{\tilde{x}} = QC_xQ^T, \tag{2.34}$$

where $C_{\tilde{x}}$ and C_x are the covariance matrices of $\tilde{x}$ and x, respectively [25]. The covariance matrix of x is given by (2.1). The SNR for pixel j, γ_j, is given by:

$$\gamma_j = \frac{[C_{\tilde{x}}]_{jj}}{[C_u]_{jj}} \tag{2.35}$$

where $j \in 1, \ldots, N$, and $[\,\cdot\,]_{jj}$ denotes the j^{th} diagonal element of the square matrix enclosed. The SNR per pixel was calculated, and the result is plotted in Figure 2.15.

It can be seen from Figure 2.15 that the SNR is relatively high (over 10) for most of the pixels. This is surprising given the previous observation that the estimation error was on order of the quantity being estimated. This observation leads one to concede that SNR alone is not a sufficient metric to gauge image estimation performance, but the effect of regularization should be considered as well. The poor estimated image quality can be improved by

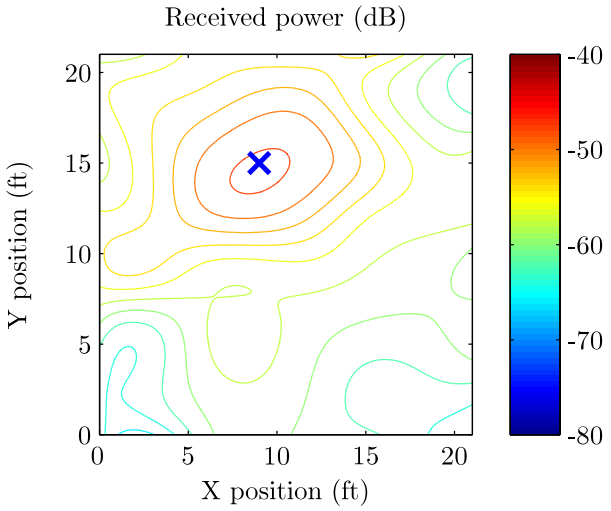

Figure 2.16: Example modeled received signal strength contour map. The blue "x" represents the hypothetical transmitter location, and the received power contours were generated using the exponential path loss model in (2.19) and shadowing model given in (2.10). Cubic spline interpolation was used to generate a higher resolution image for plotting purposes.

increasing the number of deployed sensors (and consequently the number of links) so that rank deficiency and the under-constrained nature of the problem can be mitigated.

2.3 RSS Coverage Prediction

As has been previously mentioned, a primary purpose of this thesis is to study the application of radio tomographic imaging to the problem of attenuation field estimation. When attenuation field data, such as is shown in Figures 2.3-2.3, has been obtained, one may place a hypothetical "transmitter" anywhere in the attenuation field and predict the received signal strength at any other point in the field using the following relation:

$$y_{sim} = W\hat{x}_T + \hat{m}, \tag{2.36}$$

where W and $\hat{m}$ are chosen such that a test node is placed at every point in space where an RSS estimate is desired, as well as a test node being placed at the location of the hypothetical transmitter.

This approach gives more detailed information than simple statistical models, but is simpler than more advanced techniques such as ray tracing [14]. Thus, this method takes somewhat of a "middle-of-the-road" approach between the statistical and deterministic methods.

An example simulation output is shown in Figure 2.16. The position of the hypothetical transmitter is marked with the blue "x", and the colored lines are contours of constant RSS

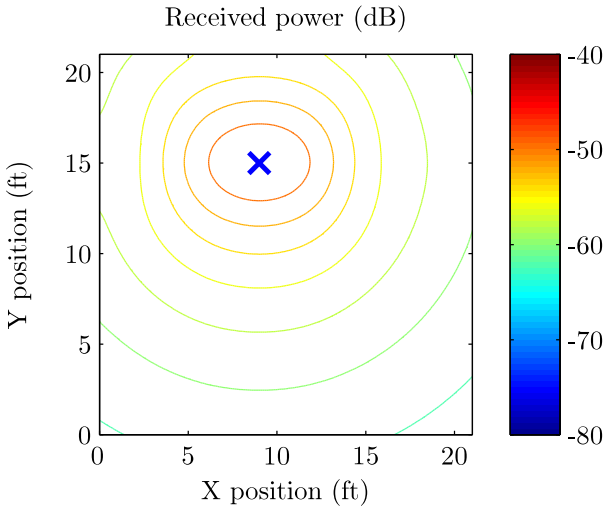

Figure 2.17: Example modeled received signal strength contour map. The blue "x" represents the hypothetical transmitter location, and the received power contours were generated using the exponential path loss model in (2.19). Cubic spline interpolation was used to generate a higher resolution image for plotting purposes. (This is why the contours look slightly elliptical.)

values. It can be seen from this figure that the additional data provided by RTI drastically changes the predicted mean signal strength from that which would be predicted using the standard exponential path loss model given in (1.7). Visually, when one uses the exponential path loss model, the RSS contours are circles, as is shown in Figure 2.17.

The advantage of this approach is that it allows for prediction of signal strength over a large area for any number of possible transmitter sites by just taking a few measurements around the perimeter of the area without having to know any geographic information about the area of interest and without having to do any kind of extensive drive-testing measurement campaign. As well, the computational simplicity of this method, and the fact that most devices already measure RSS values allow for easy implementation in future systems.

2.4 Position Location

While a number of authors have investigated the problem of using RTI for passive object tracking [20–22], serious investigation of applying the additional propagation data provided by RTI to the problem of RSS-based position location algorithms has not been undertaken.

2.4.1 Position Location with RTI

While the problem of RSS-based position location without using RTI data leads to a simple geometric interpretation (i.e., finding the intersection of three circles in the noiseless case), as was shown in Figure 1.3, when RTI data is included, the geometry becomes more complicated. As it was shown in Figure 2.16, the constant-RSS contours are no longer circles, and so the point of interest would lie at the intersection of three such contours (if there is no noise).

2.4.2 Error Minimization Problem

However, because of the presence of noise in all real scenarios, the problem of finding the free transmitter location becomes a minimization problem. Specifically, the problem may be formulated as a least-squares problem as follows:

$$\hat{\theta} = \arg\min_{\theta} \parallel y - y_{sim}(\theta) \parallel^2 = \arg\min_{\theta} G(\theta), \tag{2.37}$$

where $\theta, \hat{\theta} \in \mathbb{R}^2$ are position coordinate vectors, $y \in \mathbb{R}^M$ is the vector of measured RSS values from each of the anchor nodes, $G(\theta) = \parallel y - y_{sim}(\theta) \parallel^2$ is the objective function to be minimized, and $y_{sim}(\theta) \in \mathbb{R}^M$ is the vector of modeled RSS values from the RTI data using (2.36) to model the RSS values experienced by each of the anchor nodes for each possible free node location, θ. This leads to the creation of a three dimensional error surface for which the global minimum point corresponds to the least-squares estimate of the position. An example error surface is shown in Figure 2.18.

In general, the problem posed in (2.37) is nonlinear; therefore some type of iterative search algorithm is generally used to solve for the free node location. Among these are the methods of steepest descent, Gauss-Newton, Levenberg-Marquardt, and the trust region method [3]. However, due to the unique method for computing the RSS values for each choice of test transmitter location, θ in RTI-RSS position location, a new method was devised, which will be referred to hereafter as the Radial Search Algorithm.

2.4.3 Radial Search Algorithm

The development of the Radial Search Algorithm was motivated by the fact that to estimate what the received signal strength would be at a point (or multiple points), one has to recompute the weighting matrix, W, from (2.15) and (2.16) to include the points of interest. In essence, we are effectively placing "fake" receivers at each of the test points in our simulation and probing the power received at those points.

As well, the desire to devise an original minimization algorithm comes from the fact that there is no analytical expression for the error function (so it would be difficult to take derivatives

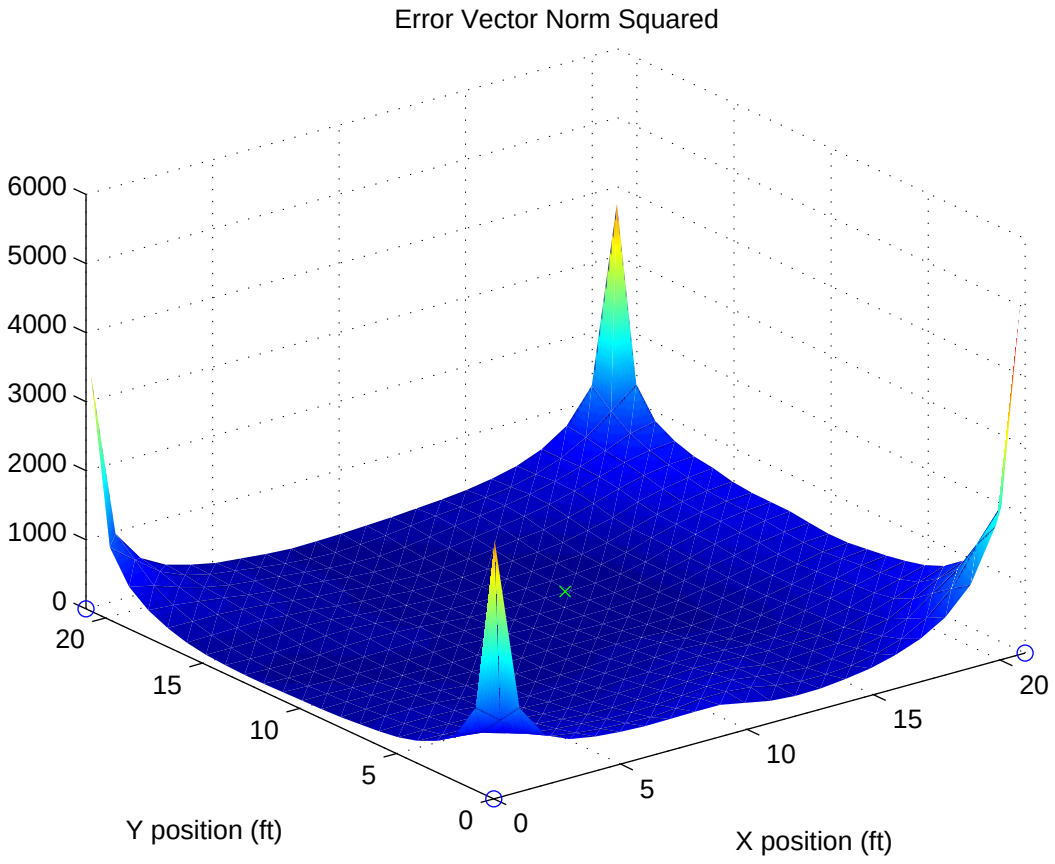

Figure 2.18: Example error surface generated from the problem stated in (2.37). The light blue "x" represents the true transmitter location, and the four blue circles (one at each corner of a 21 ft by 21 ft square area) represent anchor node locations.

to implement a method such as steepest descent) [28], and the fact that the W matrix allows one to probe several test points at once.

A computational limitation arises from the fact that the weighting matrix, W, contains $(K^2 - K)N/2$ elements, where K is the number of test points, and N is the number of pixels in the scene. For example, if the scene is 21 ft by 21 ft, the pixel width is 0.5 ft (i.e. $N = 42^2$), and one wants to probe the received power every foot (i.e. $K = 22^2$), then there will be 206,186,904 elements in W. If each element is stored as a double precision floating point number (8 bytes each), it would take approximately 1.5362 gigabytes to store the matrix alone. If one desired to increase the area to 24 ft by 24 ft, with the same pixel size, it would require approximately 3.3474 gigabytes to store. Thus, we can see that the memory requirements for storing W are significant.

In addition to the memory constraints imposed by such large matrices, there is a significant computational burden in creating the W matrix, as well as any matrix operations that are performed with it. Even when W is stored as a sparse matrix, wherein only the indices and values for the nonzero elements are stored, the computational and memory burdens are high.

Thus, an iterative scheme was developed wherein an initial, lower precision, sweep over the entire test field is first performed, then the algorithm "zooms in" on areas of interest until it finds what it considers to be the global minima of the error-squared function. The algorithm is described fully below:

Algorithm 1 Radial Search Algorithm

1. Evaluate $G(\theta_1) \; \forall \; \theta_1 \in \Omega_1$, where Ω_1 is a rectangular sampling of points separated by distance δ_x in the x-direction and δ_y in the y-direction over the entire search area

2. $\hat{\theta}_1 = \arg\min_{\theta_1} G(\theta_1)$

3. $\delta_1 = \max(\delta_x, \delta_y)$

4. $i \leftarrow 2$

5. While $\delta_i \; > \delta_{min}$

    1. Evaluate $G(\theta_i) \; \forall \; \theta_i \in \Omega_i$, where Ω_i is a rectangular sampling of points separated by distance δ_i within radius $\sqrt{2}\delta_{i-1}$ of $\hat{\theta}_{i-1}$ (to include the entire region between the points in Ω_{i-1} adjacent to $\hat{\theta}_{i-1}$)

    2. $\hat{\theta}_i = \arg\min_{\theta_i} G(\theta_i)$

    3. $i \leftarrow i + 1$

6. Evaluate $G(\theta_N) \; \forall \; \theta_N \in \Omega_N$, where Ω_N is a rectangular sampling of points separated by distance δ_N within radius $\sqrt{2}\delta_{N-1}$ of $\hat{\theta}_{N-1}$ (at this point $i = N$)

7. $\hat{\theta}_N = \arg\min_{\theta_N} G(\theta_N)$

8. $\hat{\theta} = \hat{\theta}_N$

A visualization of this algorithm is shown in Figure 2.19.

The advantage of this approach is that it is conceptually simple and by breaking the computation of the W matrix into smaller sizes, it makes the search problem computationally feasible. Also, because the algorithm does an initial search over the entire domain of interest, it is relatively robust against converging to a local minimum instead of the global minimum. More details about the specific parameters (e.g. starting search point spacing, circle radii, search points per circle, etc.) will be detailed in the following chapter which deals with computer simulation results.

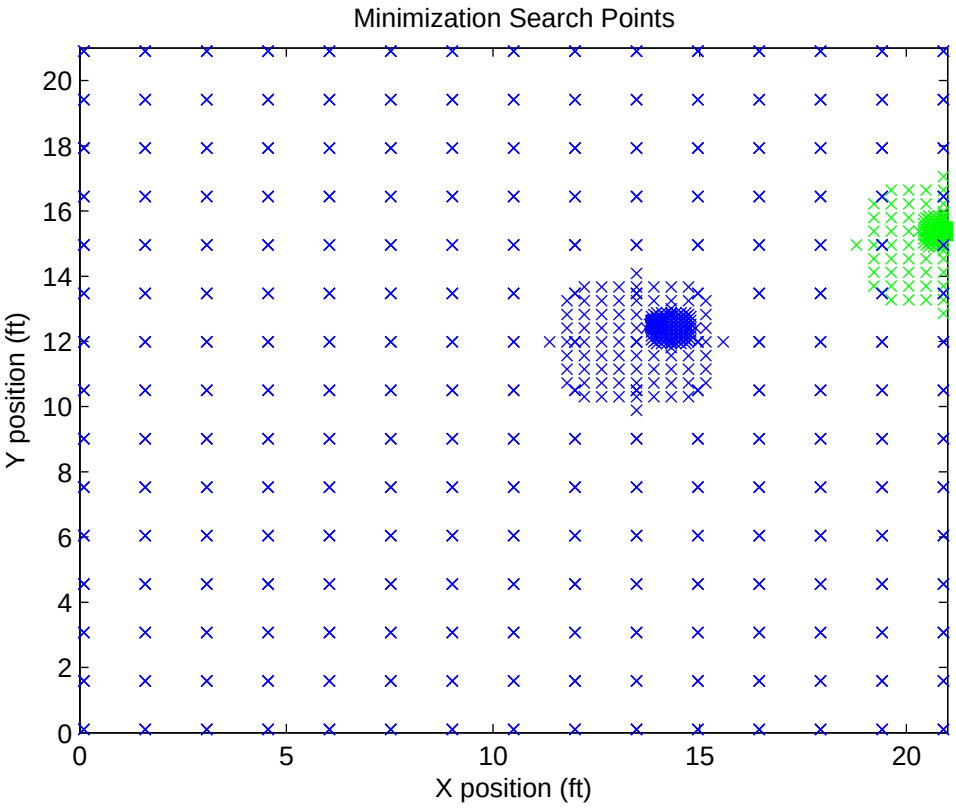

Figure 2.19: Visualization of search algorithm. A coarse sampling of the entire objective function is taken, then the algorithm recursively searches at points within a specified radius centered at the last iteration's minimum value. The blue x's represent the points searched when tomography data is included in the RSS model whereas the green x's represent the points searched when tomography data is not accounted for. (The initial coarse sampling over the entire area is the same in both cases.)

2.5 Conclusion

The mathematical foundations of algebraic RTI have been described, as well as the methods used to estimate channel parameters such as the path-loss exponent, relative reference power, and attenuation field values. Applications of this method to the problem of RSS-based position location have been described, and the effectiveness of this approach will be further described in the following chapters.

Chapter 3

Computer Simulations and Proof of Concept

3.1 Introduction

The purpose of this chapter will be to demonstrate the implementations of the algorithms mentioned in the previous chapter, evaluate their performance, and show proof of concept of the claims made. The process of generating a test scene using the correlated shadowing model will be explained, optimal regularization parameters will be obtained for the given image constraints, regularized image estimates will be produced from noisy data, and a performance evaluation of the RTI-RSS position location algorithm will be performed. It will be shown in this chapter that the estimator developed in Chapter 2 is effective at recovering the attenuation field image from noisy data, and that by implementing the additional information provided by attenuation field estimate, RSS-position location estimates can be significantly improved.

3.2 Image Simulation

As was described in the previous chapter, the correlated shadowing model may be used to generate random scenes to evaluate the performance of RTI algorithms. A set of four random images were generated using equation (2.1) to generate a covariance matrix which was used with the MATLAB function `mvnrnd` with the following parameters:

- $\sigma_X = 1$ dB
- $\delta = 2$ ft

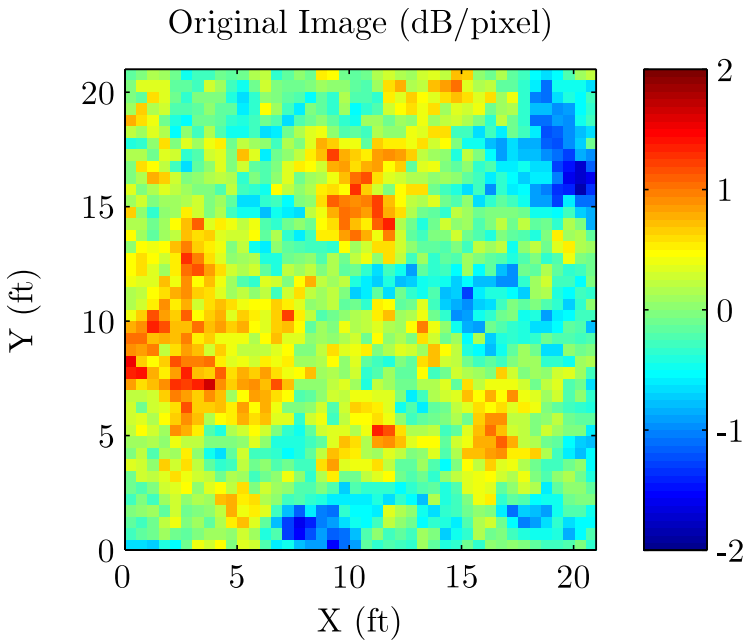

Figure 3.1: Random test image number 1.

- Image dimensions = 21 ft by 21 ft
- Pixel width = 0.5 ft

Each image generated was a different instantiation of a 1764 element zero-mean Gaussian random vector with covariance matrix given by (2.1). The resulting images are shown in Figures 3.1-3.4. This set of four test images will be referred to in future sections of this chapter.

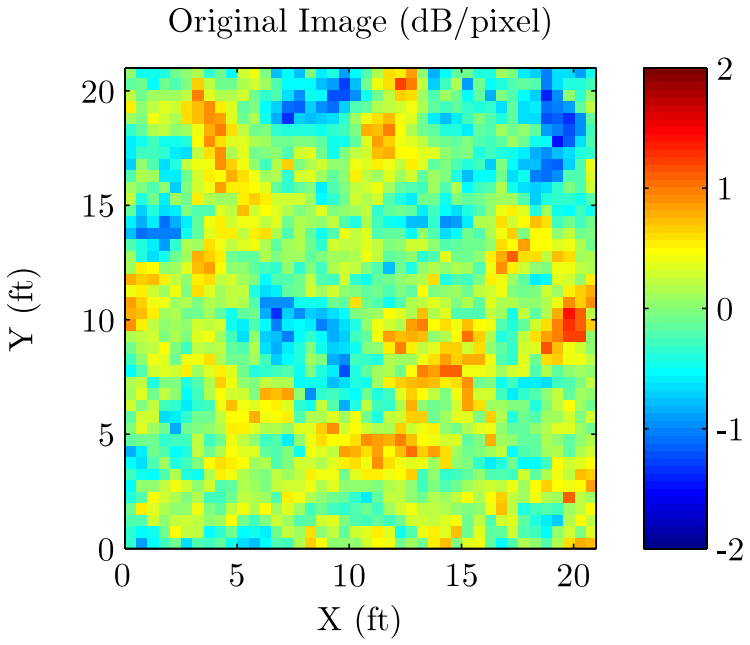

Figure 3.2: Random test image number 2.

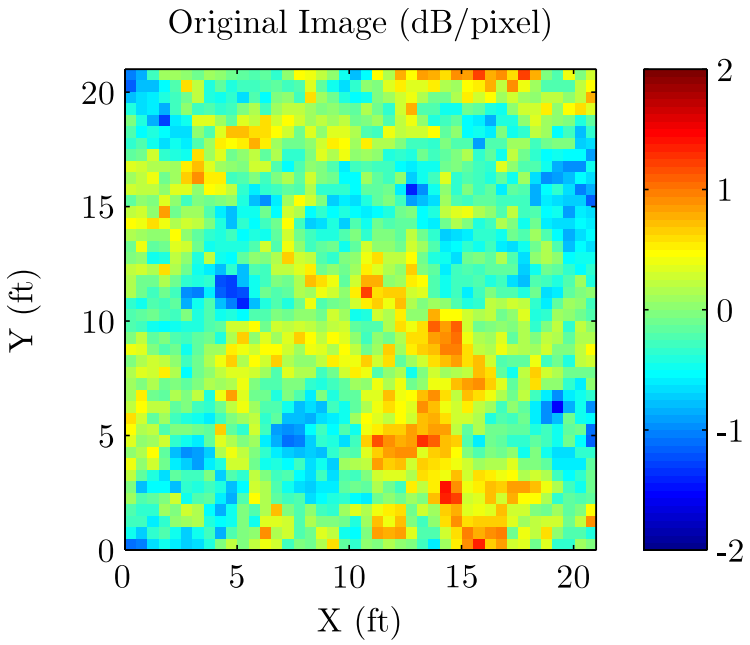

Figure 3.3: Random test image number 3.

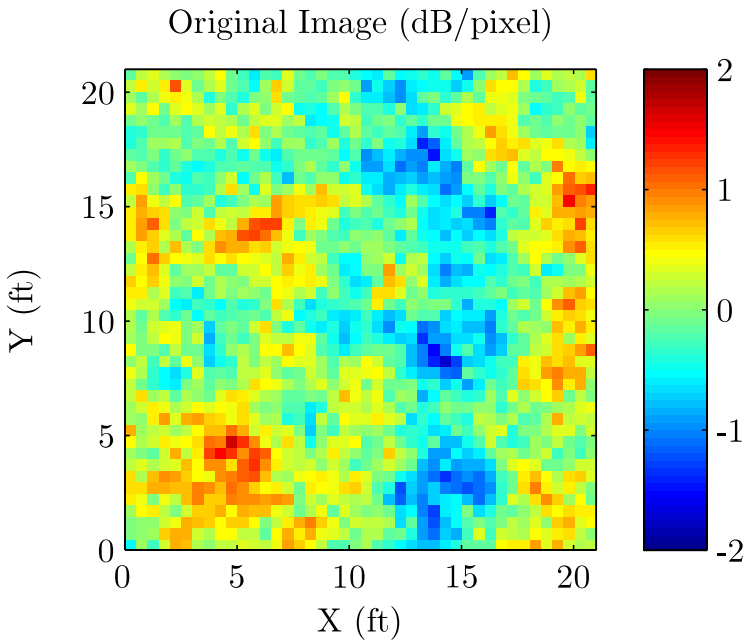

Figure 3.4: Random test image number 4.

3.2.1 Image Reconstruction

It is desired now to show how the image reconstruction process works and evaluate its performance so that one may know, at least qualitatively, the quality of image reconstruction that can be expected when the algorithm is implemented in a physical system.

The process of simulating the performance of the image reconstruction algorithm involves generating a random image, specifying hypothetical sensor node locations, generating noisy measurements from scene data, then producing a regularized image estimate from the noisy data. This process is described in full detail below:

Algorithm 2 Image Reconstruction Simulation Algorithm

1. Specify image dimensions, pixel width, and pixel selection parameter λ from (2.16).
2. Generate a random shadowing environment using a zero-mean Gaussian random vector with covariance matrix specified by (2.1).
3. Specify a path-loss exponent n_p, relative reference power level $P_{0,dB}$, and reference distance d_0 from the exponential path loss model given in (2.19).
4. Specify hypothetical sensor node locations.
5. Compute the matrix W, which specifies the relationship between each link and the pixels (elements of the image vector x) that affect that link.
6. Compute the path loss and shadowing for each link using (2.19) and (2.10), respectively.
7. Compute the expected value for the noise signal in (2.13) using (2.18).
8. Specify a noise standard deviation, σ_n for the noise signal. All links are assumed to have independent noise.
9. Generate Gaussian noise for each link from the given mean and standard deviation.
10. Model the RSS from each radio link using the computed path loss, shadowing, and noise.
11. Average the received power level for both the forward and the reverse path on each link so that there is only one RSS value per unique link.
12. The resulting M RSS values are arranged into the vector y from (2.13), where M is the number of unique links given by (2.8).
13. The regularized estimator given in (2.24) is used to produce the image estimate.

For all simulations performed in this chapter, values of $n_p = 3$, $P_{0,dB} = -45$ dB, and $d_0 = 3$ ft were used, and the sensor nodes are placed around the perimeter of a 21 ft by 21 ft area, spaced evenly every 3 ft (for a total of 28 nodes), unless otherwise specified.

3.2.2 Optimal Regularization Parameters

During the image reconstruction process, there are two parameters of interest that affect the quality of the image estimates- the ellipse width parameter λ in (2.16) and the regularization constant α in (2.24). The choice of both of these parameters is critical for the following reasons:

- λ controls the ellipse width, as is seen in Figure 2.5. If λ is too small, too many relevant pixels will be excluded from each link, whereas if λ is too large, too many pixels will be included in each link, which leads to a physically unrealistic model.
- α controls the extent to which the matrix $W^T W$ in (2.24) is regularized for invertibility. If α is too low, the matrix $W^T W$ be poorly conditioned (highly sensitive to noise or

rounding error), whereas if α is set too high, the original information contained in the matrix $W^T W$ will be lost.

- Heuristically, varying α has the effect of "blurring" the image, i.e., spreading the energy in each pixel over neighboring pixels to reduce the effect of noise. The higher the value of α, the more "blurring" occurs. If α is set too low, the image is too noisy; if α is set too high, the image is so blurry that the essential features are lost.

To determine optimal values for α and lambda for the geometries given by the images in Figures 3.1-3.4, an iterative search was performed. For each image, differing values of λ and α were used to reconstruct each image using the procedure given in Algorithm 2, and the mean squared error ($\texttt{mean}[(x - \hat{x}_i)^2]$, $i = 1, \ldots, 4$) of the estimated image as compared to the true image was computed and plotted for each value of λ and α. For each image, the values of λ were varied using 60 logarithmically spaced points from 10^{-3} to 10^{0}, and the values of α were varied using 60 logarithmically spaced points from 10^{-1} to 10^{2}. The resulting error surfaces for test images 1-4 are shown in Figures 3.5-3.8, respectively. The values of λ and α that yielded the least mean-squared error (MSE) for each image were chosen. The "optimal" values for this image geometry where then chosen by averaging the "optimal" values for λ and α obtained from each image.

From this numerical experiment, it was determined that $\lambda_{opt} = 0.0999$ and $\alpha_{opt} = 2.1110$. For illustrative purposes, if one considers a link that is 21 ft long, and $\lambda = \lambda_{opt}$ is used to construct the ellipse described by (2.16), the ellipse will be 21.0999 ft long along the major axis, and the width (minor axis length) of the ellipse will be 2.054 ft at its widest point.

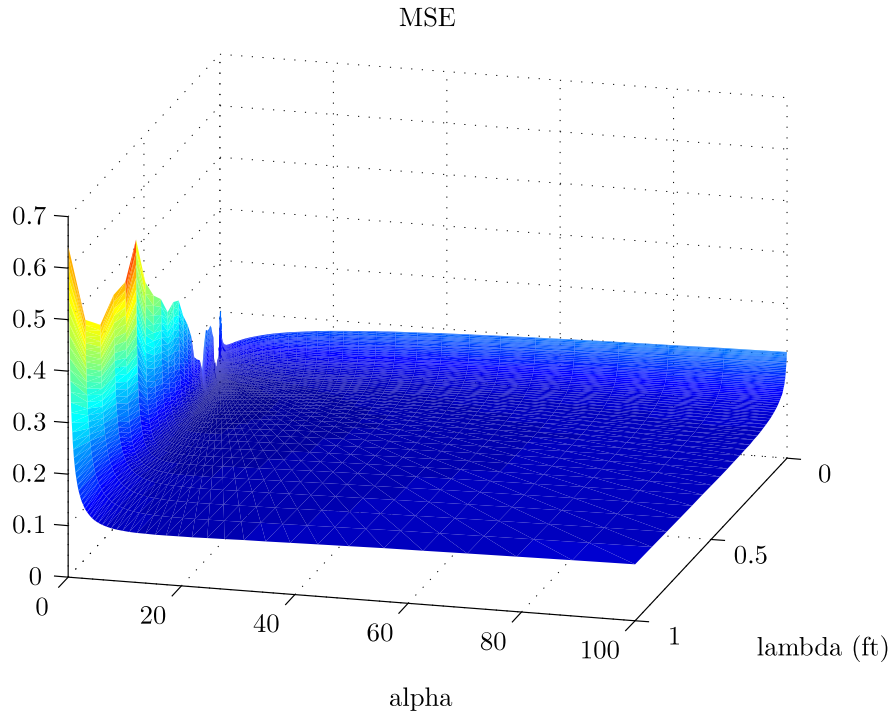

Figure 3.5: Error surface for test image 1 where λ is varied logarithmically from 10^{-3} to 10^{0} and α is varied logarithmically from 10^{-1} to 10^{2}. Note that beyond certain values of λ and α, the surface remains relatively flat, implying that the choice of α and λ have little effect on the MSE after they are raised above those critical values. It is important to note, however, that lower values of α are desirable for the reasons mentioned in the text.

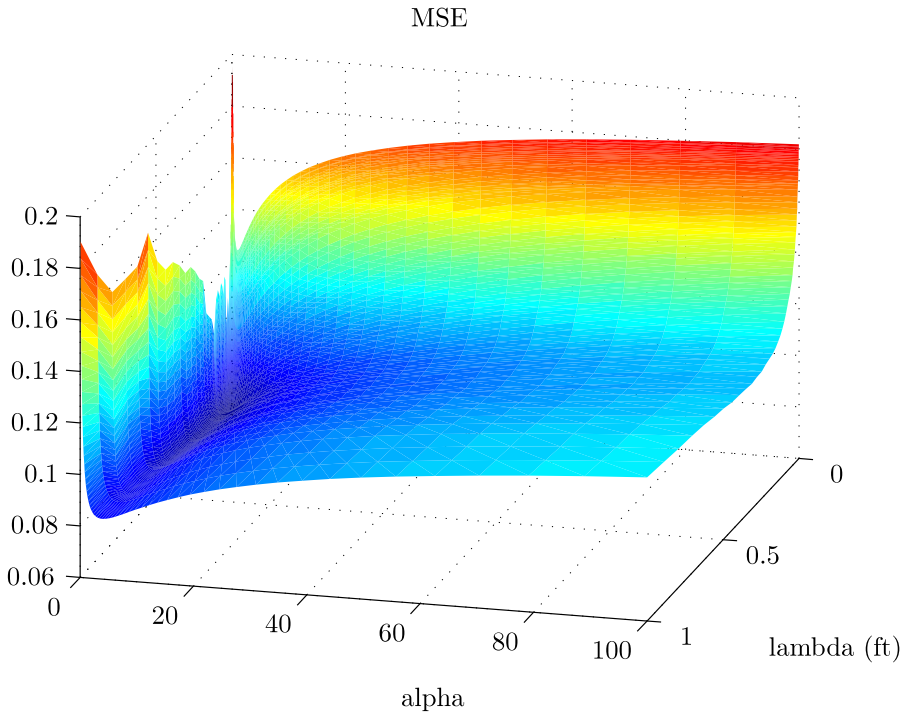

Figure 3.6: Error surface for test image 2 where λ is varied logarithmically from 10^{-3} to 10^{0} and α is varied logarithmically from 10^{-1} to 10^{2}. Note that when an appropriate value for α is chosen (i.e., in the "trough" on the error surface), the value of λ chosen has little effect on the MSE.

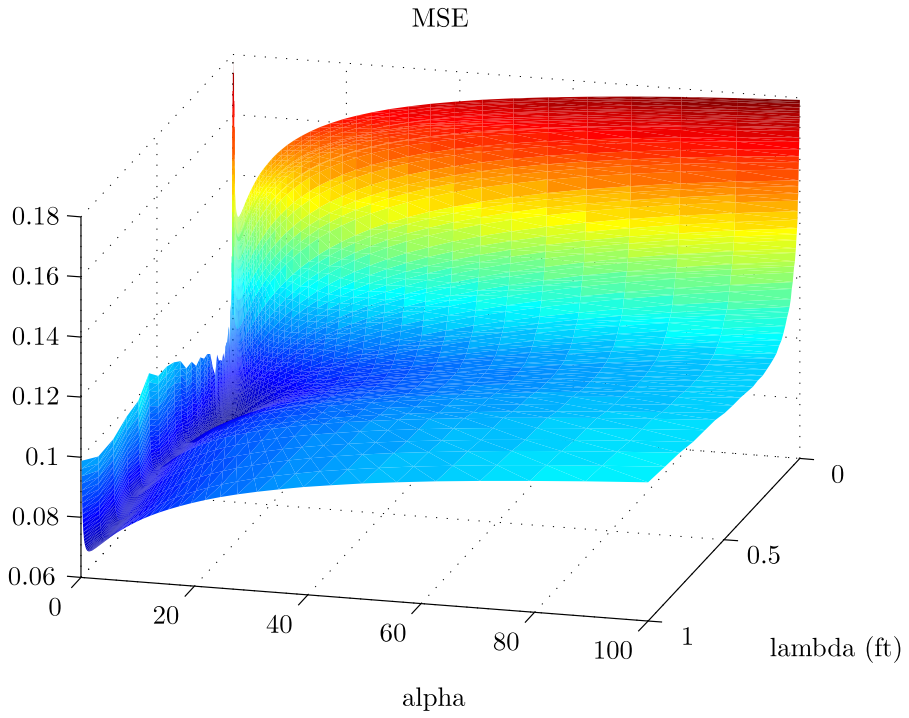

Figure 3.7: Error surface for test image 3 where λ is varied logarithmically from 10^{-3} to 10^{0} and α is varied logarithmically from 10^{-1} to 10^{2}. Note that when an appropriate value for α is chosen (i.e., in the "trough" on the error surface), the value of λ chosen has little effect on the MSE.

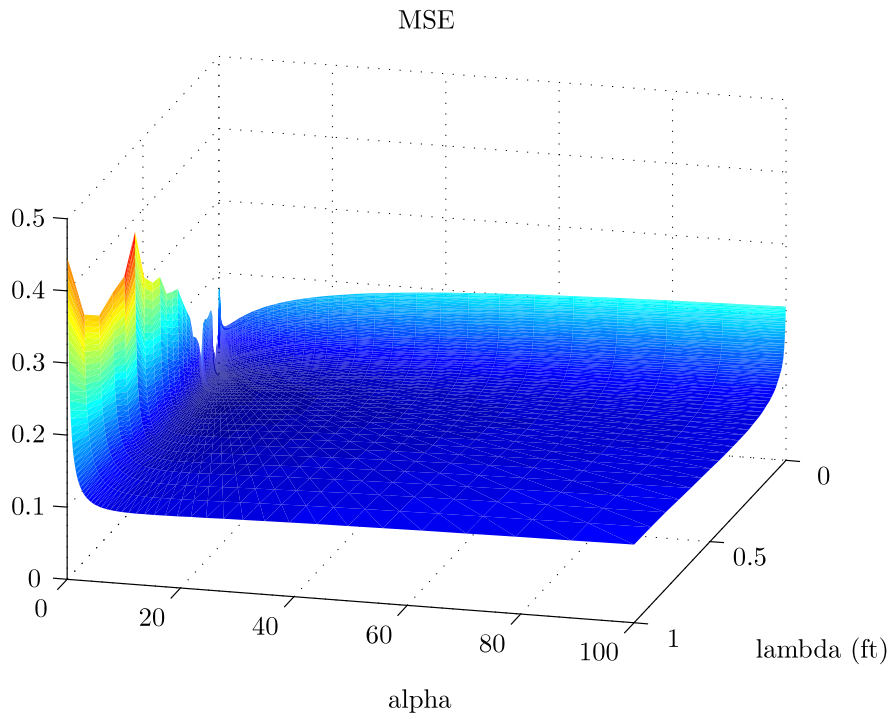

Figure 3.8: Error surface for test image 4 where λ is varied logarithmically from 10^{-3} to 10^{0} and α is varied logarithmically from 10^{-1} to 10^{2}. Note that beyond certain values of λ and α, the surface remains relatively flat, implying that the choice of α and λ have little effect on the MSE after they are raised above those critical values.

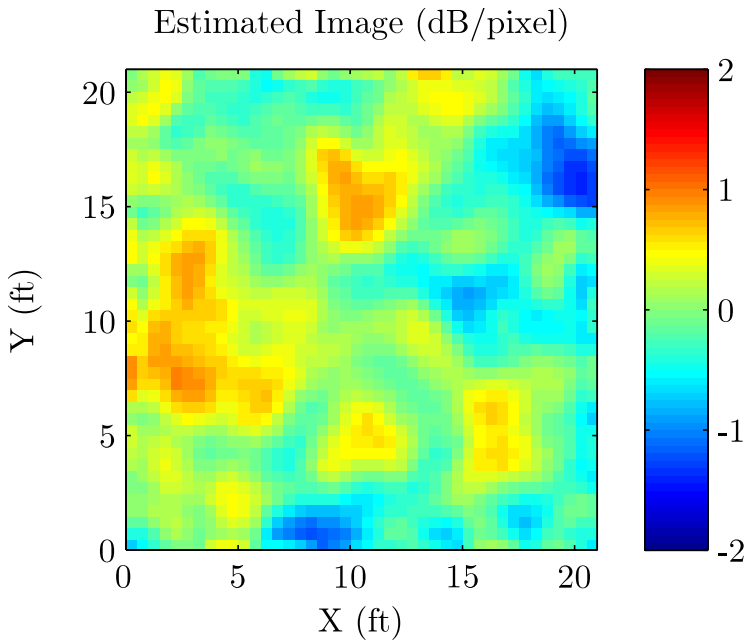

Figure 3.9: Regularized estimate of test image 1, $\sigma_n = 1$ dB.

3.2.3 Regularized Images

Using the values λ_{opt} and α_{opt}, the image reconstruction algorithm was performed on the four test images using Algorithm 2. To illustrate the effect noise can have on the regularized estimate, two values of noise standard deviation were used for each image estimate- $\sigma_n = 1$ dB and $\sigma_n = \sqrt{10}$ dB. The regularized versions of test image 1 are shown in Figures 3.9-3.10 for $\sigma_n = 1$ dB and $\sigma_n = \sqrt{10}$ dB respectively. The remaining regularized images are shown in Figures 3.11-3.16, with the corresponding test image and noise standard deviation specified in the figure caption of each figure.

Note that from all these images, the general features of the original image are preserved, but that the regularized estimates are slightly "blurrier" than the original images. Also note that when the noise standard deviation is increased $\sqrt{10}$ dB, the images do contain additional artifacts, as would be expected.

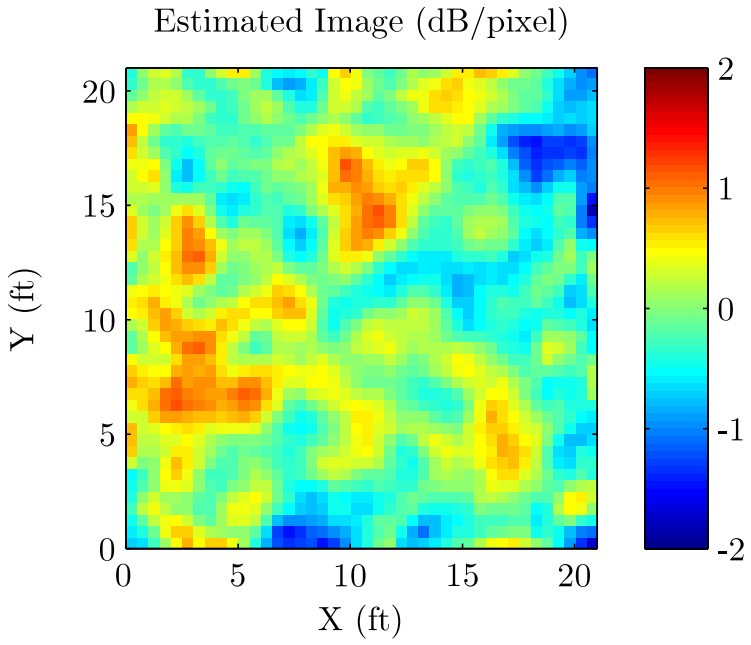

Figure 3.10: Regularized estimate of test image 1, $\sigma_n = \sqrt{10}$ dB.

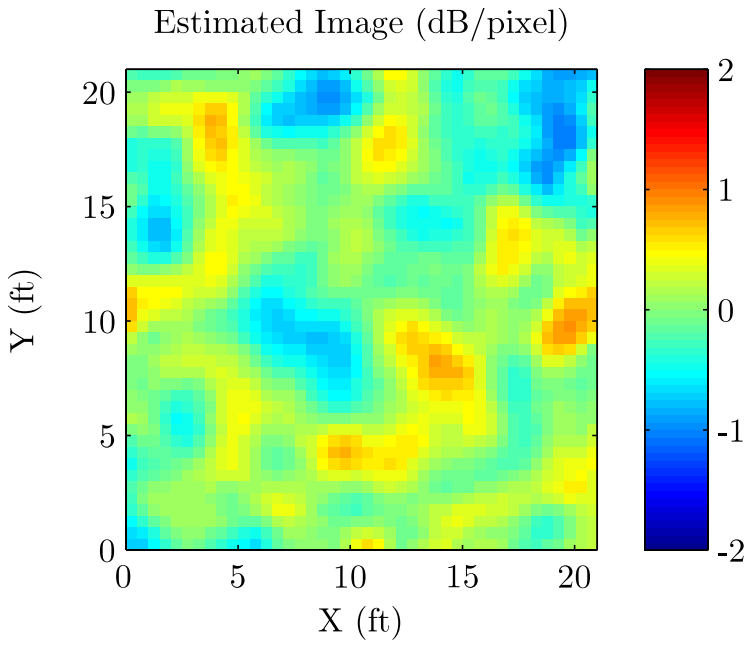

Figure 3.11: Regularized estimate of test image 2, $\sigma_n = 1$ dB.

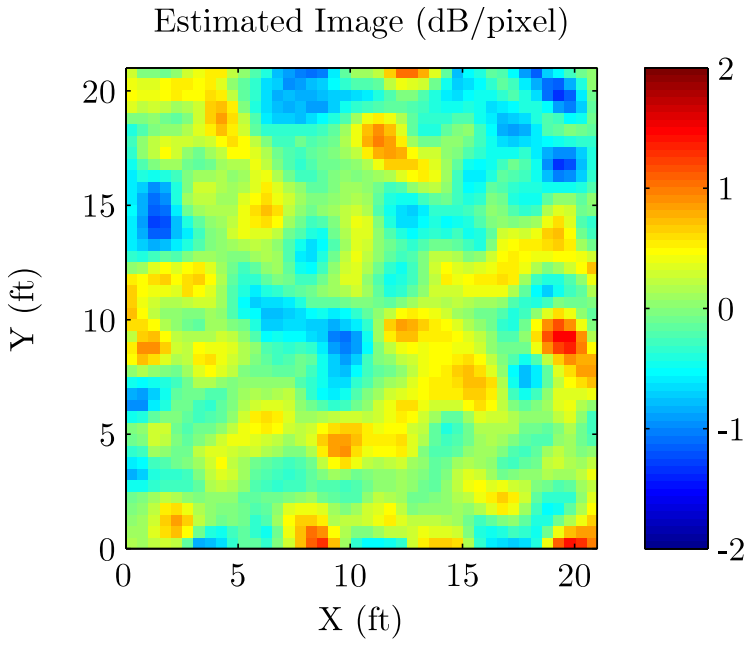

Figure 3.12: Regularized estimate of test image 2, $\sigma_n = \sqrt{10}$ dB.

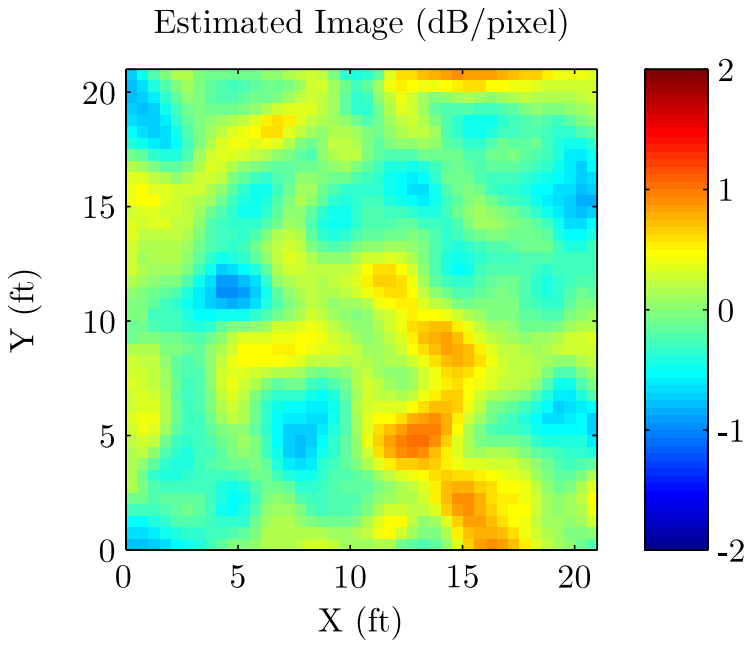

Figure 3.13: Regularized estimate of test image 3, $\sigma_n = 1$ dB.

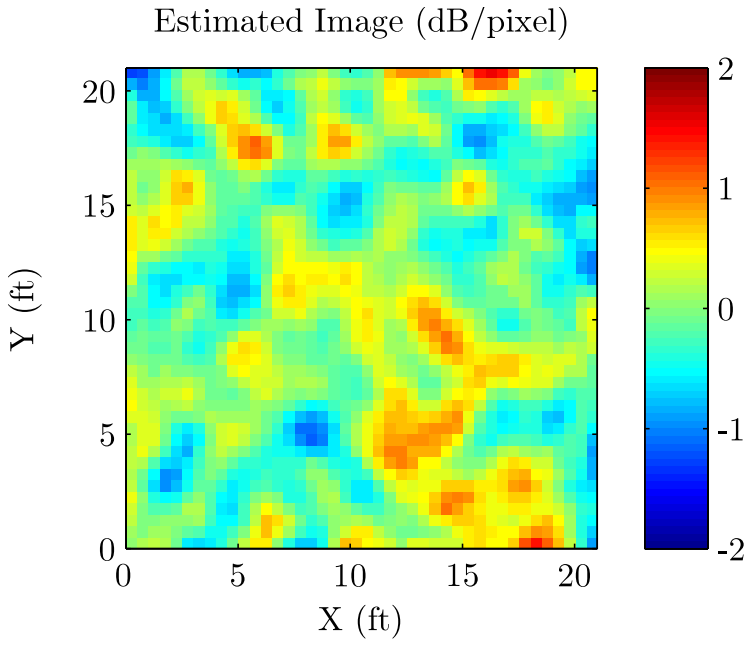

Figure 3.14: Regularized estimate of test image 3, $\sigma_n = \sqrt{10}$ dB.

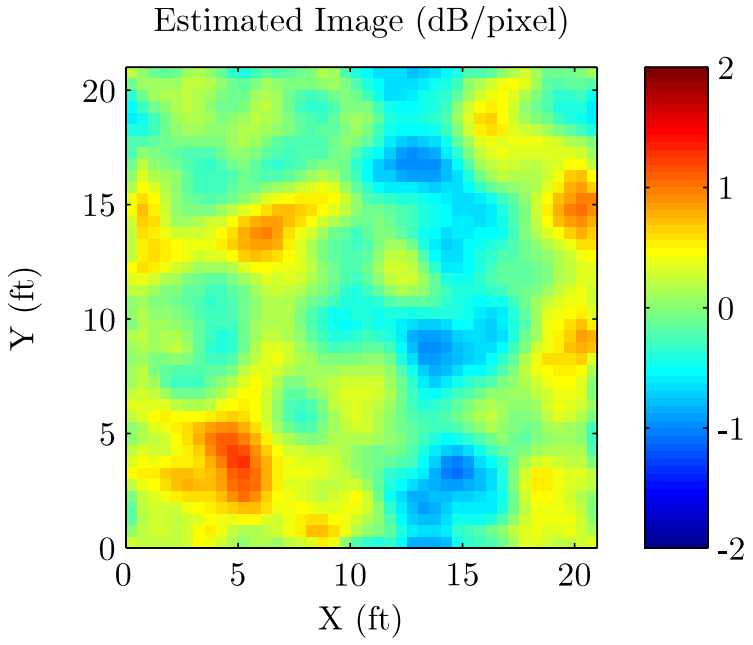

Figure 3.15: Regularized estimate of test image 4, $\sigma_n = 1$ dB.

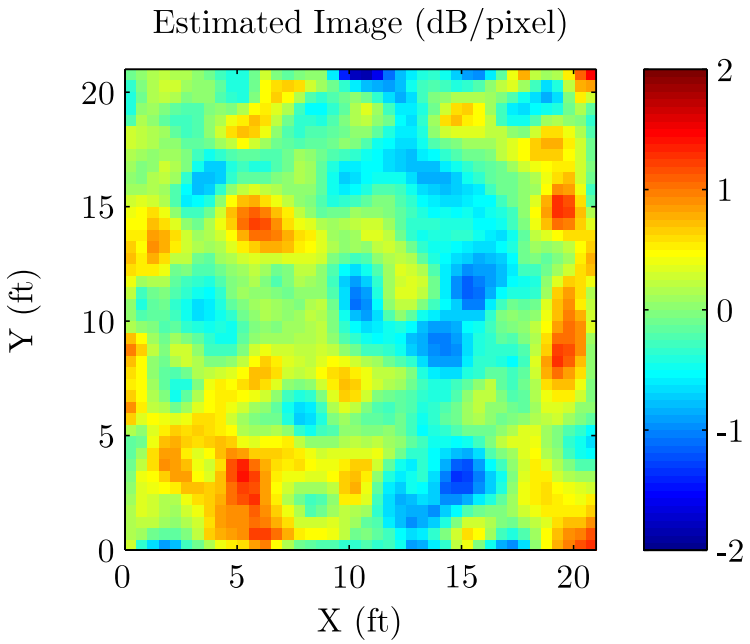

Figure 3.16: Regularized estimate of test image 4, $\sigma_n = \sqrt{10}$ dB.

3.3 RSS-Based Position Location

As was described in the previous chapter, RTI can be used to improve the quality of RSS-based position location estimates. This is due to the fact that one of the primary sources of error for RSS-based multilateration is shadowing, in that an attenuating object between the free node and an anchor node can make the free node appear to be farther away than it really is. When RTI is used to create a shadowing map of an area, these errors can be mitigated significantly. A description of how this process was simulated as well as a performance evaluation of this method as compared to traditional RSS-based multilateration will follow.

3.3.1 Simulation Setup

The radiolocation problem is posed as follows: For a given scene, an RTI system consisting of 28 sensor nodes evenly spaced around the perimeter of a 21 ft by 21 ft area is used to estimate the attenuation field for the scene. All of the 28 sensor nodes are then removed except for the nodes that lie at each corner of the square. These four nodes will be referred to as the anchor nodes. One sensor node is placed at a random position within the area, and the four anchor nodes measure the RSS from the free node. The free node itself does not communicate any information to the anchor nodes. Once the attenuation field has been estimated, and RSS measurements have been taken from the four anchor nodes, the Radial

Search Algorithm from the previous chapter (Algorithm 1) is used to estimate the position of the free node, both with and without using tomography data. The purpose of these simulations is to determine the efficacy of using the additional data provided by RTI for position location.

To calculate the vector of simulated RSS values to each anchor node, $y_{sim}(\theta) \in \mathbb{R}^4$, in (2.37), the linear problem formulation given in (2.13) is used. Node locations are specified to be at each of the four anchor node locations, the free node location, and at each location $\theta_i \in \Omega_i$, where Ω_i is the set of test points in the domain of the objective function for iteration i as is described in Algorithm 1. Once the test points have been specified, these are used to construct the matrix W in (2.13) to simulate the RSS received at each test point. For the case when the performance of traditional RSS-based multilateration is being evaluated, the tomography data is ignored, and only the exponential path loss model is used to simulate RSS at the test points (with $P_{0,dB}$ and n_p chosen beforehand).

The search space used in the radial search algorithm can be described as follows:

- $\Omega_1 = \{$square gridding of S evenly spaced points per side on the interval $x \in [\epsilon, 21 - \epsilon], y \in [\epsilon, 21 - \epsilon]\}$. (The spacing constant ϵ is included to avoid singularities in the objective function at the corners of its domain where the anchor nodes lie.)
- $\Omega_i = \{$square gridding of D evenly spaced points per side within radius $\sqrt{2}\delta_{i-1}$ of $\hat{\theta}_{i-1}\}$, $i > 1$. (Points outside the circle are discarded.)

Once again, for reference, the search process is illustrated in Figure 2.19. In this figure, $S = 15$, $D = 11$, $\epsilon = 0.1$ ft, and $\delta_{min} = 0.1$ ft. The blue x's represent the points in the domain of the objective function searched when tomography is accounted for; the green x's represent points searched when tomography data is ignored.

3.3.2 Results

To be able to make general statements about the performance of RTI-aided RSS-based multilateration, it was necessary to test the performance in a wide variety of situations to show that the performance is consistently better than traditional RSS-based multilateration. To achieve this objective, a random attenuation field and free node location were chosen, and the performance of the two radiolocation approaches was compared for each instantiation of the random scene and transmitter location. As well, the simulation process also varied the amount of of shadowing for each scene and the amount of noise that was added at each step of the simulation process (generating noisy measurements from which the attenuation field is estimated, as well as the noise that is added to the RSS value observed by the anchor nodes).

Quantitatively, the search process was as follows: 11 different noise standard deviation values were chosen (0 dB to 10 dB, in steps of 1 dB), 3 different shadowing constants σ_X were chosen (1 dB, 5 dB, and 10 dB), and for each value of noise standard deviation/shadowing constant, a large number (either 2500 or 10000) different simulations were run. In each simulation, the following parameters were used to generate the scene:

- $\delta = 2$ ft
- $P_{0,dB} = -45$ dB
- $n_p = 3$
- $d_0 = 3$ ft
- Image dimensions = 21 ft by 21 ft
- Pixel width = 0.5 ft

with the following parameters used in the search algorithm:

- $S = 15$
- $\epsilon = 10^{-6}$ ft
- $\delta_{min} = 0.1$ ft
- $D = 11$

As well, for each scene, the free node location was chosen randomly using a uniform distribution on the interval $(0, 21)$ for both the $x-$ and the $y-$coordinates. For each scene, the Radial Search Algorithm was used both with and without tomography data to minimize the objective function in (2.37) and produce an estimate of the position of the free node. The distance error for each iteration was recorded for both cases, and the average distance error for each position location method and shadowing constant was computed as a function of noise standard deviation. The results are shown in Figures 3.17-3.19.

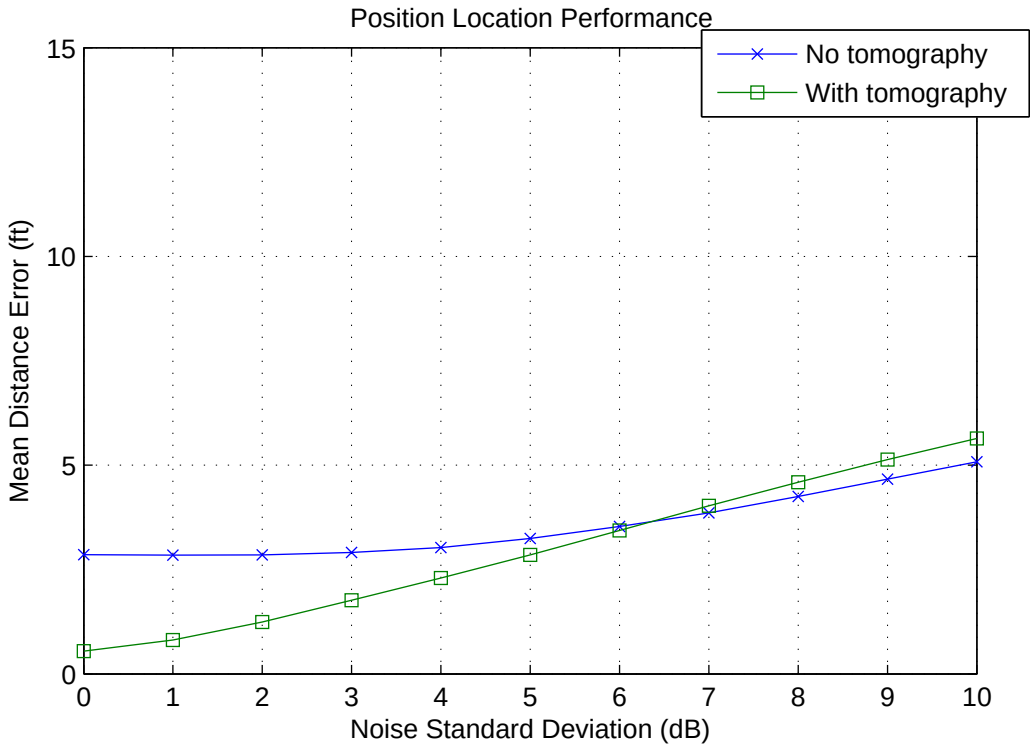

Figure 3.17: Average distance error of RSS-based position location estimates as a function of noise standard deviation, with the distance error from 10000 position estimates averaged per noise standard deviation value. For scene generation, $\sigma_X = 1$ dB, $\delta = 2$ ft, $P_{0,dB} = -45$ dB, $n_p = 3$, and $d_0 = 3$ ft were used.

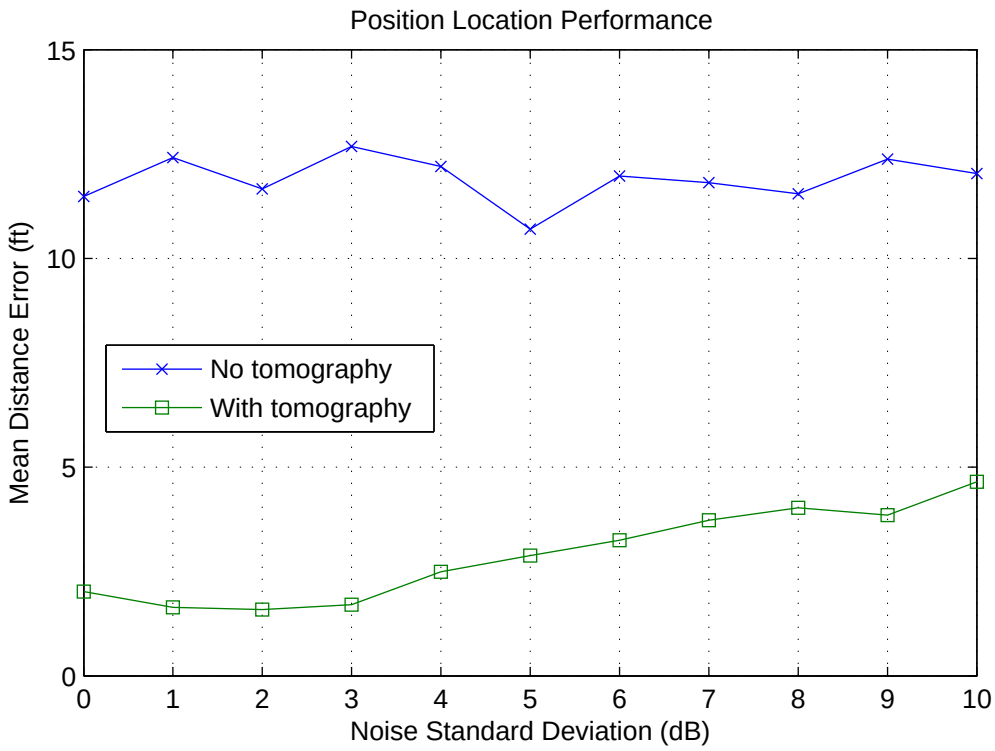

Figure 3.18: Average distance error of RSS-based position location estimates as a function of noise standard deviation, with the distance error from 2500 position estimates averaged per noise standard deviation value. For scene generation, $\sigma_X = 5$ dB, $\delta = 2$ ft, $P_{0,dB} = -45$ dB, $n_p = 3$, and $d_0 = 3$ ft were used.

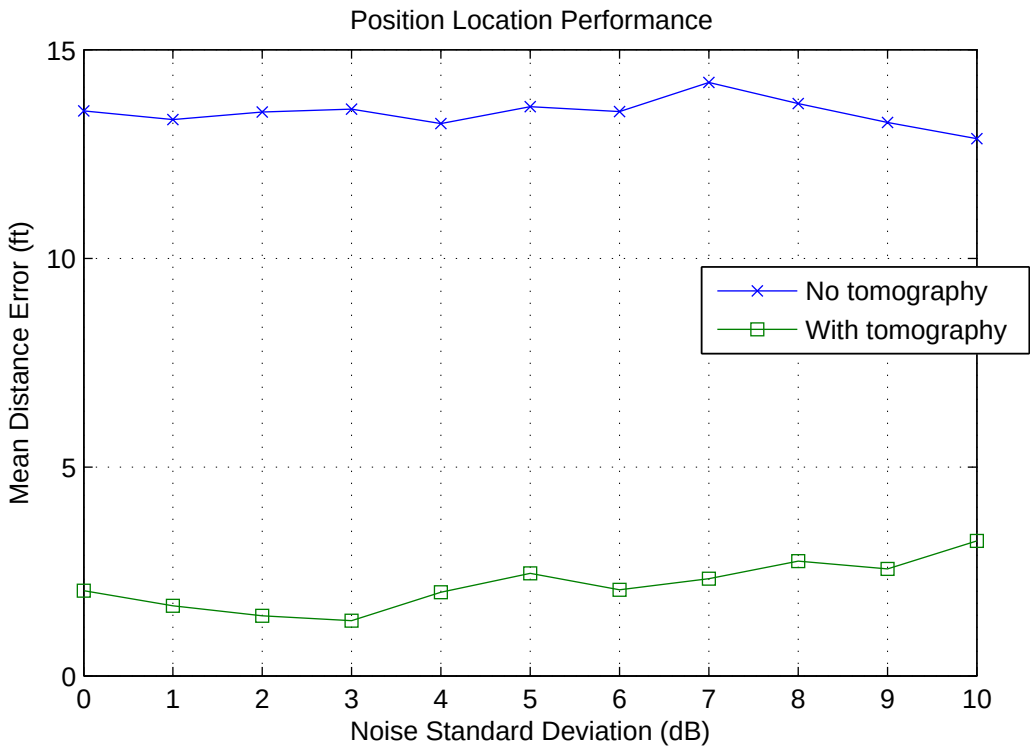

Figure 3.19: Average distance error of RSS-based position location estimates as a function of noise standard deviation, with the distance error from 2500 position estimates averaged per noise standard deviation value. For scene generation, $\sigma_X = 10$ dB, $\delta = 2$ ft, $P_{0,dB} = -45$ dB, $n_p = 3$, and $d_0 = 3$ ft were used.

Upon examining Figures 3.17-3.19, it can be observed that when RTI is used, the position location performance is usually better, especially when more shadowing is present (i.e. when σ_X is 5 or 10 dB). However, as can be seen in Figure 3.17, the improvement is not strictly better when RTI is used. As well, the fact that the RTI method tended to have higher errors than not using RTI for higher noise standard deviation values was an unexpected result. The reasons for these results are not certain; it may be due to the fact that for low values of σ_X, there is not sufficient shadowing present for RTI to afford much improvement (in the presence of no shadowing, the two methods are the same). However, it is still uncertain why the RTI method performs more poorly with high values of noise standard deviation.

3.4 Conclusion

An explanation of the methods used to simulate the performance of RTI algorithms has been given. This includes random image generation and regularized estimation as well as the evaluation of RSS-based position location methods. It has been shown that coarse image estimation is possible with regularization, and with those image estimates, it is possible to improve the performance of RSS-based position location estimates in environments where shadowing is significant. As well, it has been implicitly shown that RTI can be used for radio coverage prediction due to the fact that it was necessary to simulate RSS values at a variety of test points during the Radial Search Algorithm procedure. These methods provide additional tools that may be useful for cellular network planning and position location applications.

Chapter 4

Experimental Verification

4.1 Introduction

The purpose of this chapter will be to demonstrate the validity of the assertions made in the previous chapters- namely that radio tomographic imaging may be used as a simple method for accurate radio coverage prediction and that these estimates may be used to improve the accuracy of RSS-based position location methods. A series of experiments were performed in a variety of test environments where the RTI network was deployed. First, a description of the test environments will be given, as well as descriptions of the details of the network deployment, the experiments performed, and analysis of the results.

4.2 Test Environments

Three different test environments will be considered:

- Scene 1: Network deployed around the perimeter of a house in Christiansburg, VA
- Scene 2: Network deployed on the concrete observation deck outside the 3rd floor of Whittemore Hall at Virginia Tech
- Scene 3: Network deployed in a park on Virginia Tech campus

4.2.1 Scene 1

The measurement geometry for scene 1 is shown in Figure 4.1. The area was surveyed using a 300 ft long open-reel tape measure with fiberglass strands to minimize stretching that

occurs when the tape is put in tension. A laser-right angle was used to orient the x- and y- axes, but the other corners of the measurement area are not right angles. There was a slight grade to the measurement area which caused an elevation difference of approximately 6-10 ft over the measurement area between the highest and lowest points (the y-axis was approximately level, but the ground sloped gradually downward in the x-direction). It can be seen from Figures 4.2-4.4 that this elevation gradient is relatively monotonic.

Distances were measured along the ground using the tape measure rather than with a laser range-finder due to the difficulty of sighting the laser at long ranges during daylight conditions, and the fact that elevation angle measurements would be required in conjunction with laser range measurements for a rigorous survey, which would require professional surveying equipment and a trained observer. For these reasons, the tape measure was used, so it must be accepted that location accuracy will likely not be more accurate than approximately one foot. Measured distances are given as they were read from the tape measure in this experiment and those that follow.

The objects that lie in the field are the house (in the middle), a small shed that was approximately 2 ft tall (east of the house), and a tree near the southeastern corner of the house (as seen in Figure 4.4). The house was occupied by its residents during the measurements, so there may be minor variations in signal strength due to their movement, but this effect will be assumed to be small compared to the attenuation produced by house itself. The base-station node (which listens to network traffic and records the RSS values reported by each node) was placed inside the house because it was observed that fewer dropped packets were received at this location than if the base-station was placed outside the western boundary of the network.

The measurement nodes for the RTI network were placed with 8 evenly-spaced nodes on each side of the polygon bounding the measurement area (including corners), for a total of 28 nodes. Because each side is a different length, the node spacing on each side is different. This does not pose any problems for image reconstruction as long as the node positions are known.

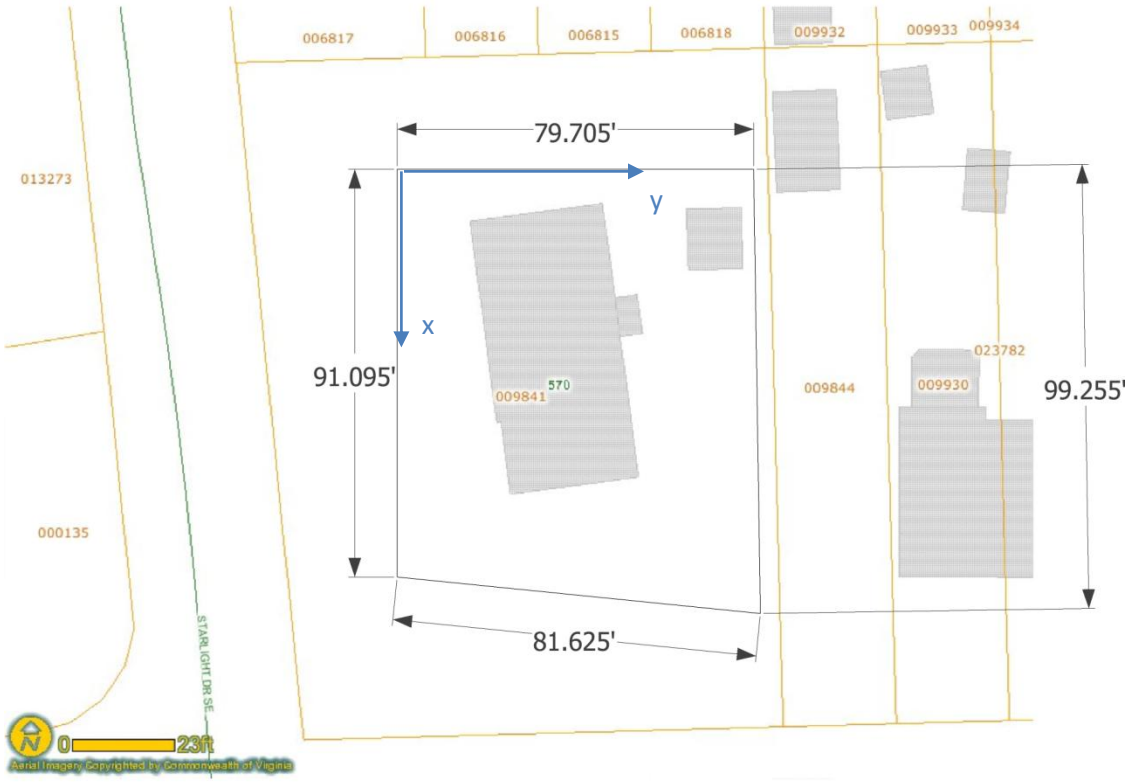

Figure 4.1: Approximate measurement geometry for scene 1. Used under fair use, 2011.

Figure 4.2: South-facing view from the western boundary of scene 1.

Figure 4.3: North-facing view from the western boundary of scene 1.

Figure 4.4: South-facing view from the northeastern corner of scene 1.

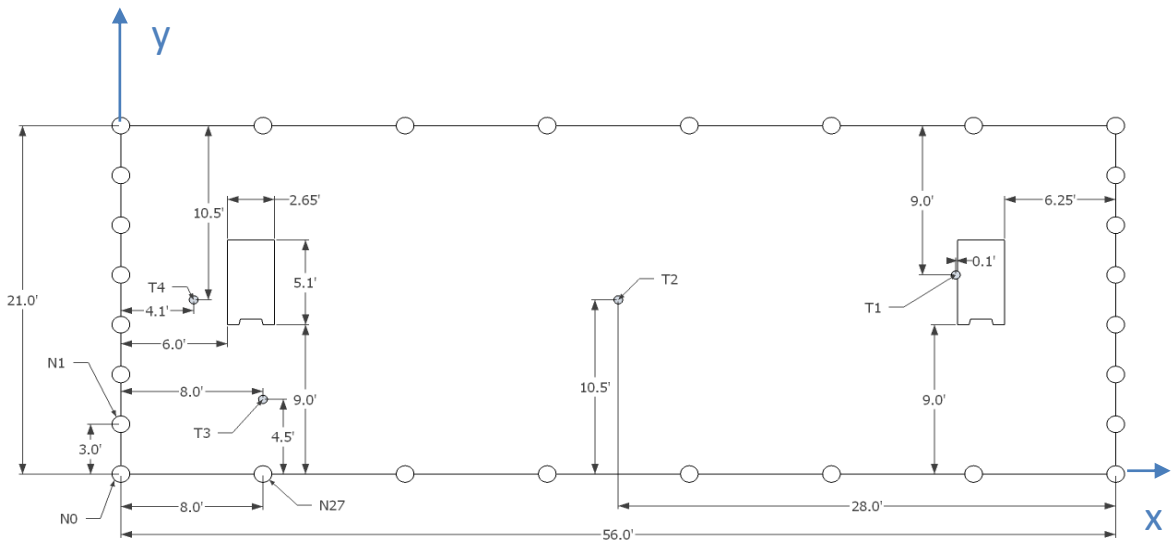

Figure 4.5: Measurement geometry for scene 2. Sensor node locations (N0 through N27 are the sensor nodes numbered in a clockwise fashion as shown in the figure) are denoted by the circles around the perimeter of the area. Test "free node" locations are designated as T1 through T4 (their use will be explained in a later section).

4.2.2 Scene 2

The measurement geometry for scene 2 is shown in Figure 4.5. A photograph of the area imaged is shown in Figure 4.6. It can be seen that the area is bounded by glass windows on one side, concrete railing on another, and has two concrete columns in the middle of the area.

Note the numbering scheme for the nodes shown in Figure 4.5– node zero (the first node) is placed at the origin of the coordinate system with two edges of the perimeter along the x- and y- axes and the node numbers increasing as you traverse the perimeter in a clockwise fashion. This geometrical convention is consistently used in every experiment.

Node positions were determined using a laser right-angle and laser range finder (which was feasible because of the shorter distances) to survey the perimeter of the rectangular area, then individual node positions were marked using a tape measure. Because the surface is flat concrete, the author is confident in the accuracy of the tape measure. However, due to wind blowing the top of the stands, and dead-reckoning error that may have occurred as we traversed the corners of the rectangle during measurement, the position accuracy of the

Figure 4.6: Photograph of deployed network at scene 2, taken from outside the network on the left side of Figure 4.5, facing in the x-direction.

sensor nodes is likely on the order of inches, despite the great care taken to survey the area.

4.2.3 Scene 3

The measurement geometry for scene 3 is shown in Figure 4.7. The area surveyed was approximately a 140 ft by 140 ft square which consists mostly of an open grassy field, with a few trees near the perimeters to serve as "test attenuators".

The area was surveyed using a combination of the open-reel tape measure with spools of string. Triangulation was used to survey the corners of the box. However due to the elasticity of the string, some error was introduced as the diagonals were measured (the tape measure, however, was very inelastic). Three of the side lengths were measured to be almost exactly 140 ft with the tape measure, but the upper left side in Figure 4.7 was measured to be 141.6 ft using the tape measure. However, this only represents a 1.143% error from the nominal length, so the error is not catastrophic. Because of the reasons, the box is not perfectly square, which means that the stated accuracy of node positions will likely be on the order of feet rather than inches. However, because of the large network size, this error is acceptable.

The test points T1-T5 for later position location experiments are located at the following coordinates (in ft):

- T1 = (20,20)
- T2 = (20,120)
- T3 = (120,120)
- T4 = (120,20)
- T5 = (70,70)

4.3 Experimental Procedures

4.3.1 Sensor Network

The sensor network consisted of 28 TelosB ZigEee radios produced by MEMSIC, Inc., with an additional radio connected to a laptop serving as a base station node to listen to network traffic. The radios transmit in the 2.4 GHz ISM band. The communication protocol used is called SPIN, which was developed by the University of Utah's SPAN Lab [29]. The protocol operates in a token-ring fashion– each node transmits in sequence then passes the "token" to the next node in the "ring", which then receives permission to transmit while all other nodes listen. If a node does not receive the message that it has been passed the token, the other nodes will wait a specified amount of time, then the next node in the sequence will automatically transmit. This allows the network to be very robust against dropped packets, as the nodes will simply skip the "bad node" and continue transmitting until the "bad node" is able to receive the message.

Each node records the RSS from each other node as they transmit in a buffer; when it is this node's turn to transmit, it will transmit the contents of the buffer (the last recorded RSS value from each other node) to all other nodes. The receiving nodes don't actually record the information that is transmitted– they only record the RSS. The base-station node, however, records the contents of all packets that are transmitted to a text file on the laptop for post-processing. It takes approximately half a second for the token to traverse the entire ring, so one may obtain several hundred RSS measurements within only a few seconds. In this fashion, one may obtain RSS values between every possible combination of node pairs within a very short time.

According to the data sheet for the CC2420 RF transceiver used in the TelosB radios [26], the RSSI values reported by the radio are in dB units with a reference power level of approximately -45 dBm. This value, however, is not exact and must be determined experimentally,

Figure 4.7: Approximate measurement geometry for scene 3. Used under fair use, 2011.

Figure 4.8: North facing view from the southern corner (the origin of the coordinate system) of scene 3.

so for the measurements presented in this thesis, we will use the RSSI values reported by the radio directly, as the choice of reference level has no effect on the quality of image estimates. The receiver has a sensitivity of approximately -95 (typ) to -90 (min) dBm, and an input saturation level of approximately 0 (min) to 10 (typ) dBm. This yields a dynamic range of approximately 100 dB. In terms of RSSI values reported by the radios, the minimum values reported will be approximately -50 to -45 dB, and the maximum valid values will be approximately 45 to 55 dB. In the experiments performed in this chapter, RSSI values never exceeded 10 dB, so there was no distortion in the measurement data due to compression.

4.3.2 Optimal Regularization Parameters

Because the measurement geometries discussed in this chapter are different than that simulated in the previous chapter, the same procedure was used for the new geometries to determine the optimal values of λ and α for image reconstruction. For the geometry of scenes 1 and 3, 3 random images were generated for each scene, and a 50 point by 50 point test point grid was used for λ and α for each random image. λ was varied logarithmically from 10^{-1} to $10^{1.5}$ and α was varied logarithmically from 10^{-1} to 10^{1}. The values of λ and α that lead to the least estimation error for each image were averaged to obtain the "optimal" values for each geometry. The following values were obtained:

- Scene 1: $\alpha = 1.0577$, $\lambda = 0.8112$ ft
- Scene 3: $\alpha = 1.1020$, $\lambda = 0.4691$ ft

Because the pixel size was the same for scene 2 as the scene simulated in the previous chapter and the network area is of the same order of magnitude, the same values for α and λ that were obtained in the previous chapter will be used.

4.3.3 Image Estimation

Using the regularization parameters from the previous section, a series of numerical experiments was performed on the data recorded from each scene. The first of which is estimating the "empty" scene, i.e., where there is no motion in the area of interest. These images were obtained by taking RSS measurements over an extended period of time (60s for scenes 1 and 2, and 30s for scene 3) averaging across every timestep, and then averaging the forward and reverse RSS for each two-way link to construct the vector y from (2.13). The reason for averaging over time is to ensure that the effect of any short term fluctuations in the RSS due to moving scatterers outside the network, interference, wind causing the radio stands to wobble, or other sources of noise are minimized. Because the transceivers in the RTI network are approximately stationary (except for the small amount wind causes the stands

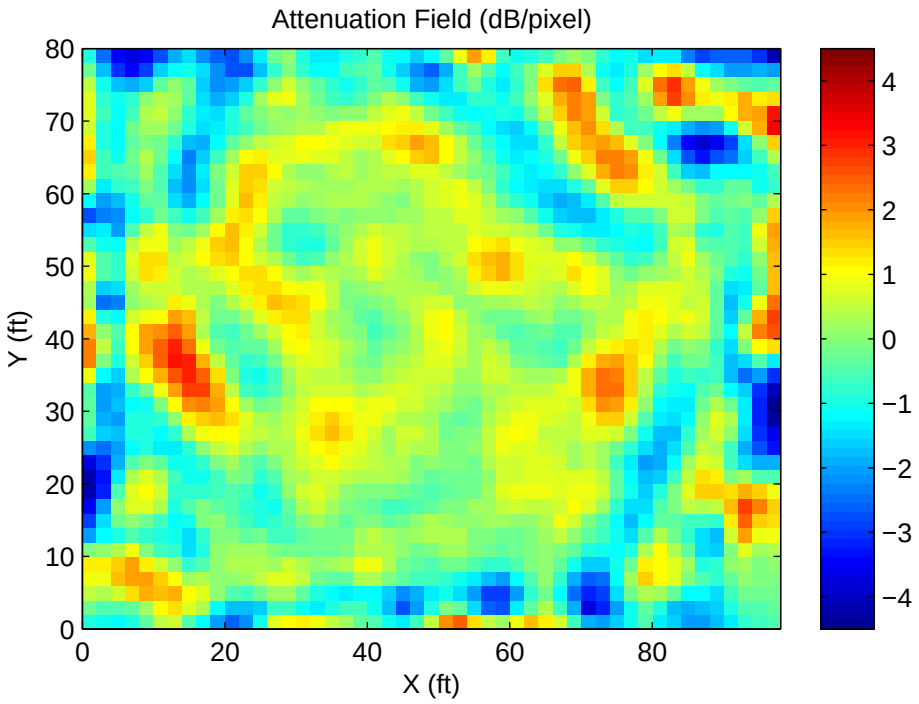

Figure 4.9: Estimated image for scene 1 (empty).

to wobble around the same location), the doppler spread of the channel will be near-zero, which means that the channel coherence time (which is approximately inversely proportional to the doppler spread), will be very large. In other words, because the physical layout of the channel is not changing in a uniform manner, the multipath profile will not vary significantly, and thus we will assume that any fluctuations that occur can be mitigated by time-averaging.

The estimator from (2.24) was used to estimate the image vector x. The resulting image estimates are shown in Figures 4.9-4.11.

It can be observed that while the images look rather "blobby", some salient features do appear. It can be seen in Figure 4.9 that areas of increased attenuation do occur mainly in the vicinity of the house and the tree locations. It can be seen in Figure 4.10 that small areas of increased attenuation roughly appear at the location of the concrete columns. It can be seen in Figure 4.11 that areas of increased attenuation do appear roughly at the tree locations. However, it should be noted that several artifacts do appear around the perimeters of all three images– the reasons for these are not entirely clear, but it may be due to several factors, including antenna pattern irregularities, multipath interference, limitations in the linear problem formulation, or the relative sparsity of radio links crossing pixels near the perimeter of the area.

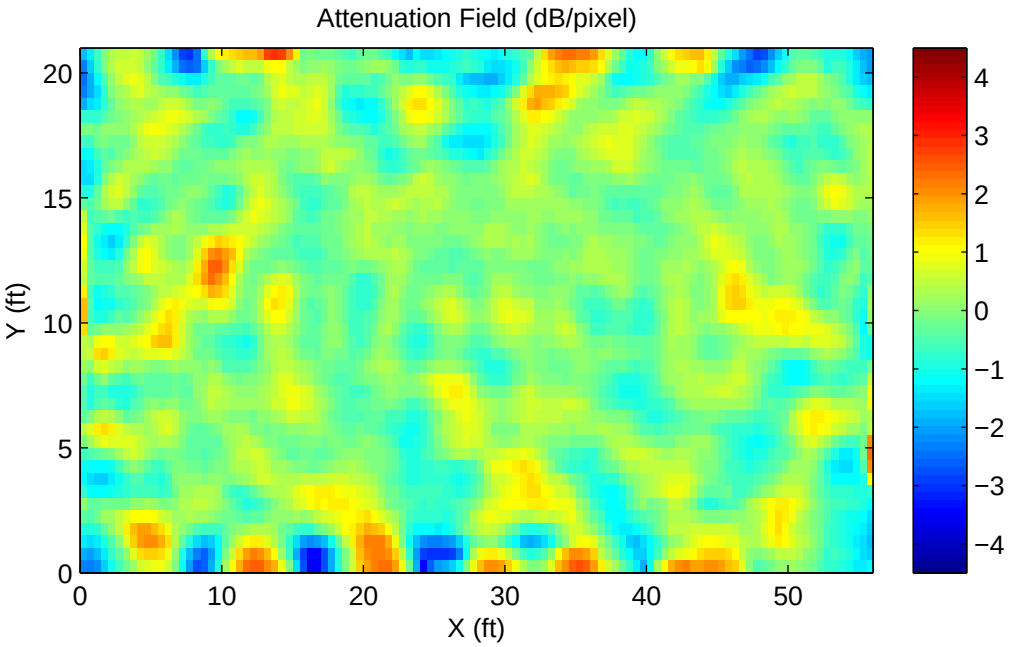

Figure 4.10: Estimated image for scene 2 (empty).

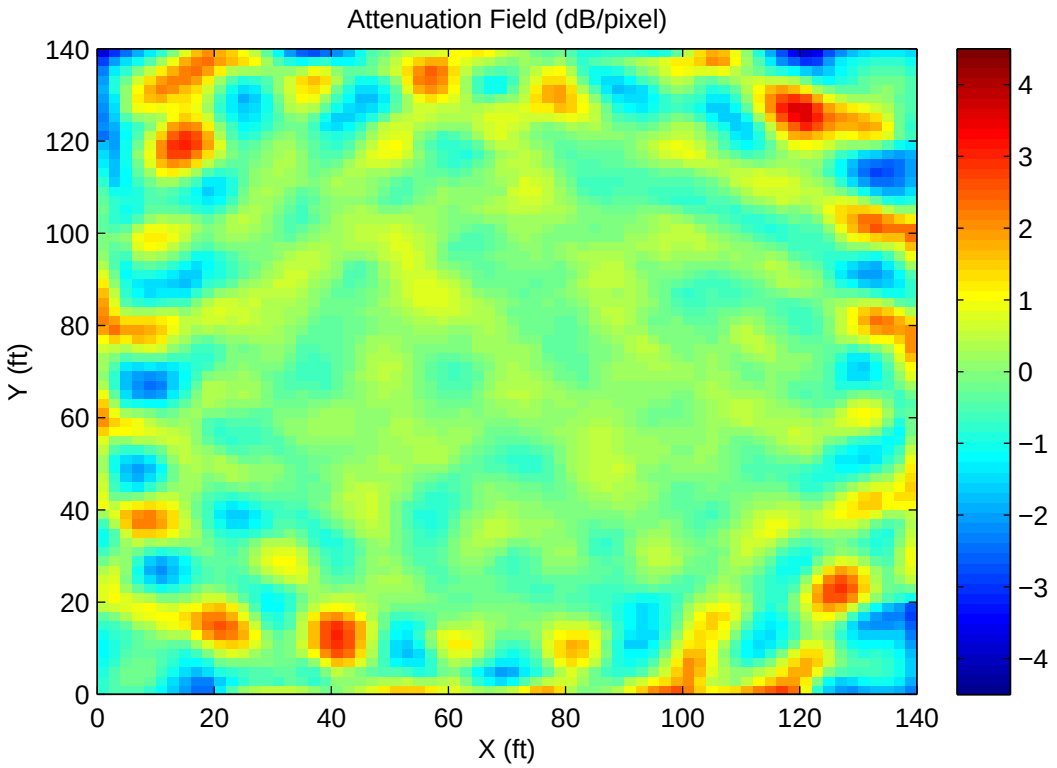

Figure 4.11: Estimated image for scene 3 (empty).

4.4 Radio Coverage Prediction

As has been previously mentioned, RTI can be used as a relatively simple method for radio coverage prediction. Due to the large amount of RSS data that can be measured by an RTI network, this claim will now be evaluated.

The first step is estimating the path loss exponent and relative reference power from (2.19). For all plots, a reference distance of $d_0 = 3$ ft was chosen (the choice is arbitrary). The time-averaged RSS values from each empty scene are then plotted versus $\log_{10}(d/d_0)$, and the results are shown in Figures 4.12-4.14. Linear least-squares regression was used to estimate the path loss exponent and relative reference power, and the resulting best-fit lines are plotted (dashed blue) in the corresponding figures. These best-fit lines represent the mean received power as a function of distance. The path loss exponents and relative reference powers obtained from the data are as follows:

- Scene 1: $P_{0,dB} = 10.3$ dB, $n_p = 3.3$
- Scene 2: $P_{0,dB} = -2.1$ dB, $n_p = 2.0$
- Scene 3: $P_{0,dB} = -11.6$ dB, $n_p = 1.3$

It can be observed that where there are more obstructions, the estimated path loss exponent is higher, as expected. However, the fact that for scene 3 (largely open field), the path loss exponent is significantly less than 2 is curious. However, it should be noted that the estimated relative reference power, $P_{0,dB}$ for scene 3 is significantly lower than it is for the other two cases, which significantly compensates for the decreased decay of signal strength with distance.

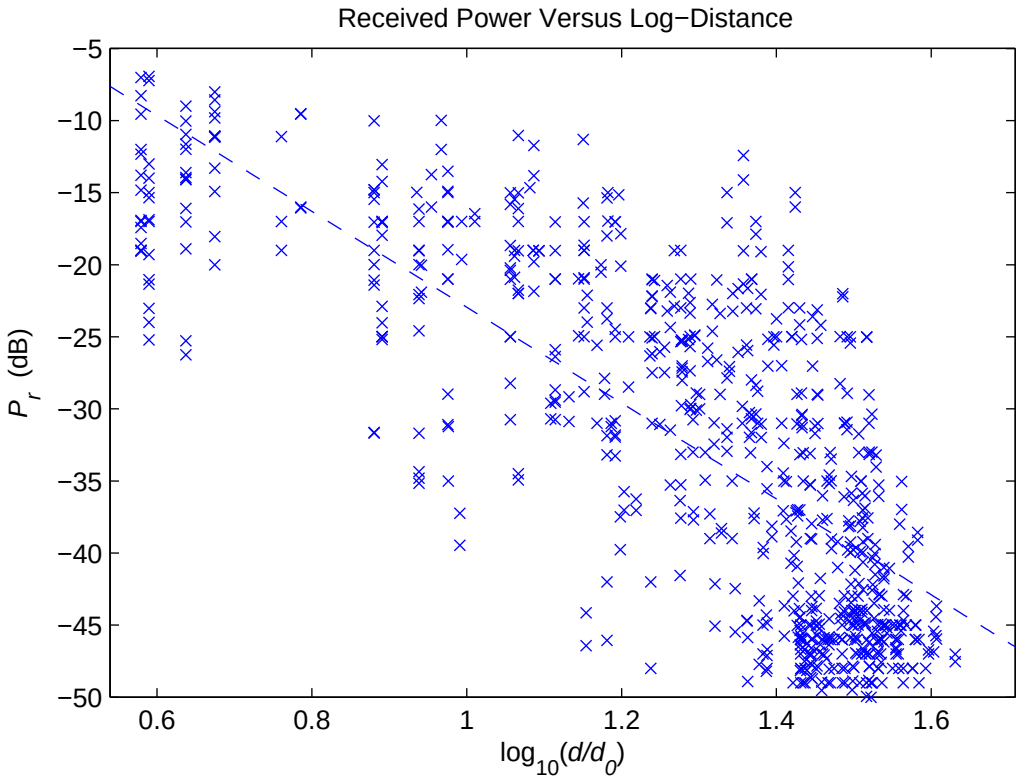

Figure 4.12: RSS versus log-distance for scene 1 (empty).

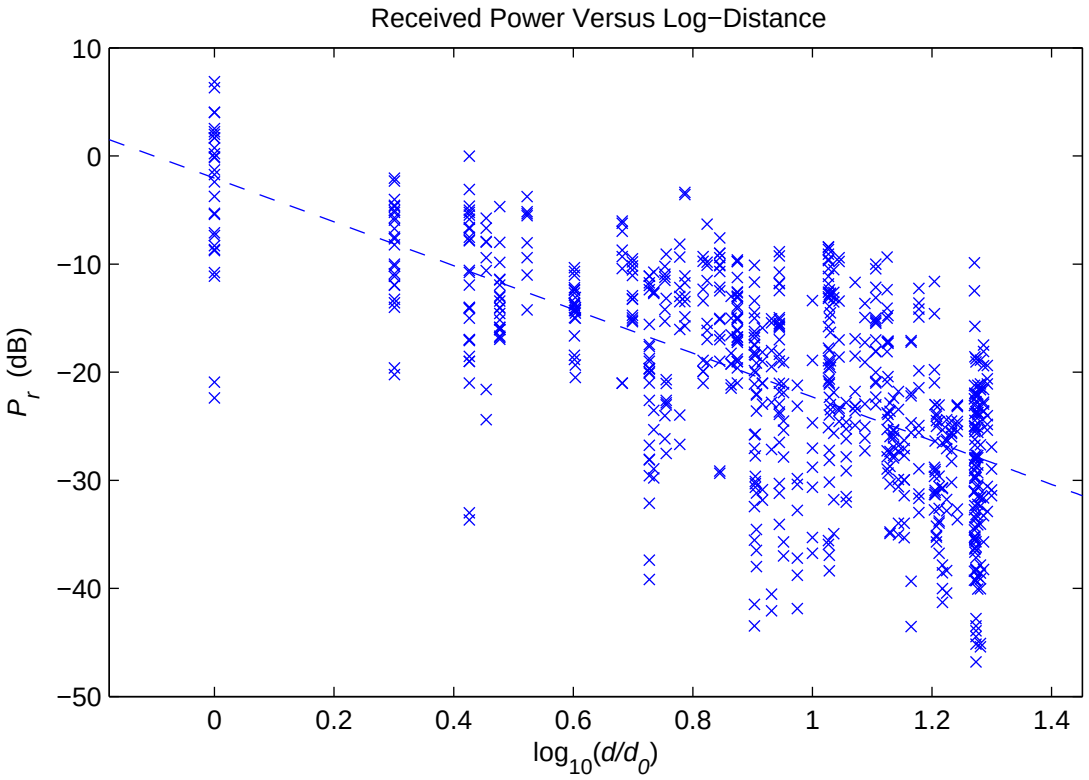

Figure 4.13: RSS versus log-distance for scene 2 (empty).

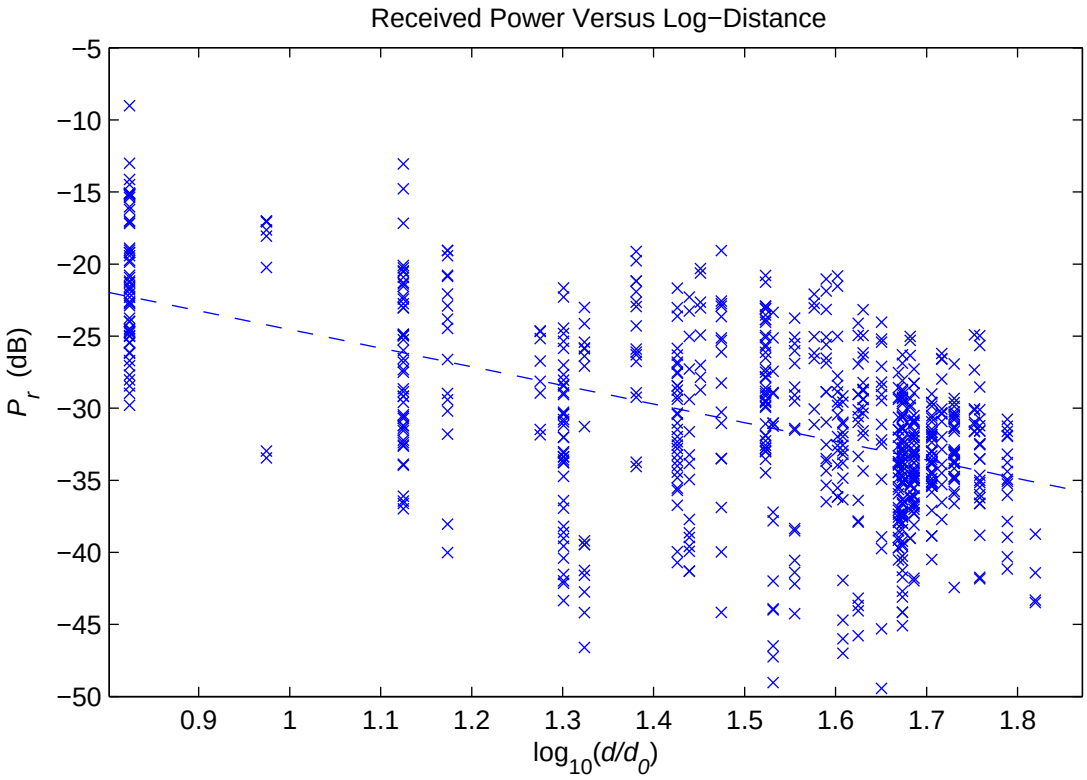

Figure 4.14: RSS versus log-distance for scene 3 (empty).

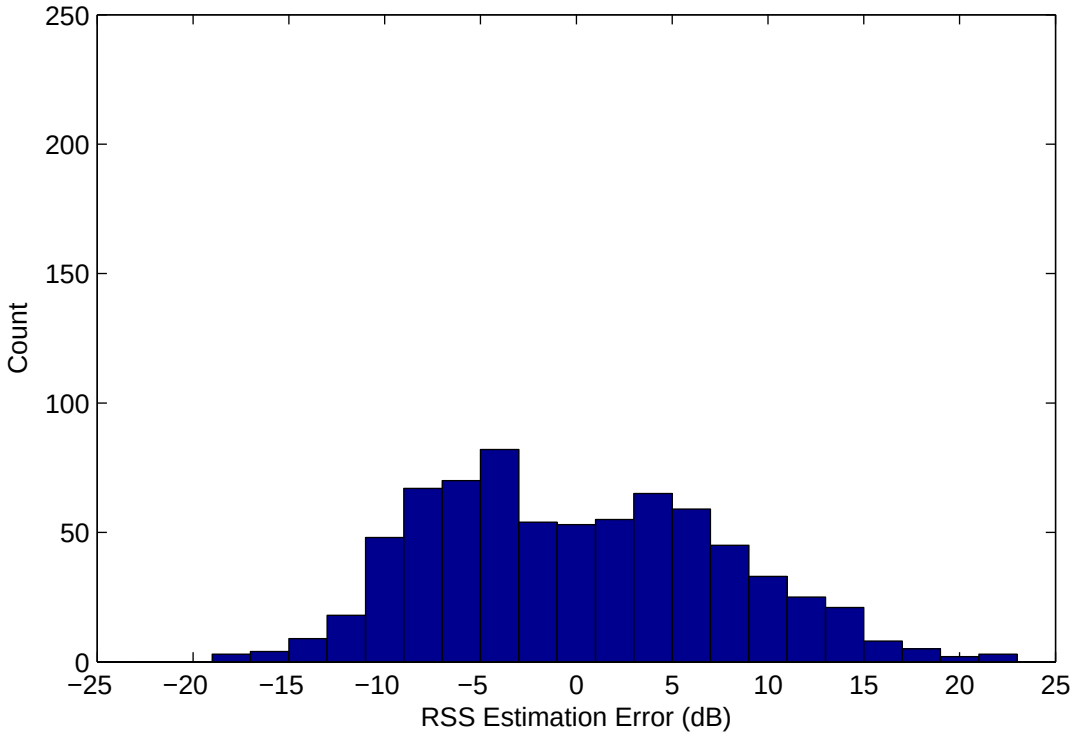

Figure 4.15: Histogram of RSS estimation error without using RTI for scene 1 (empty).

To evaluate the performance of utilizing RTI to predict RSS values for a given network, the estimated RSS was computed using (2.36) from the time-averaged RSS measurements from each empty scene, and the difference between the measured and simulated values was evaluated.

Consider the histograms shown in Figures 4.15-4.16, which show the distribution of estimation errors from the measurements taken from an empty scene 1, without and with utilizing RTI, respectively, to produce RSS estimates. It can be seen that by comparing these two figures that when RTI is used, the histogram of errors is significantly more concentrated about zero, whereas when only the exponential path loss model is used, the error distribution is much more heavy-tailed. This lends weight to the claim that RTI can significantly improve RSS estimates. Improvement was observed in all three cases; however for brevity's sake, only the plots related to scene 1 will be shown. The reader is referred to Appendix A for the remaining figures.

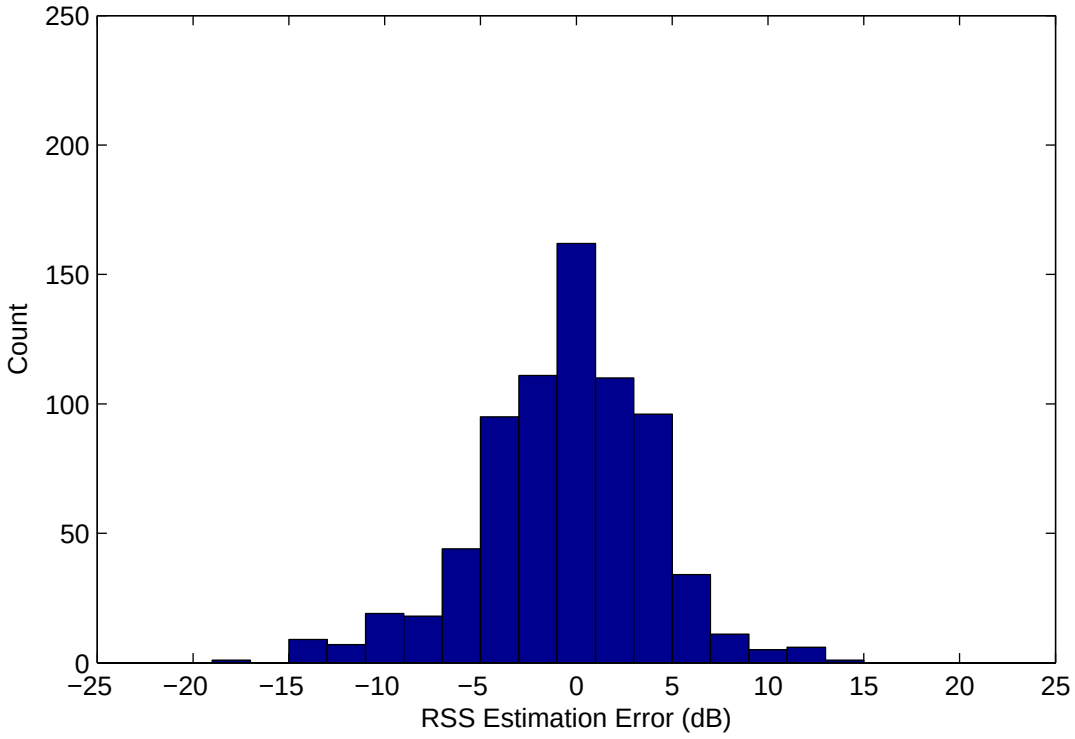

Figure 4.16: Histogram of RSS estimation error with using RTI for scene 1 (empty).

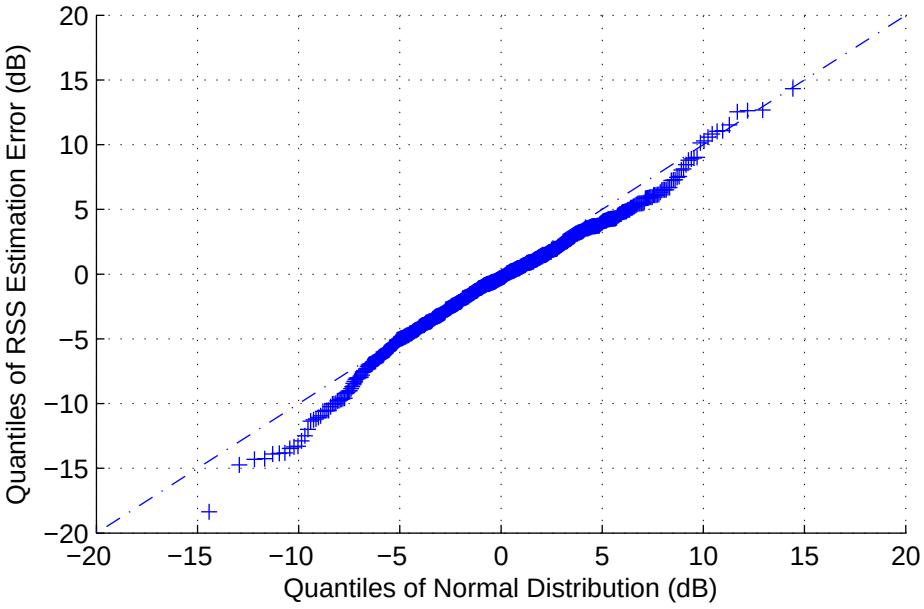

Figure 4.17: Q-Q Plot of RSS estimation error (with using RTI) versus normal distribution for scene 1 (empty). The dashed blue line (which has a slope of 1) is plotted for reference.

Table 4.1: RSS estimation error statistics without (EXP) and with (RTI) tomography.

Scene	μ_{EXP} (dB)	σ_{EXP} (dB)	μ_{RTI} (dB)	σ_{RTI} (dB)
1	0.0	7.7	0.5	4.5
2	0.0	7.3	0.0	3.8
3	0.0	5.4	0.0	3.1

Heuristically, it can be observed in Figure 4.16 that the errors (when RTI is used) appear roughly to follow a Gaussian distribution. To test this assertion, a method similar to that employed by Wilson [2] will be used. A quantile-quantile (Q-Q) plot was constructed with the x-axis as the quantiles of a zero-mean Gaussian distribution with standard deviation σ_e (the sample standard deviation of the estimation error), and the y-axis as the quantiles of the estimation errors. This is shown in Figure 4.17. If the data follow the specified distribution, the points of the Q-Q plot will be perfectly linear with a slope of 1. It can be seen from Figure 4.17 that the data do very closely follow the specified distribution, especially within ± 5 dB of the mean.

The histograms and Q-Q plots for the other two scenes (both empty) can be seen in Appendix A. For reference, the calculated sample mean and standard deviations of the estimation error (using only the exponential path loss model (denoted by subscript EXP) and using tomography (denoted by subscript RTI)) for each case are shown in Table 4.1. It can be seen that from this table that in each scene, the standard deviation was noticeably less when tomography was used. As well, for 2 of the 3 scenes, the mean estimation error was zero with RTI. The reason that the exponential path loss model alone has a zero-mean estimation error is because the linear least-squares regression process forces the mean to be zero to compute the line that best fits the data points.

Now that the estimation error has been characterized with a distribution (Gaussian) and a measurable parameter (the error standard deviation), realistic bounds on the accuracy of RSS estimation may be obtained using the well-known Gaussian cumulative distribution function (CDF). For example, using the sample standard deviation from the scene 1 data, one may assert that there is a 68.27% chance that the measured RSS for a given link will lie within ± 4.5 dB of the estimated value (using the Gaussian CDF to compute the probability).

4.5 Tomography-Aided Radiolocation

Once the attenuation field for an area has been estimated, the additional information can be used to improve position location estimates that rely on RSS-trilateration. Two sets of experiments were performed:

- Moving N27 (the last node) to a specified location (i.e. T1, T2, etc.), and using only the data from nodes N0, N7, N14, and N21 as "anchor nodes" to locate the free node using RSS-trilateration, and
- Using only the RSS data from nodes N0, N7, N14, and N21 and leaving all other nodes in their original positions at the perimeter of the network and sequentially designating each other node as the "free node" to be located.

Algorithm 1, the Radial Search Algorithm, was used to obtain the position estimates by searching over the entire measurement area with the following parameters:

- $\Omega_1 = \{$rectangular gridding of S evenly spaced points per side on the interval $x \in [\epsilon, x_{max} - \epsilon], y \in [\epsilon, y_{max} - \epsilon]\}$, where (x_{max}, y_{max}) is the upper right corner of the highest numbered pixel (using the convention given in Figure 2.8).
- $\Omega_i = \{$square gridding of D evenly spaced points per side within radius $\sqrt{2}\delta_{i-1}$ of $\hat{\theta}_{i-1}\}$, $i > 1$. (Points outside the circle are discarded.)

with:

- $S = 15$
- $\epsilon = 0.1$ ft
- $\delta_{min} = 0.1$ ft
- $D = 11$

The results from the two sets of experiments will be given below.

4.5.1 Repositioned Test Node Location Experiments

As was mentioned previously, N27 was chosen as the free node and was moved to series of test locations (T1, T2, etc.) while N0, N7, N14, and N21 were used as the anchor nodes (and were not repositioned) to locate N27 using only the RSS data from the four anchor nodes. The position of N27 was estimated using the Radial Search algorithm. This set of

Table 4.2: Position location performance for scene 2.

Test Position	Truth	Est. w/ RTI	Est. w/o RTI	RTI Error	w/o RTI Error
T1	(47, 12)	(23.8, 3.8)	(24.0, 21.0)	24.6 ft	24.7 ft
T2	(28, 10.5)	(22.1, 16.3)	(46.3, 17.6)	8.3 ft	19.6 ft
T3	(8, 4.5)	(11.3, 13.4)	(12.8, 20.5)	9.5 ft	16.7 ft
T4	(4.1, 10.5)	(2.0, 10.1)	(0.0, 18.9)	2.1 ft	9.4 ft
Average				11.1 ft	17.6 ft

Table 4.3: Position location performance for scene 3.

Test Position	Truth	Est. w/ RTI	Est. w/o RTI	RTI Error	w/o RTI Error
T1	(20, 20)	(0.4, 12.5)	(0.0, 5.8)	21.0 ft	24.5 ft
T2	(20, 120)	(40.2, 137.9)	(29.4, 137.2)	27.0 ft	19.6 ft
T3	(120, 120)	(102.5, 133.6)	(140.0, 135.4)	22.1 ft	25.2 ft
T4	(120, 20)	(140.0, 18.5)	(133.8, 0.0)	20.0 ft	24.3 ft
T5	(70, 70)	(121.5, 81.2)	(123.5, 20.2)	52.7 ft	73.1 ft
Average				28.6 ft	33.3 ft

experiments was performed on both scene 2 and scene 3. The results are summarized in Tables 4.2-4.3, where the column labeled "Truth" is the true position, and the next two columns are the estimated positions using the Radial Search Algorithm with and without RTI, respectively.

The estimated and true locations for test position T1 for scene 2 are shown in Figure 4.18. It can be seen from this figure that even though the magnitude of the distance errors for both methods were almost the same, the location estimated provided by the two methods are separated by a significant distance. While this is not always the case, it does happen with some regularity. Graphical representations of the true and estimated positions for all test cases can be found in Appendix B.

It can be seen from Tables 4.2-4.3 that utilizing RTI to account for shadowing can result in significant improvements to location accuracy. For scene 2, the RTI method performed better in every case, and for scene 3, the RTI method performed better in every case except one.

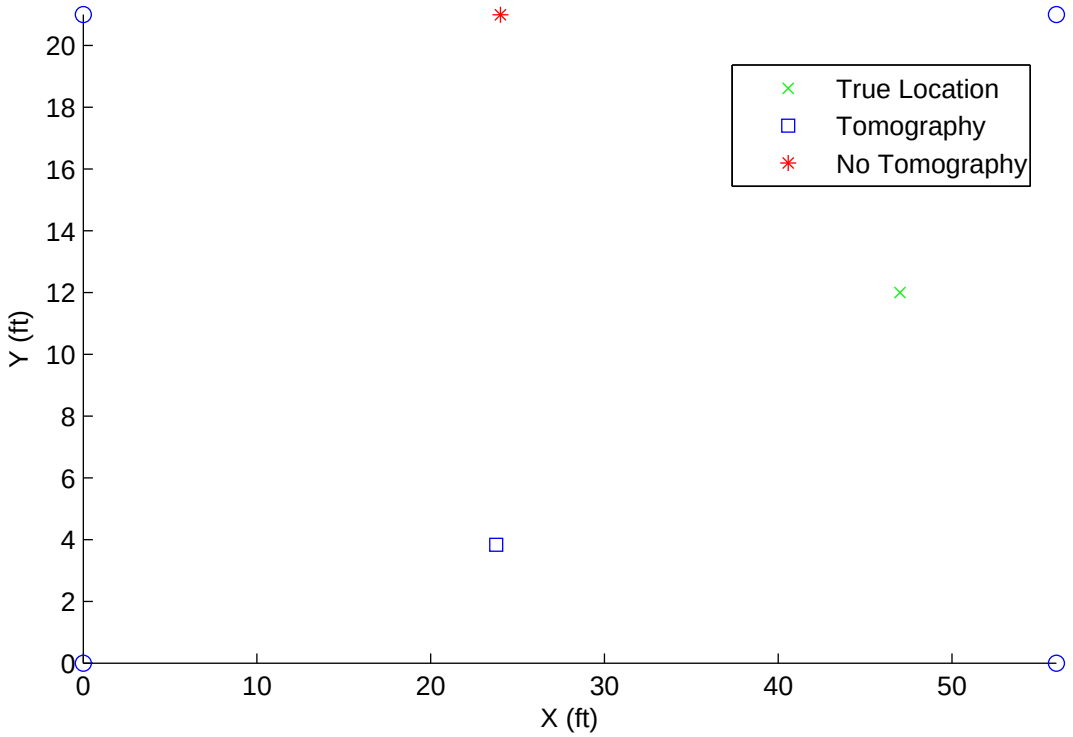

Figure 4.18: Location estimates with and without tomography for node position 1 in scene 2. The blue circles represent anchor node locations.

Table 4.4: Position location performance for perimeter node experiments.

Scene	Mean Error w/ RTI (ft)	Std Dev (ft)	Mean Error w/o RTI (ft)	Std Dev (ft)
1	9.9	6.9	13.6	9.4
2	7.5	10.6	8.3	9.2
3	30.3	31.6	30.3	22.1

4.5.2 Perimeter Node Location Experiments

As was mentioned previously, in this set of experiments, all the sensor nodes remained in their original positions, and the free node was chosen by sequentially choosing one node along the perimeter of the network (with the exception of N0, N7, N14, and N21, which were the anchor nodes in each case). Because there are 28 nodes in the network, this scheme provides 24 test locations for the free node. The RSS data used was the time-averaged empty scene data, and after the image estimation was complete, the only RSS data used for position location was the RSS measured at each of the anchor nodes. The average error for each scene was computed and is displayed in Table 4.4. It can be observed that in each case, the average error when RTI was used was as less than or equal to the error when RTI was not used.

Scatter plots of the distance error for position location with RTI versus position location without RTI are shown in Figures 4.19-4.21, with the correlation coefficient R for each plot shown in the figure caption and the least-squares fit line superimposed on top of the data. It can be seen from these figures that there is a moderate, but not terribly strong, correlation in the magnitudes of distance errors between the two methods. This observation is consistent with the data shown in Appendix B. This can be interpreted to mean that generally when the RTI method has relatively large error, the non-RTI method will likely have relatively large error as well and vise-versa, but this will not necessarily always be the case.

The set of distance errors for both sets of experiments in each scene were aggregated and the histogram of the combined sets of errors for each scene, with and without RTI, are shown in Appendix C.

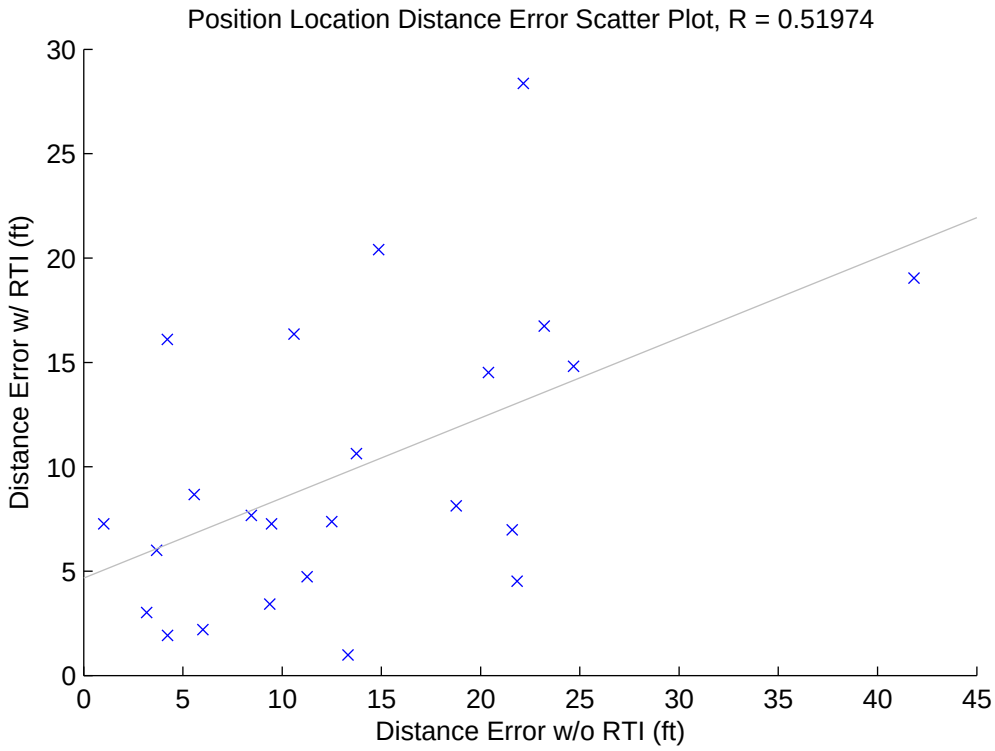

Figure 4.19: Scatter plot of distance error with RTI versus distance error without RTI for the perimeter node experiments performed in scene 1. The least-squares fit line for the data is shown in grey.

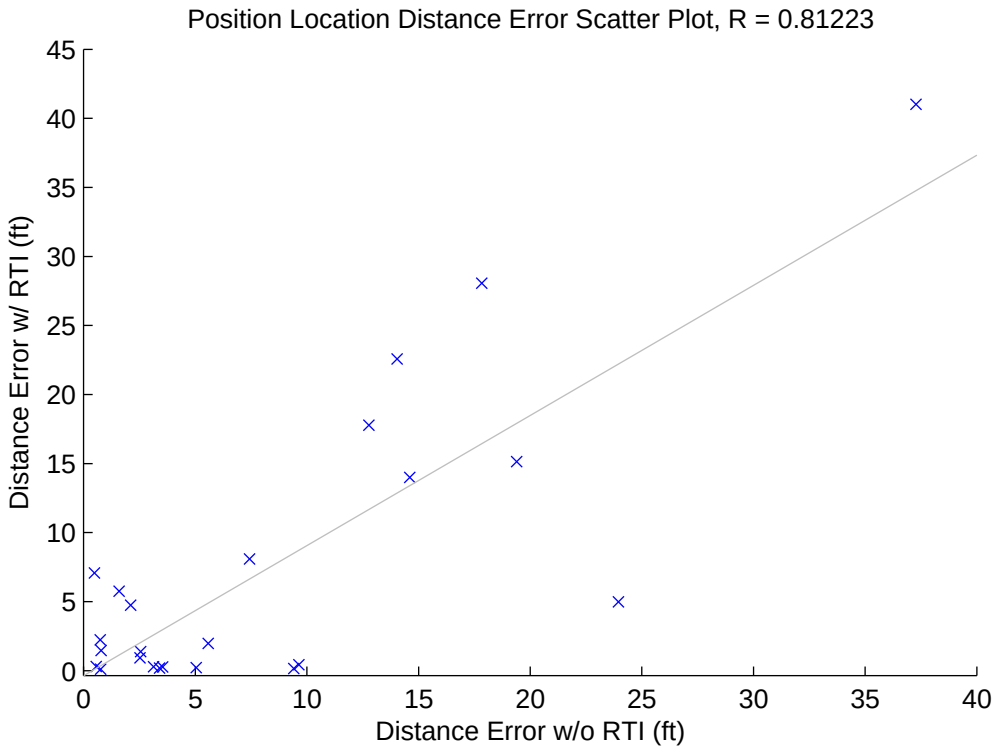

Figure 4.20: Scatter plot of distance error with RTI versus distance error without RTI for the perimeter node experiments performed in scene 2. The least-squares fit line for the data is shown in grey.

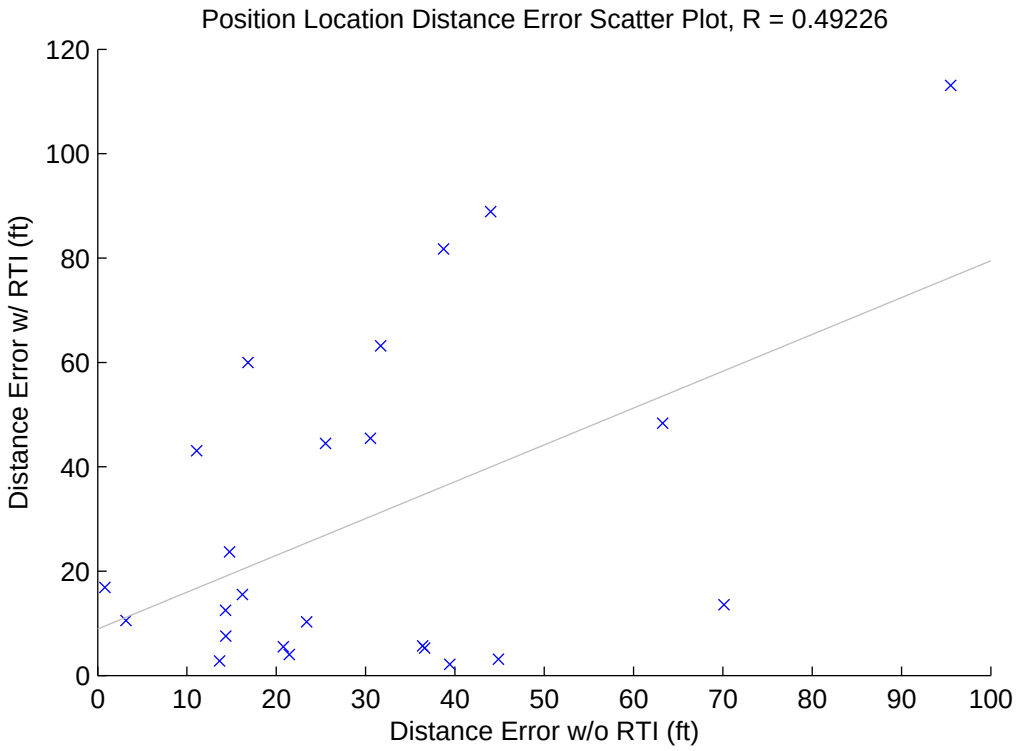

Figure 4.21: Scatter plot of distance error with RTI versus distance error without RTI for the perimeter node experiments performed in scene 3. The least-squares fit line for the data is shown in grey.

4.5.3 Analysis

It can be seen from the proceeding sections that when RTI data was used in conjunction with RSS-based position location, noticeable improvement does occur. However, the improvement varied from scene to scene. For instance, it can be seen from Table 4.4 that the greatest improvement in location accuracy achieved with using RTI occurred in scene 1, and the least improvement in accuracy achieved by using RTI was with scene 3 (no improvement, on average). One possible explanation is that using RTI will yield the best results in cluttered scenes, and that if there is little clutter in a scene, the additional benefit of using RTI with RSS-based position location will be minimal. This hypothesis is supported by the data– the scene with the most clutter was scene 1 (the clutter being the house which blocked a large number of links), and the scene with the least clutter was scene 3 (an open field with some trees). The data in Tables 4.2-4.3 also support this hypothesis. Thus it can be concluded that RTI provides the greatest improvement to RSS-based position location accuracy when the amount of shadowing present in a given area is relatively large.

4.6 Conclusion

In this chapter, it has been shown that the use of an RTI network for attenuation field estimation and RSS-based position location is feasible in real life, and that noticeable improvement does occur when RTI is used to improved RSS-based position location estimates. However, it has also been observed that this improvement is most significant when more clutter is present in the area of interest, and that if an area is relatively uncluttered, marginal to no improvement was observed in these experiments.

Chapter 5

Conclusions

5.1 Summary of Findings

5.1.1 Radio Tomographic Imaging

Radio Tomographic Imaging (RTI) is an emerging field in which a large number of relatively low-cost radio sensors are used to detect the presence of objects within an area of interest. Its strength lies in its simplicity- both in terms of the sensor requirements, and the mathematical algorithms used for inverse imaging. It has been shown that RTI can be used to estimate the location and strength of attenuating objects within the area of interest, and that this knowledge can be used for radio coverage prediction as well as RSS-based position location algorithms.

5.1.2 Improvements to Radio Coverage Prediction

Because of the large number of sensors present in an RTI network, the RTI network can be used to measure the propagation characteristics of an environment, specifically the path-loss exponent and relative reference power (from the exponential path-loss model) and the location and strength of shadowing objects. With knowledge of this data, it can be used to predict the RSS at any point in the field for any given transmitter location with relative simplicity. The advantages of this method over others (such as ray tracing) lies in its simplicity, both conceptual and computational. It has been shown that significant improvement over the standard exponential path-loss model can be achieved, and that the errors in RSS estimation closely follow a Gaussian distribution.

5.1.3 Improvement to RSS-Multilateration

Because RTI can be used to improve RSS predictions, it can also be used to improve the quality of RSS-based position location algorithms, whose major source of error is range estimation error due to shadowing. Once the shadowing has been accounted for (using the attenuation field measured by the RTI network), it has been shown that noticeable improvement can be achieved over using the exponential path loss model only for range estimation. It has also been observed, however, that this improvement is only significant if the area of interest is relatively cluttered, and that when the area of interest is largely uncluttered, marginal to no improvement can be achieved (due to the lack of shadowing objects).

5.2 Open Research Topics

5.2.1 Scalability

The foremost question of interest resulting from this research is the scalability of using RTI for image estimation and RSS prediction over much larger areas. Due to the low transmit power of the Zigbee sensors used in this work, a maximum range of approximately 200-300 ft (in an open area) limited the size of the areas where experiments were performed. It would be of great practical interest to see if these same conclusions were true for larger areas– areas with a radius on the order of hundreds to thousands of meters (i.e., the area covered by a single cell tower). In this case, if the number of cell towers in an area is relatively large, it may be possible to use the towers themselves as the sensor nodes in the RTI network. Investigation into this possibility would be of great interest.

5.2.2 Spatial Sampling Geometry

Another question of interest is this– is it possible to produce accurate image estimates with a small number of sensors? Could a "synthetic array" of RTI sensors be produced by allowing nodes with self localization capability (such as GPS) to move around the perimeter of an area while taking RSS measurements? One of the weaknesses of RTI is that it requires a large number of sensors deployed around the perimeter of the area of interest, and if similar accuracy can be obtained by creating a synthetic array of measurement locations, this would greatly increase the number of potential applications that RTI could be used in.

5.2.3 Refinement of Linear Estimation Problem

The linear estimation problem formulated in Chapter 2 for inverse image reconstruction is relatively simple, in terms of its formulation and assumptions (such as the pixel selection algorithm, or the assumption that the noise is Gaussian). Further improvements to image quality may be obtained by using non-Gaussian noise models (and adjusting the linear estimators according the the statistics of the new noise distribution). As well, further improvement may be obtained by refining the pixel selection algorithm (i.e., the method of choosing which pixels are included in each link, and how each pixels relative attenuation is weighted) or other aspects of the linear estimation problem.

5.2.4 Spatial Correlation of Received Signal Strength

Another area of future research that could improve the quality of image estimates could be to study the effect of spatial correlation on RSS measurements. Because the wavelengths involved are on the order of centimeters, the multipath profile may cause RSS measurements to be very different if a transceiver is only moved by a fraction of the wavelength. Future work could focus on studying the effect of moving each transceiver from it's nominal location by a random, but small, amount, and then averaging the RSS values recorded at each transceiver for several random perturbations in its location. This could potentially average out the effect of small-scale fading (multipath), which is suspected to be a primary source of error in the RTI measurements.

5.3 Conclusion

It has been shown in this thesis that RTI can be used for RSS-prediction, and subsequently, can also be used to improve RSS-based multilateration. This is an exciting development because it provides another set of tools for propagation prediction that are incredibly simple and could potentially be applied in a wide number of situations because the only measurement capability needed in the hardware is RSS measurement, which is a feature included in practically every wireless digital communication device. Future work in this field could include studying the scalability of these methods to larger areas, developing practical ways of obtaining image estimates with a smaller number of sensors, and refining the linear estimation problem formulation.

Appendix A

RSS Estimation Error Statistics

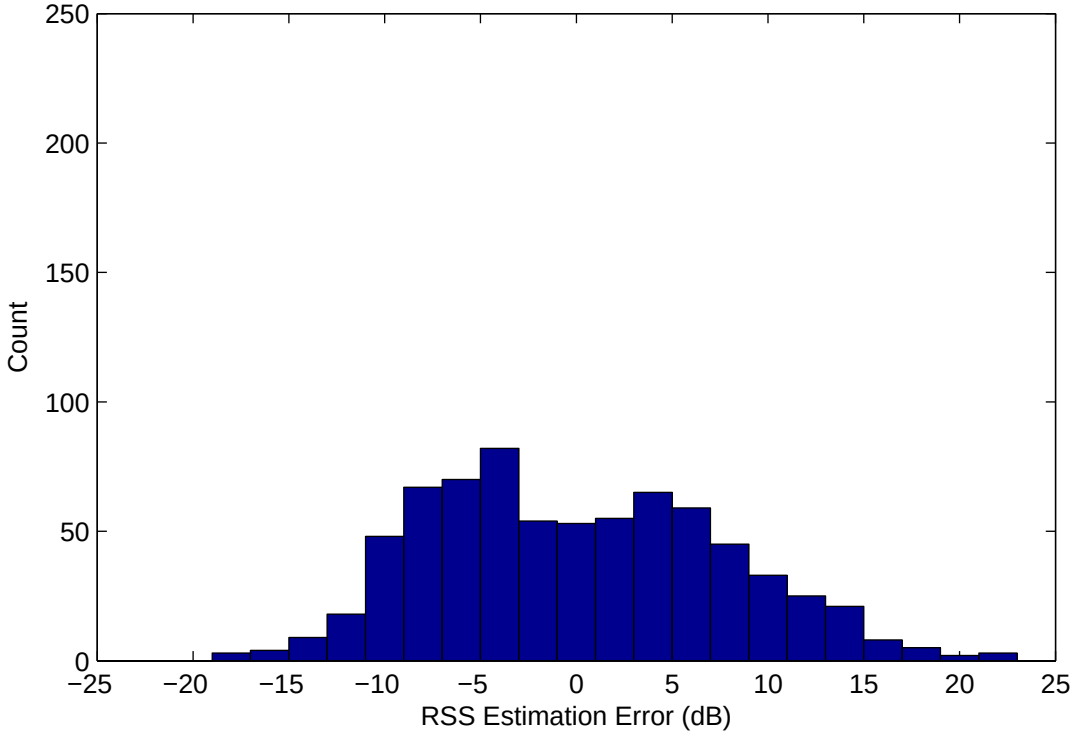

Figure A.1: Histogram of RSS estimation error without using RTI for scene 1 (empty).

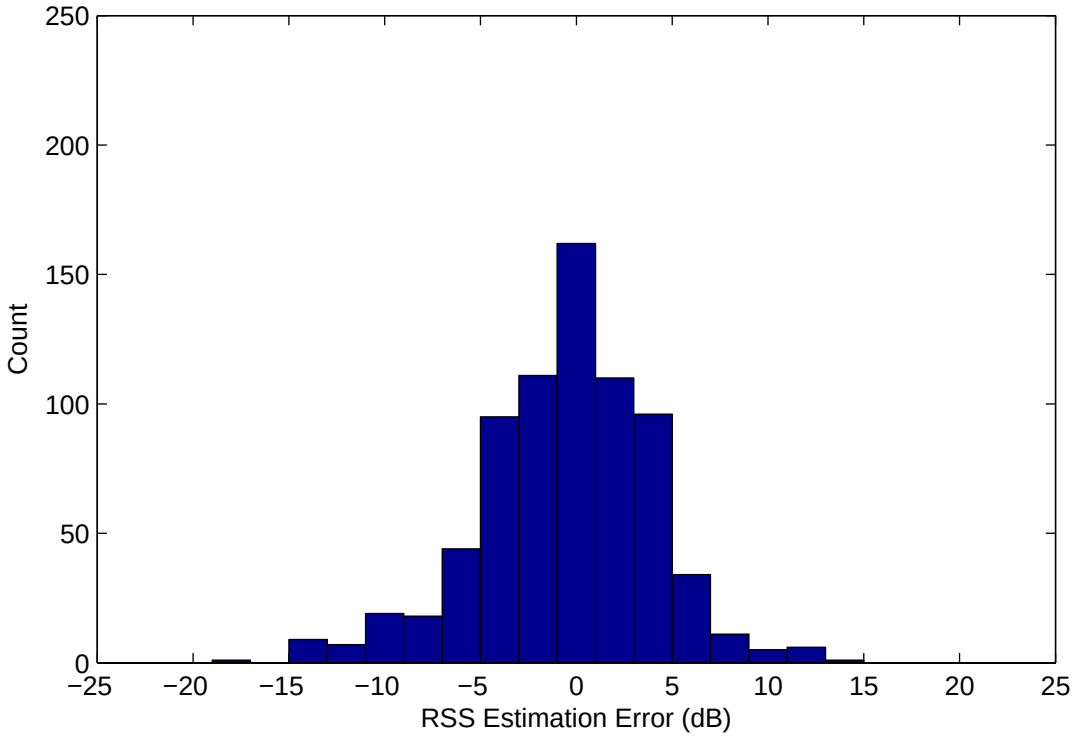

Figure A.2: Histogram of RSS estimation error with RTI for scene 1 (empty).

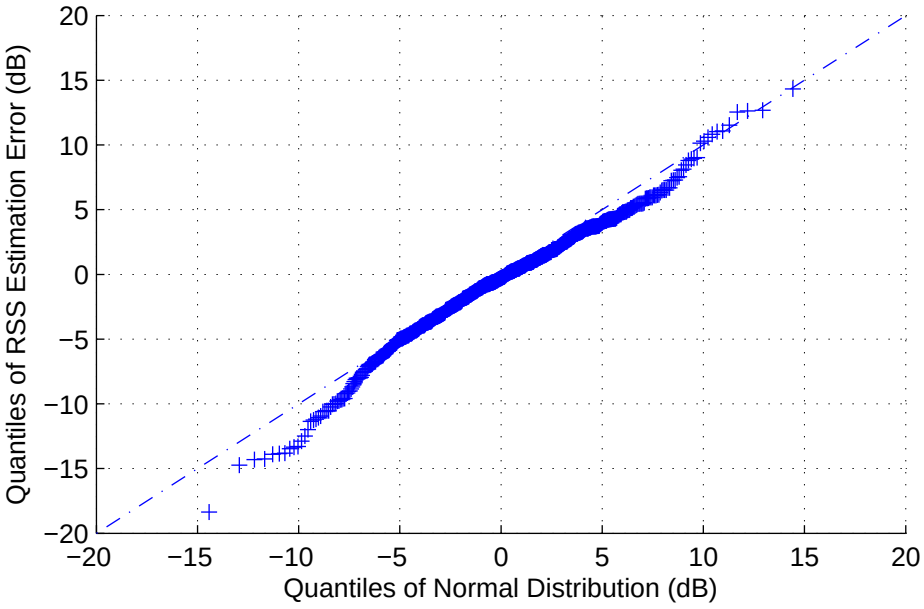

Figure A.3: Q-Q Plot of RSS estimation error versus normal distribution for scene 1 (empty).

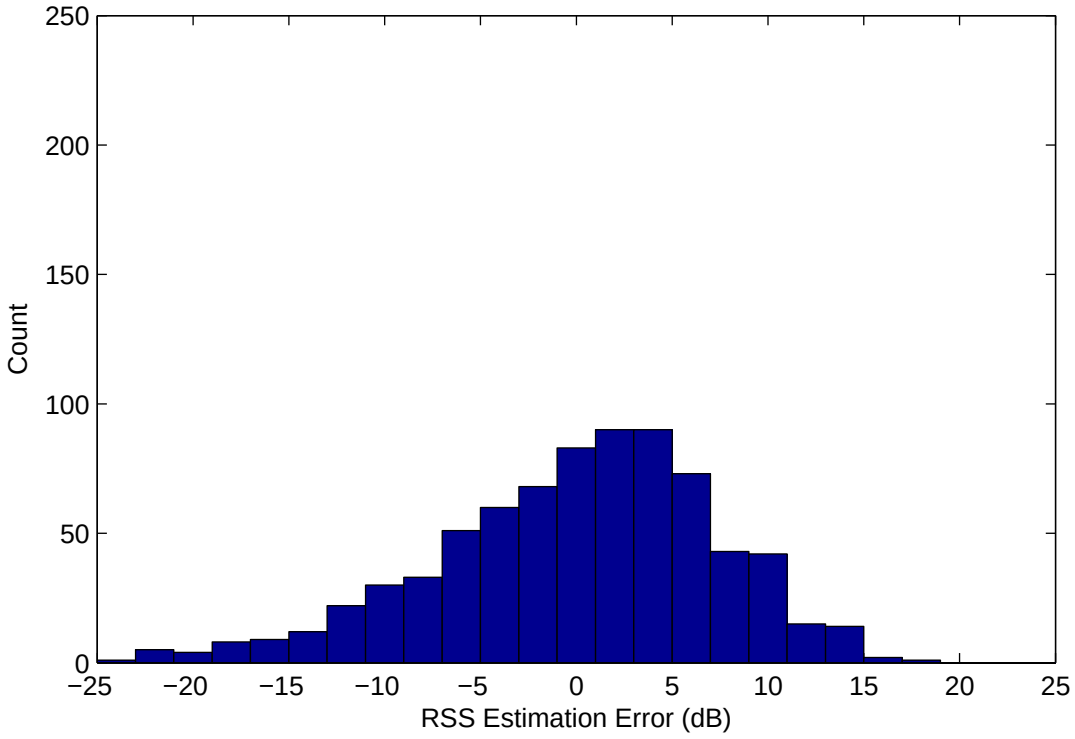

Figure A.4: Histogram of RSS estimation error without using RTI for scene 2 (empty).

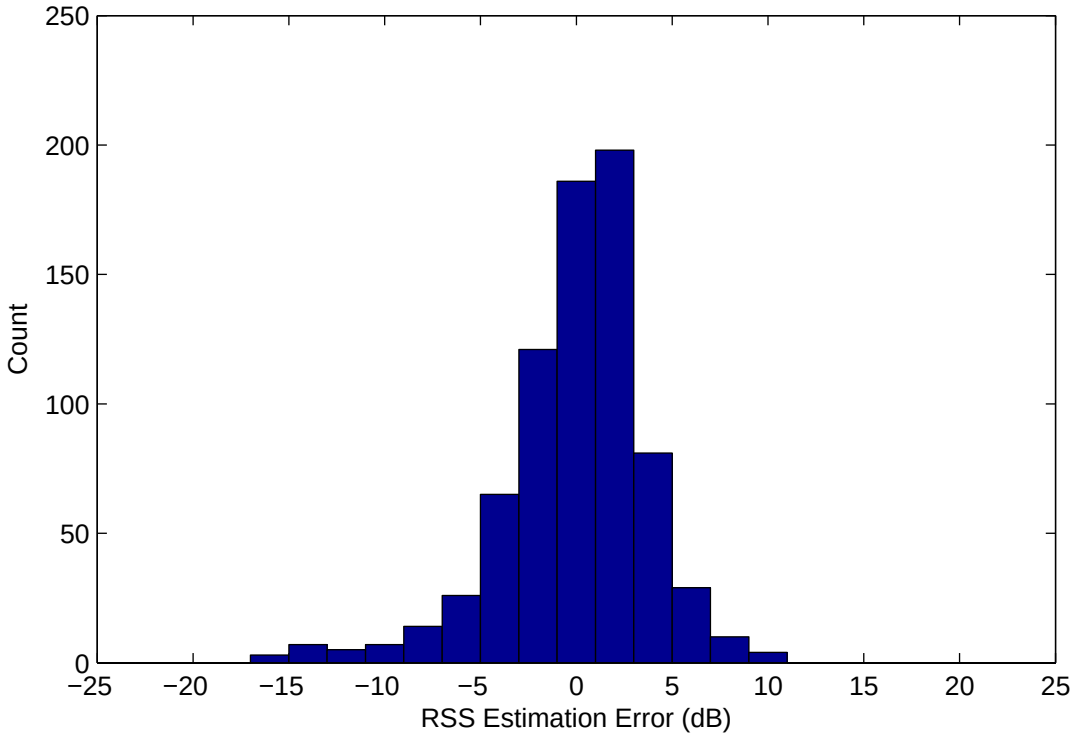

Figure A.5: Histogram of RSS estimation error with RTI for scene 2 (empty).

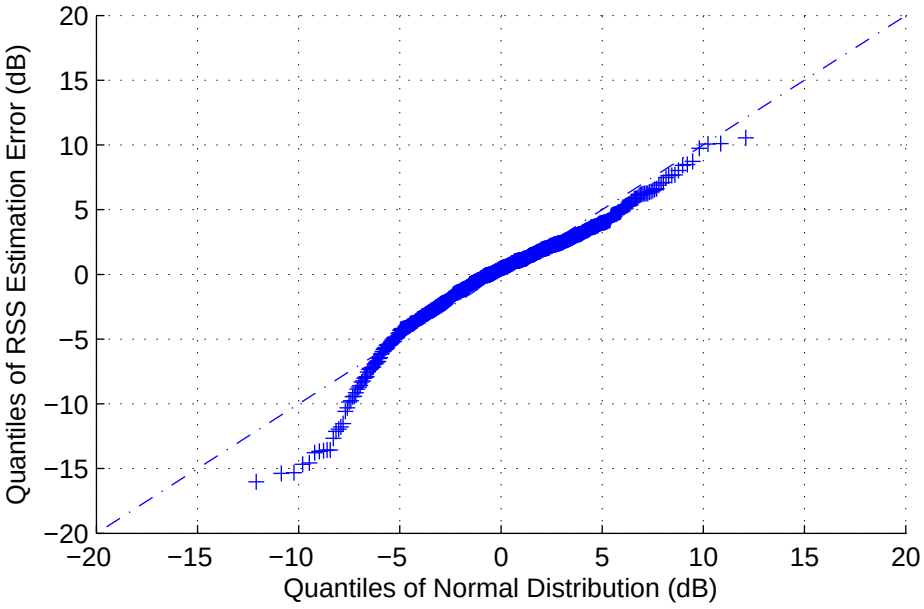

Figure A.6: Q-Q Plot of RSS estimation error versus normal distribution for scene 2 (empty).

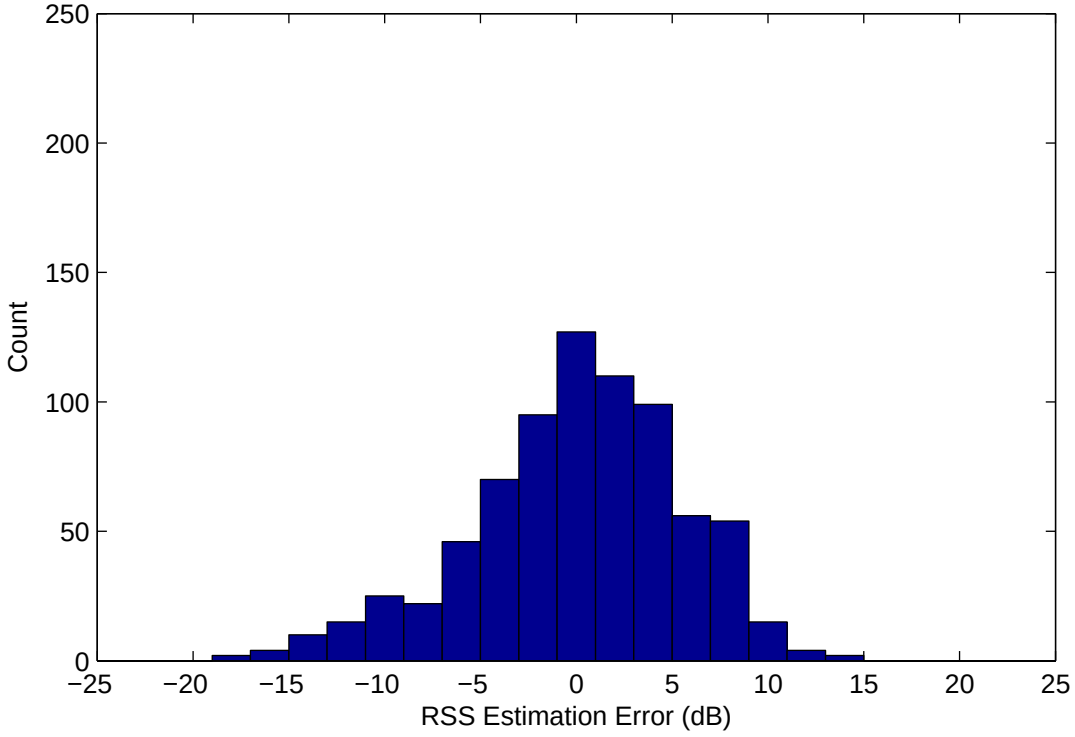

Figure A.7: Histogram of RSS estimation error without using RTI for scene 3 (empty).

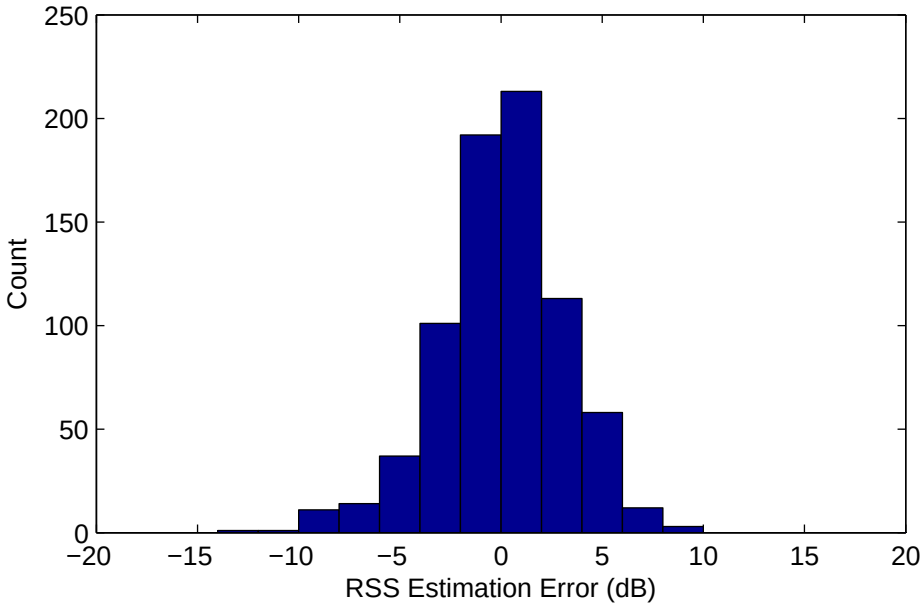

Figure A.8: Histogram of RSS estimation error with RTI for scene 3 (empty).

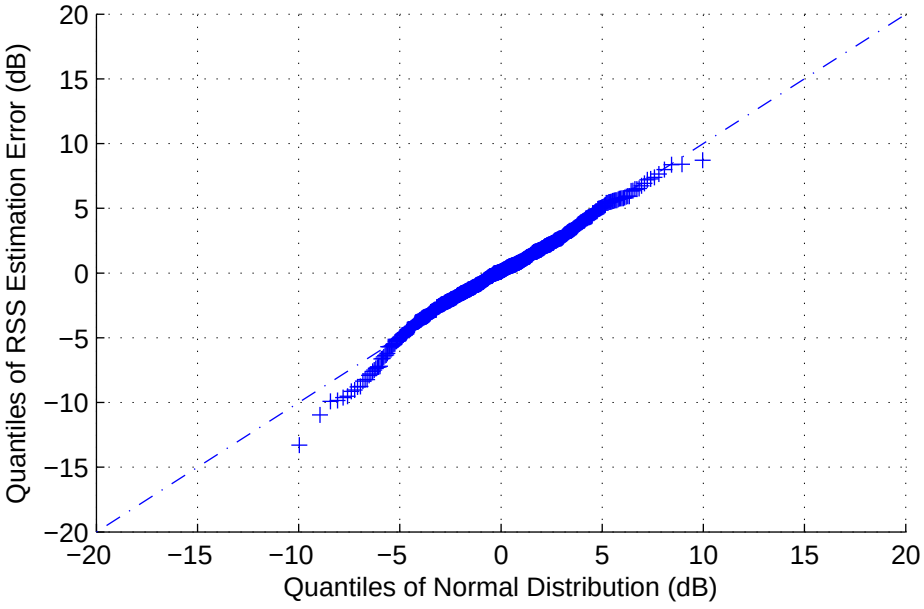

Figure A.9: Q-Q Plot of RSS estimation error versus normal distribution for scene 3 (empty).

Appendix B

Position Location Plots

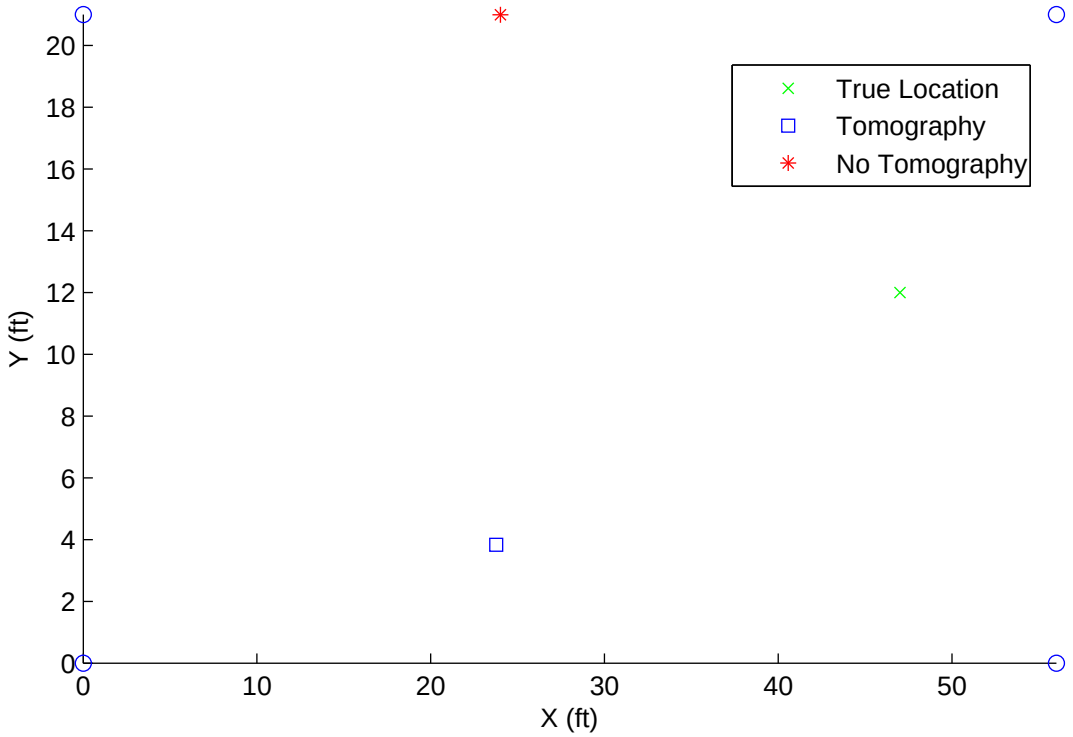

Figure B.1: Location estimates with and without tomography for node position 1 in scene 2. The blue circles represent anchor node locations.

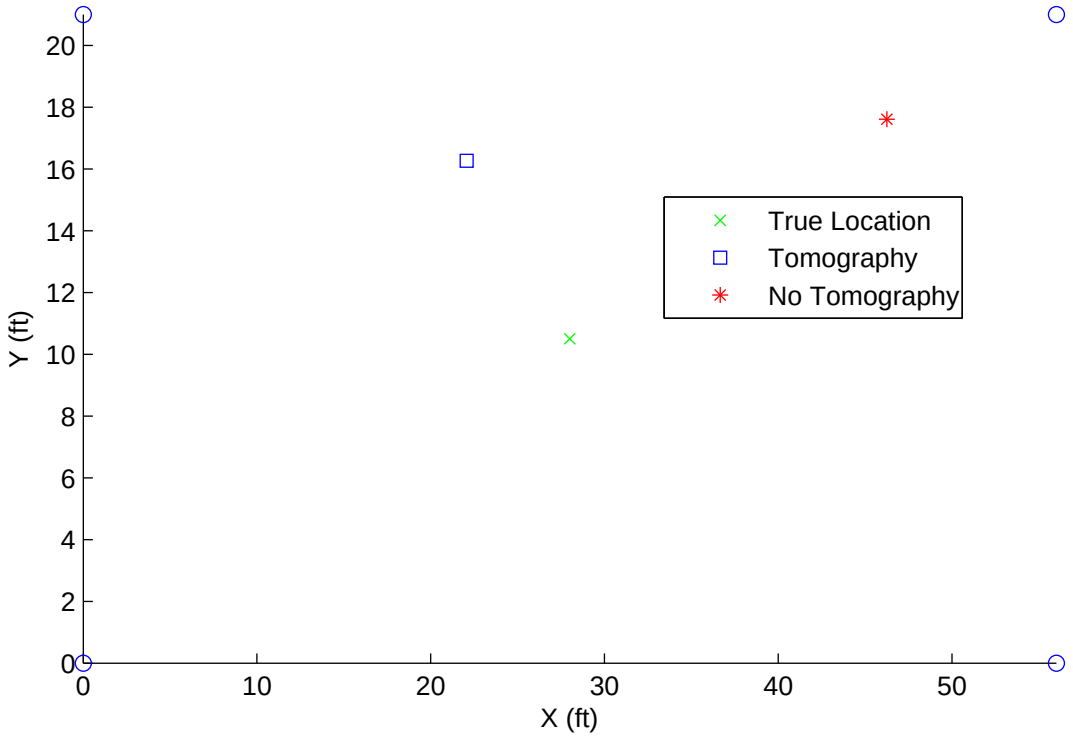

Figure B.2: Location estimates with and without tomography for node position 2 in scene 2. The blue circles represent anchor node locations.

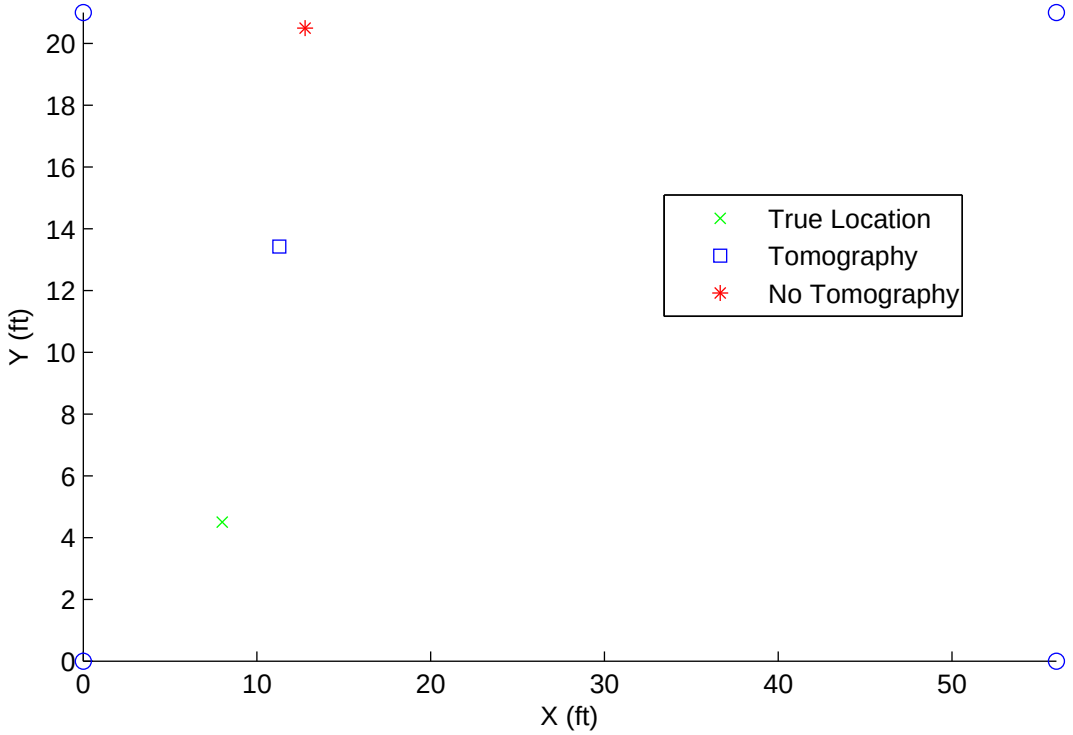

Figure B.3: Location estimates with and without tomography for node position 3 in scene 2. The blue circles represent anchor node locations.

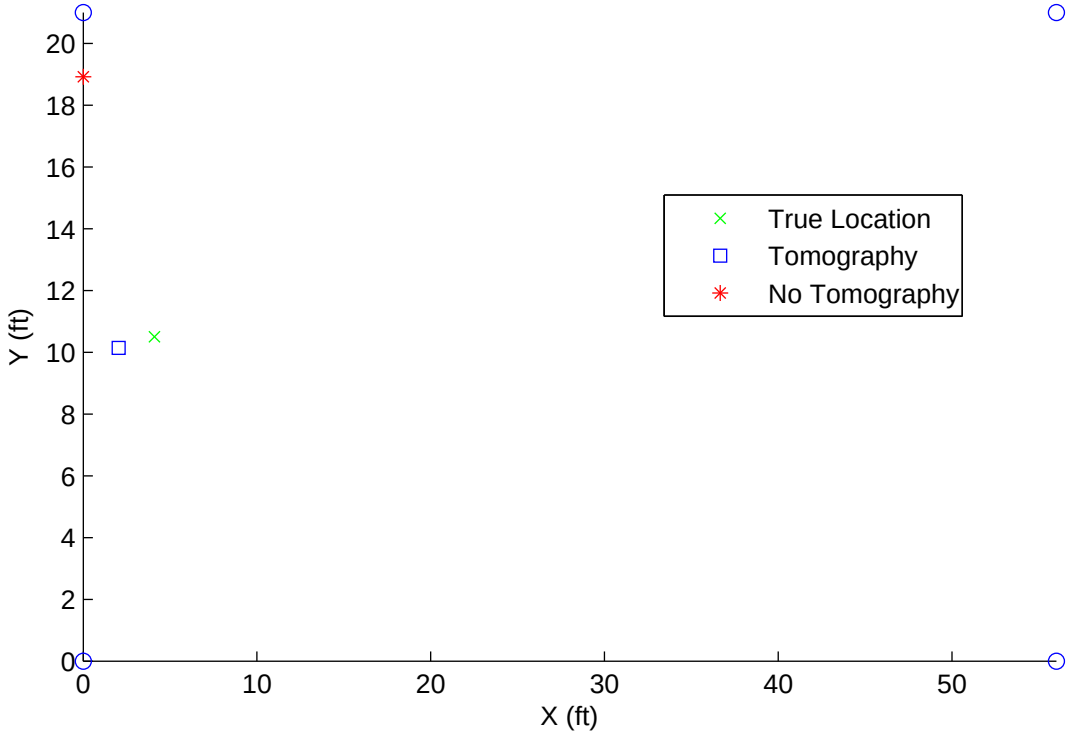

Figure B.4: Location estimates with and without tomography for node position 4 in scene 2. The blue circles represent anchor node locations.

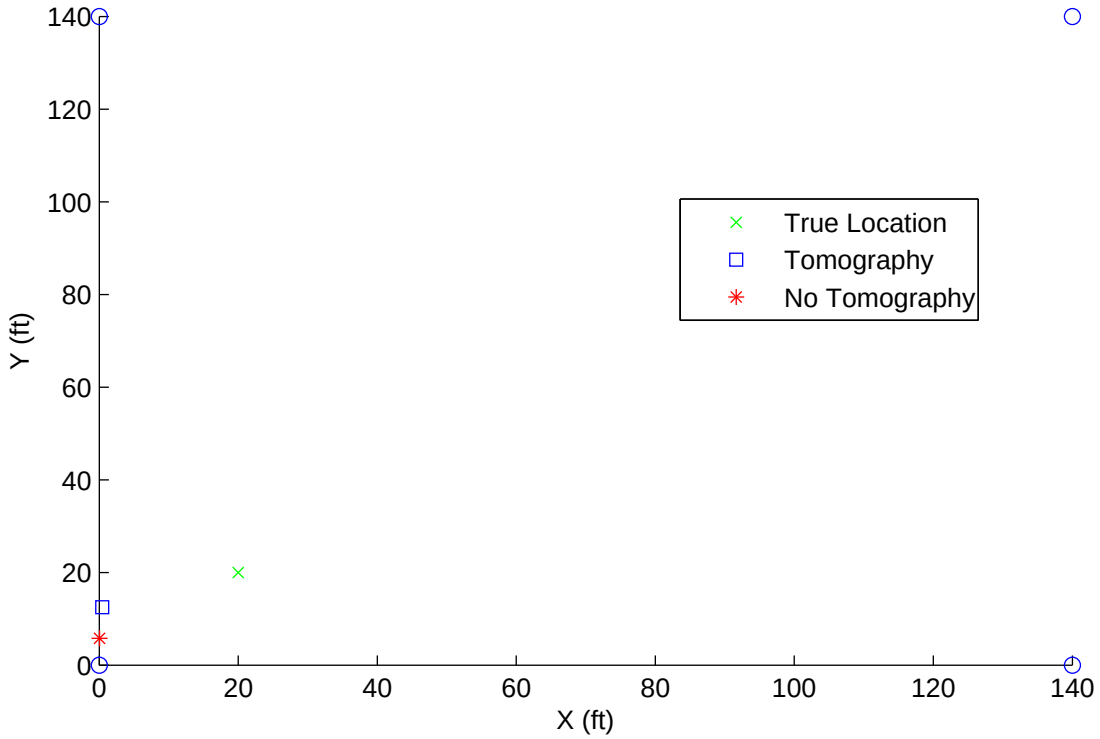

Figure B.5: Location estimates with and without tomography for node position 1 in scene 3. The blue circles represent anchor node locations.

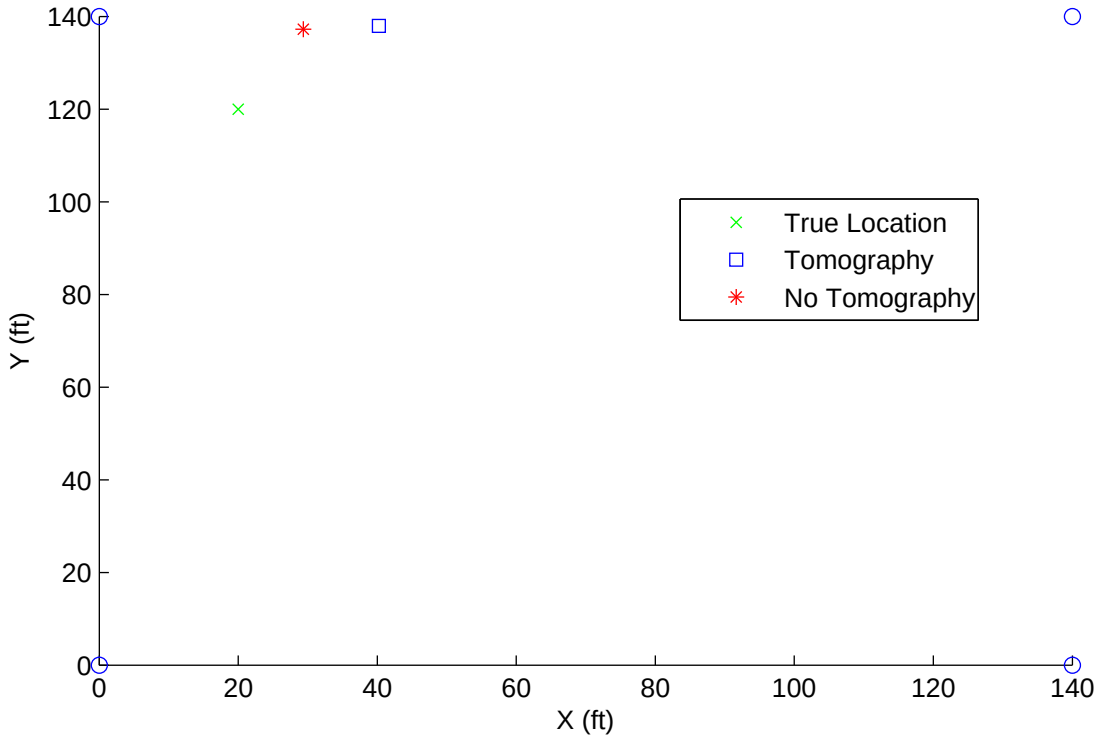

Figure B.6: Location estimates with and without tomography for node position 2 in scene 3. The blue circles represent anchor node locations.

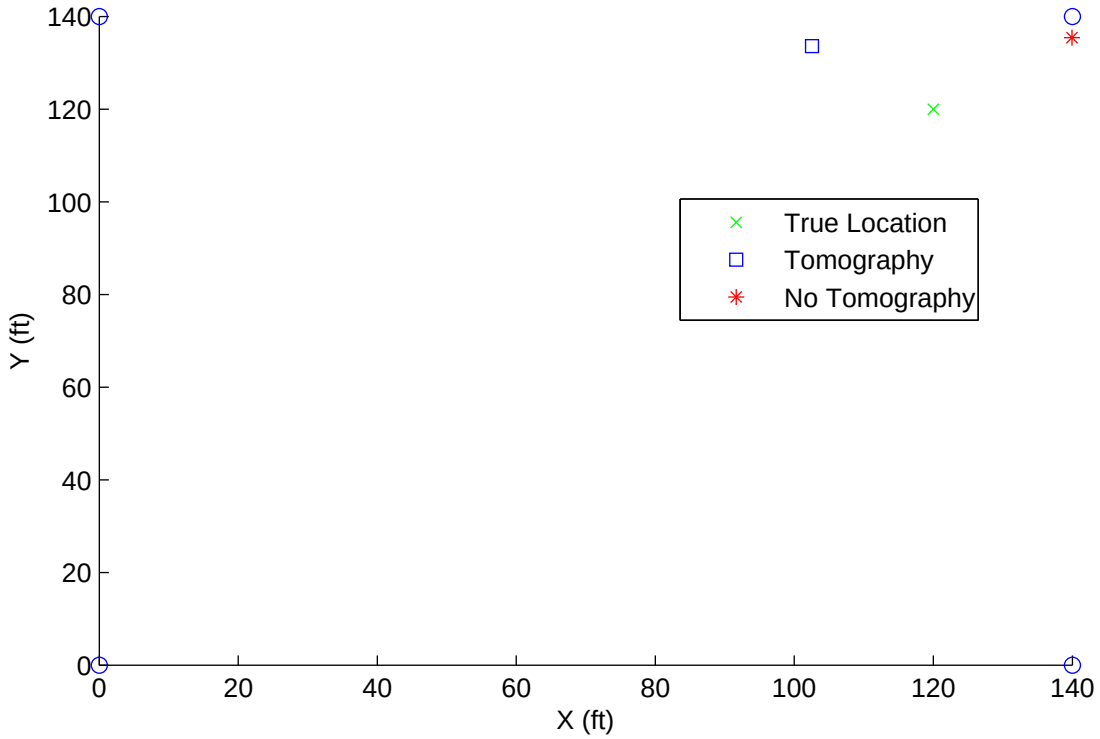

Figure B.7: Location estimates with and without tomography for node position 3 in scene 3. The blue circles represent anchor node locations.

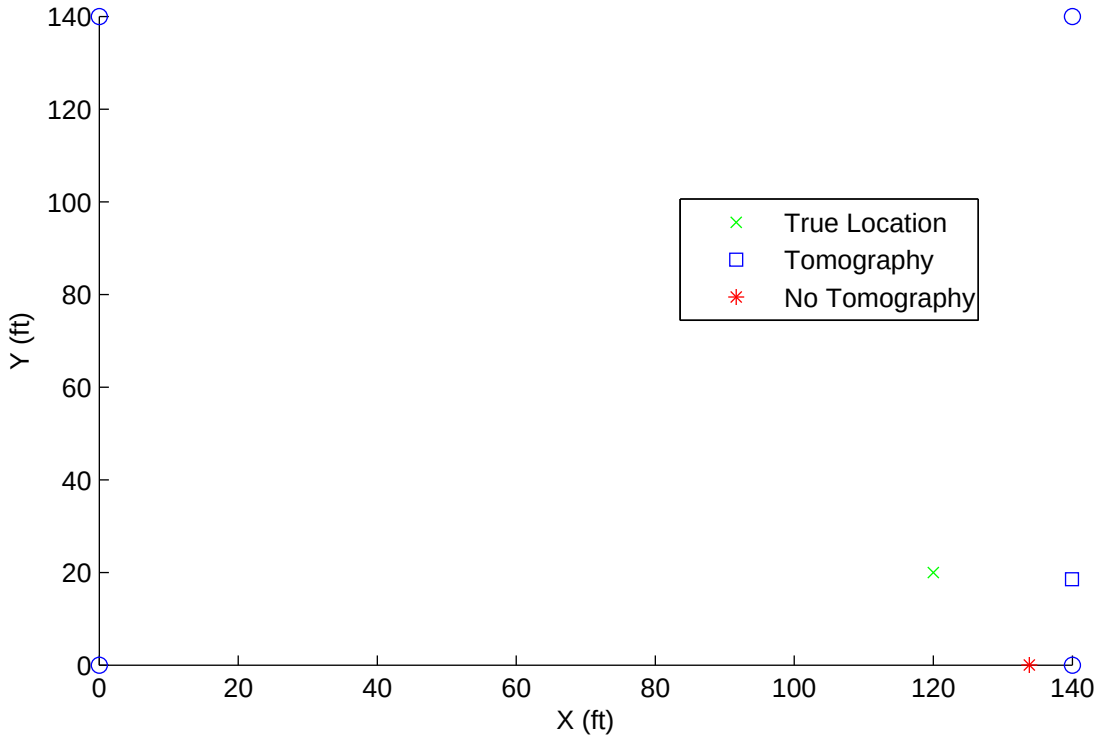

Figure B.8: Location estimates with and without tomography for node position 4 in scene 3. The blue circles represent anchor node locations.

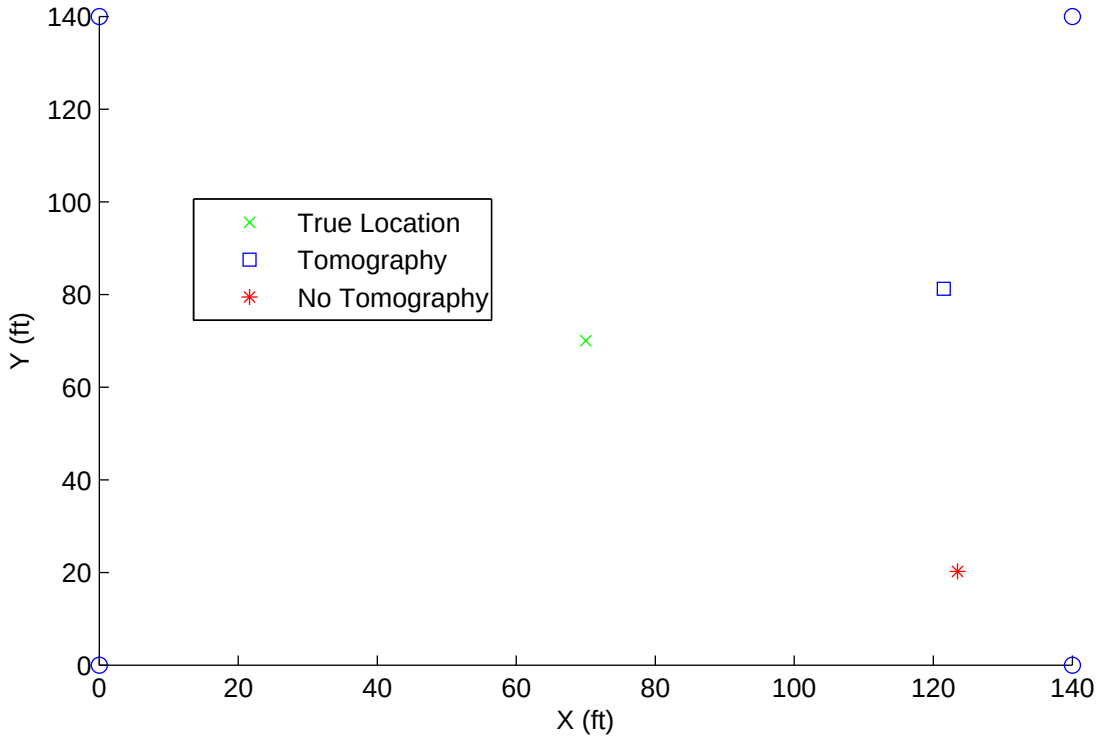

Figure B.9: Location estimates with and without tomography for node position 5 in scene 3. The blue circles represent anchor node locations.

Appendix C

Localization Error Statistics

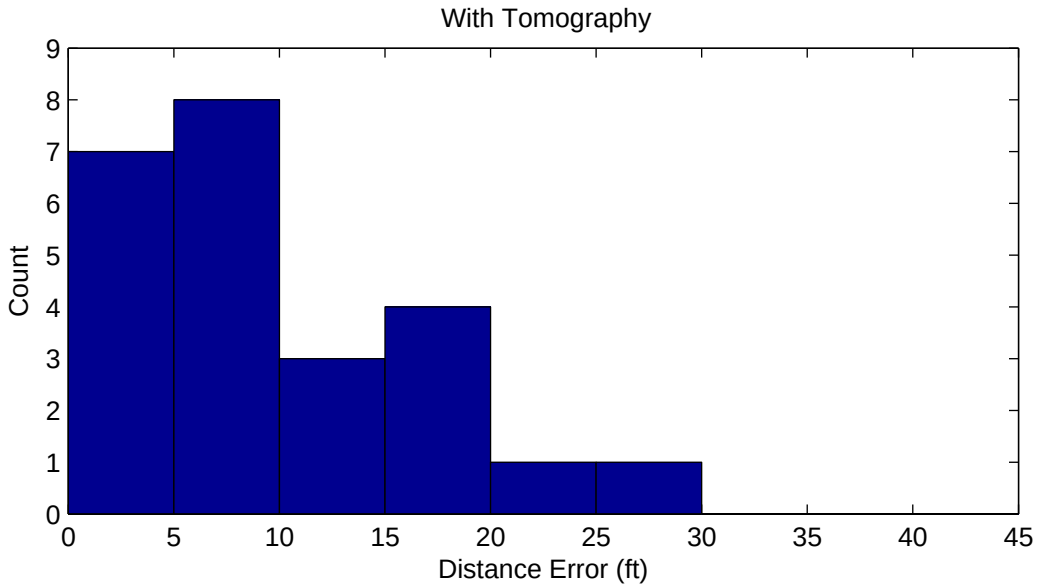

Figure C.1: Histogram of localization errors for the network deployed in scene 1 utilizing tomography data.

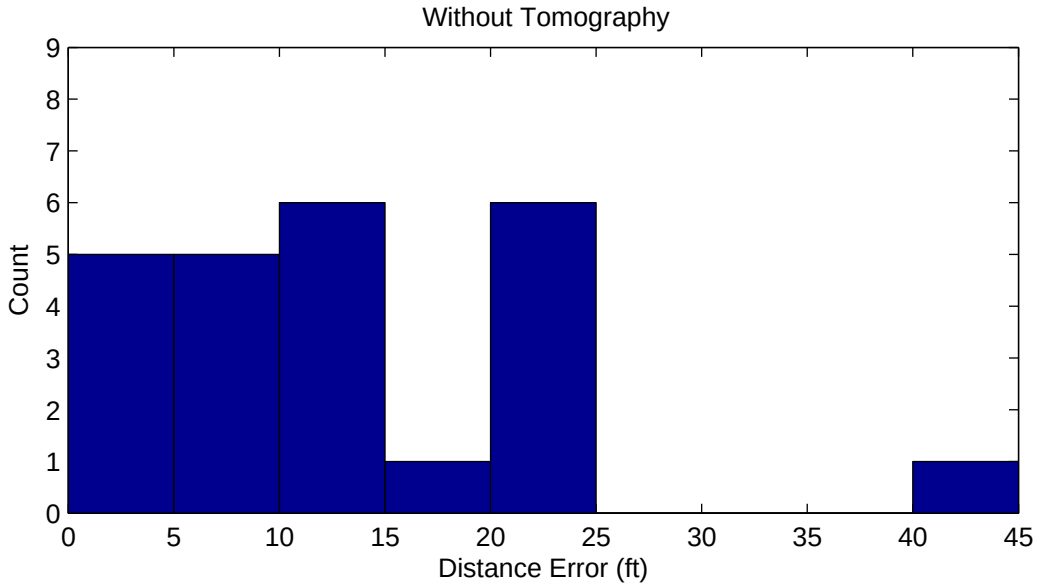

Figure C.2: Histogram of localization errors for the network deployed in scene 1 without utilizing tomography data.

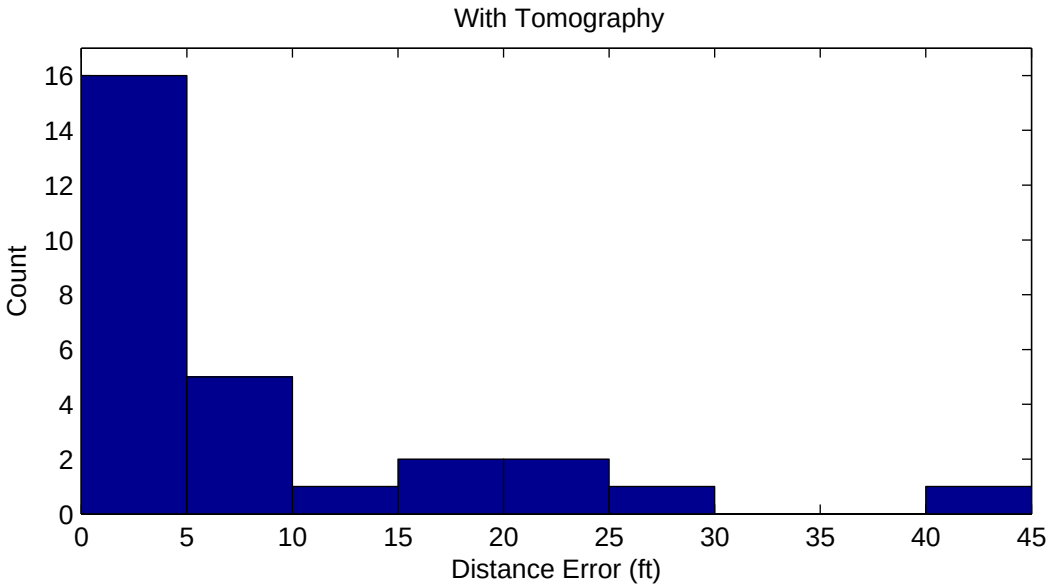

Figure C.3: Histogram of localization errors for the network deployed in scene 2 utilizing tomography data.

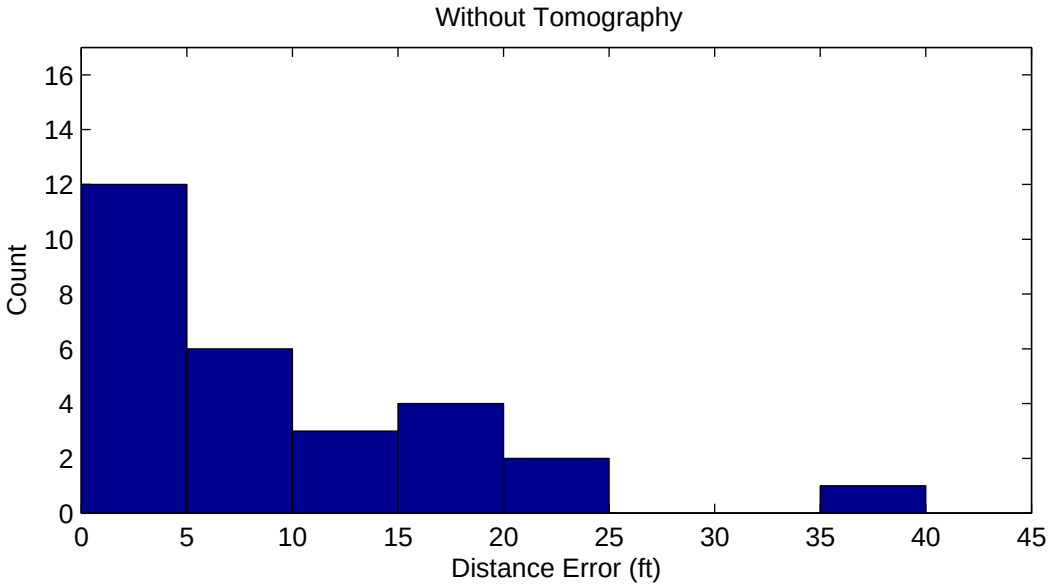

Figure C.4: Histogram of localization errors for the network deployed in scene 2 without utilizing tomography data.

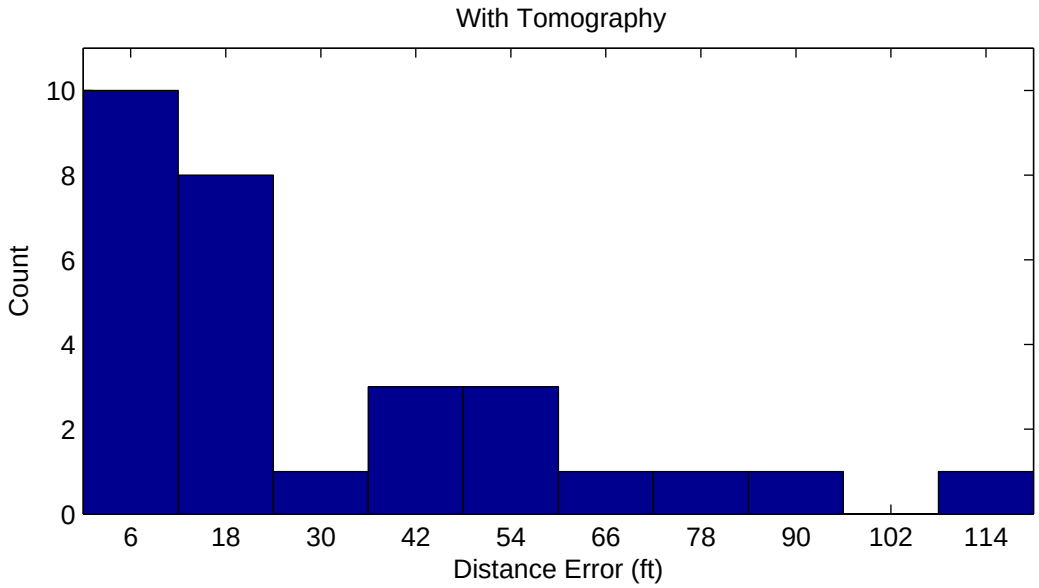

Figure C.5: Histogram of localization errors for the network deployed in scene 3 utilizing tomography data.

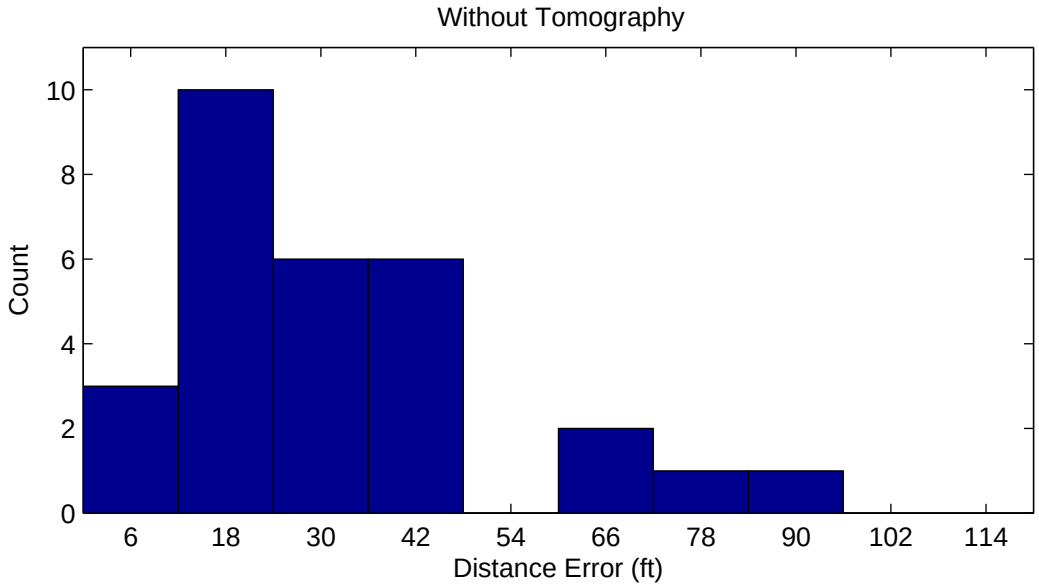

Figure C.6: Histogram of localization errors for the network deployed in scene 3 without utilizing tomography data.

Bibliography

[1] A. C. Kak and M. Slaney, *Principles of Computerized Tomographic Imaging*. IEEE Press, 1999. [Online]. Available: http://www.slaney.org/pct/pct-toc.html

[2] J. Wilson and N. Patwari, "Radio tomographic imaging with wireless networks," *IEEE Transactions on Mobile Computing*, vol. 9, no. 5, pp. 621–632, 2010.

[3] J. H. Lee, "Physical layer security for wireless position location in the presence of location spoofing," Ph.D. dissertation, Virginia Polytechnic Institute and State University, March 2011.

[4] A. Wilson, "Device-free localization with received signal strength measurements in wireless networks," Ph.D. dissertation, The University of Utah, United States – Utah, 2010.

[5] N. Patwari and P. Agrawal, "Effects of correlated shadowing: Connectivity, localization, and RF tomography," in *Information Processing in Sensor Networks, 2008. IPSN '08. International Conference on*, Apr. 2008, pp. 82 –93.

[6] A. Tarantola, *Inverse Problem Theory and Methods for Model Parameter Estimation*. Society for Industrial Mathematics, 2005. [Online]. Available: http://www.ipgp.fr/ tarantola/Files/Professional/Books/index.html

[7] R. W. Deming, "Tutorial on Fourier space coverage for scattering experiments, with application to SAR," in *Proceedings of SPIE*, vol. 7699, 2010, pp. 769 904–769 904–12.

[8] M. Wicks, B. Himed, J. Bracken, H. Bascom, and J. Clancy, "Ultra narrow band adaptive tomographic radar," in *Computational Advances in Multi-Sensor Adaptive Processing, 2005 1st IEEE International Workshop on*, Dec. 2005, pp. 36 – 39.

[9] M. Wicks, "RF tomography with application to ground penetrating radar," in *Signals, Systems and Computers, 2007. ACSSC 2007. Conference Record of the Forty-First Asilomar Conference on*, Nov. 2007, pp. 2017 –2022.

[10] L. Lo Monte and D. Erricolo, "Propagation model, optimal geometry and receiver design for RF geotomography," in *Radar Conference, 2008. RADAR '08. IEEE*, May 2008, pp. 1 –6.

[11] L. Lo Monte, D. Erricolo, F. Soldovieri, and M. C. Wicks, "Radio frequency tomography for tunnel detection," *Geoscience and Remote Sensing, IEEE Transactions on*, vol. 48, no. 3, pp. 1128 –1137, March 2010.

[12] L. Lo Monte, F. Soldovieri, I. Akduman, and M. C. Wicks, "Imaging under irregular terrain using RF tomography and numerical Green functions," in *2010 IEEE Antennas and Propagation Society International Symposium (APSURSI)*, 2010, pp. 1–4.

[13] L. Lo Monte, D. Erricolo, F. Soldovieri, and M. C. Wicks, "Recent advances in RF tomography for underground imaging," in *Ground Penetrating Radar (GPR), 2010 13th International Conference on*, June 2010, pp. 1 –6.

[14] A. Goldsmith, *Wireless Communications*. Cambridge University Press, 2005.

[15] T. Rappaport, *Wireless Communications*. Prentice Hall PTR, 2002.

[16] A. Longley, "Prediction of tropospheric radio transmission loss over irregular terrain - a computer method - 1968," Institute for Telecommunication Sciences, Boulder CO., Tech. Rep., 1968.

[17] K. Chamberlin and R. Luebbers, "An evaluation of Longley-Rice and GTD propagation models," *Antennas and Propagation, IEEE Transactions on*, vol. 30, no. 6, pp. 1093 – 1098, Nov. 1982.

[18] P. Agrawal and N. Patwari, "Correlated link shadow fading in multi-hop wireless networks," *Wireless Communications, IEEE Transactions on*, vol. 8, no. 8, pp. 4024 –4036, Aug. 2009.

[19] N. Patwari, J. Ash, S. Kyperountas, I. Hero, A.O., R. Moses, and N. Correal, "Locating the nodes: cooperative localization in wireless sensor networks," *Signal Processing Magazine, IEEE*, vol. 22, no. 4, pp. 54 – 69, July 2005.

[20] J. Wilson and N. Patwari, "Through-wall tracking using variance-based radio tomography networks," *Arxiv preprint arXiv:0909.5417*, 2009. [Online]. Available: http://arxiv.org/abs/0909.5417

[21] X. Chen, A. Edelstein, Y. Li, M. Coates, M. Rabbat, and A. Men, "Sequential monte carlo for simultaneous passive device-free tracking and sensor localization using received signal strength measurements," 2011.

[22] Y. Li, X. Chen, M. Coates, and B. Yang, "Sequential monte carlo radio-frequency tomographic tracking," in *Proc. Int. Conf. Acoustics, Speech, and Signal Processing, ICASSP*, vol. 11, May 2011.

[23] E. Callaway, M. Perkins, Q. Shi, and N. Patwari, "Intra-piconet location determination and tomography," United States of America Patent 6 745 038, June 1, 2004.

[24] S. Kay, *Fundamentals of Statistical Signal Processing: Estimation Theory.* Prentice Hall PTR, 1993.

[25] A. Leon-Garcia, *Probability, Statistics, and Random Processes for Electrical Engineering.* Prentice Hall, 2008.

[26] CC2420 2.4 GHz IEEE 802.15.4 / ZigBee-ready RF Transceiver Datasheet. Texas Instruments. [Online]. Available: http://www.ti.com/lit/ds/symlink/cc2420.pdf

[27] J. Wilson, N. Patwari, and F. Vasquez, "Regularization methods for radio tomographic imaging," in *2009 Virginia Tech Symposium on Wireless Personal Communications*, 2009.

[28] J. Crockett and H. Chernoff, "Gradient methods of maximization," *Pacific Journal of Mathematics*, vol. 5, no. 1, pp. 33–50, 1955.

[29] J. Wilson. Spin - TinyOS Code for RSS Collection. University of Utah SPAN Lab. [Online]. Available: http://span.ece.utah.edu/spin